Micromechanical damage and fracture in elastomeric polymers

A Thesis by

Stefanie Heyden

in Partial Fulfillment of the Requirements

for the Degree of

Doctor of Philosophy

California Institute of Technology

Pasadena, California

2015

(Defended October 13, 2014)

To my Mom –
for shipping tons of chocolate over the Atlantic.

To my Dad –
for trying to bring my blood sugar back to non-comatose levels
(I promise, I will accomplish a pull-up one day).

And to the boy I came with four years ago –
for everything in between.

Acknowledgements

This thesis is the result of four years of work under the continued guidance and inspiration of my advisor, Professor Michael Ortiz. His kindness, patience, and unceasing support have served as a constant reminder of how fortunate I was to become a member of his group. Above all, however, I would like to thank him for changing my perspective: from viewing science as a means of understanding – to getting a glimpse at the beauty behind it all.

Moreover, I would like to express my gratitude to the members of my thesis committee, Professors Guruswami Ravichandran, Kaushik Bhattacharya, and Kerstin Weinberg (University of Siegen), who have supported my work through all those years with many kind and truly uplifting words as well as personal advice and guidance, even from afar. In addition, Professor Anna Pandolfi (Politecnico di Milano) has been a wonderful mentor and teacher, whose research visits at Caltech I deeply cherished. Further inspiring bright minds that I was lucky enough to collaborate with include Professors Sergio Conti (University of Bonn) and Wolfgang Wall (TUM), whose help and support through the *Hausdorff Center for Mathematics* and *Institute for Advanced Study*, respectively, enabled several research stays and scientific adventures outside the United States. Financial support from the Office of Naval Research and the National Science Foundation is also gratefully acknowledged.

Looking back on my time at Caltech, I am indebted to many other people who have surrounded me over the years. Lydia and Marta, my days as a graduate student were brightened every time I stepped into your offices. Cindy, Jonathan, Brandon and Panos – coffee breaks, studying for qualifying exams, or being teaching assistants wouldn't have been the same without the amazing group of people I could be a part of. My deep appreciation also goes to Bo Li as one of those great students whose paths I tried to follow, for passing on his knowledge and introducing me to his computational methods in countless discussions. Aubrie and Jeff, thanks for late-night pizza deliveries to campus through the pouring rain, for converting math variables into farm animals, but most importantly, for your friendship. Gabriela, muchisimas gracias for simply being my best buddy, in- and outside the research bubble.

Finally, I would like to thank my little sister. Her light-hearted spirit always reminds me not to take ourselves too seriously.

Abstract

This thesis aims at a simple one-parameter macroscopic model of distributed damage and fracture of polymers that is amenable to a straightforward and efficient numerical implementation. The failure model is motivated by post-mortem fractographic observations of void nucleation, growth and coalescence in polyurea stretched to failure [Weinberg and Reppel, 2013], and accounts for the specific fracture energy per unit area attendant to rupture of the material.

Furthermore, it is shown that the macroscopic model can be rigorously derived, in the sense of optimal scaling, from a micromechanical model of chain elasticity and failure regularized by means of fractional strain-gradient elasticity. Optimal scaling laws that supply a link between the single parameter of the macroscopic model, namely the critical energy-release rate of the material, and micromechanical parameters pertaining to the elasticity and strength of the polymer chains, and to the strain-gradient elasticity regularization, are derived. Based on optimal scaling laws, it is shown how the critical energy-release rate of specific materials can be determined from test data. In addition, the scope and fidelity of the model is demonstrated by means of an example of application, namely Taylor-impact experiments of polyurea rods. Hereby, optimal transportation meshfree approximation schemes using maximum-entropy interpolation functions are employed.

Finally, a different crazing model using full derivatives of the deformation gradient and a core cut-off is presented, along with a numerical non-local regularization model. The numerical model takes into account higher-order deformation gradients in a finite element framework. It is shown how the introduction of non-locality into the model stabilizes the effect of strain localization to small volumes in materials undergoing softening. From an investigation of craze formation in the limit of large deformations, convergence studies verifying scaling properties of both local- and non-local energy contributions are presented.

Contents

List of Figures

List of Tables

Notation

The following table gives an overview of different symbols used in the present work. In general, scalar quantities are denoted by lowercase letters, whereas bold lower- and uppercase letters denote vector and tensor quantities, respectively.

A, a	area in the undeformed and deformed configuration
$\mathbf{x}$, $\mathbf{X}$	coordinates in the deformed and undeformed configuration
x, y, z	Cartesian coordinates
$\mathbf{C}$	right Cauchy-Green deformation tensor
$\mathbf{e}_i$	unit vectors in Cartesian coordinates
E	Young's modulus
$\mathbf{F}$	deformation gradient tensor
$\mathbf{f}$	vector of body or surface forces
$\mathbf{f}_{\text{int}}, \mathbf{f}_{\text{ext}}$	vector of internal and external forces
J	Jacobian
$\mathbf{L}$	velocity gradient tensor
$\mathbf{n}$	unit normal vector
$\widetilde{N}_i$	shape functions
Q	heat
S	entropy
t	time
Δt	time increment
$\mathbf{t}$	traction vector
T	temperature
$\mathbf{u}$	displacement vector
$\mathbf{v}$	velocity vector
L	Langevin function
k_B	Boltzmann constant
l_t	total polymer chain length
l_m	monomer length
β	reciprocal absolute temperature
σ	variance

λ_r	relative stretch
$\nu(N)$	distribution of polymer chains with N monomers
$\rho(l_t, N)$	probability distribution of chains with N monomers of total length l_t
κ, μ, λ	bulk modulus, shear modulus, Lamé parameter
H	Hamiltonian of a system
Z	partition function
$\mathcal{L}$	stochastic point process
$\mathcal{T}$	Delaunay tesselation
$\mathbf{I}$	second-order identity tensor
$\mathbf{E}$	Green-Lagrange strain tensor
$\boldsymbol{\epsilon}$	linearized strain tensor
$\mathbf{P}$	first Piola-Kirchhoff stress tensor
$\boldsymbol{\sigma}$	Cauchy stress tensor
N_{dim}	number of spatial dimensions
α_∞	attenuation function
$D(\zeta)$	damage distribution function
E_b	energetic cost of polymer chain failure
k_l/k_u	lower/upper constants
l	intrinsic length
Φ	specific energy per unit area
G_c	critical energy release rate

1. Introduction

This section gives an overview of both application fields and current limitations of elastomeric polymers and summarizes the main modeling approaches that have been put forth in the literature. Furthermore, formulations of non-local damage in the framework of elasticity are discussed.

1.1. Elastomeric polymers as structural materials

Elastomeric polymers have recently been identified as suitable structural materials in a wide range of applications, including shock mitigation as well as blast protection [El Sayed et al., 2009]. They have further been identified as promising in transparent armor applications, in which specific "ports" (transparent to visible and other wavelengths) need protection against foreign object impact [Albrecht et al., 2012]. In the following, details of the derivation and usage of one such elastomeric polymer, viz. polyurea, will be discussed. In addition, material failure characteristics and resulting current limitations will be reviewed. These form a basis for subsequent material modeling approaches.

1.1.1. Derivation and usage

Elastomeric polymers mark a group of materials with a long-standing tradition in the field of soft materials. Prime examples of their main characteristics include high damping capabilities as well as high stiffness-to-weight ratio. Moreover, lightweight mono-

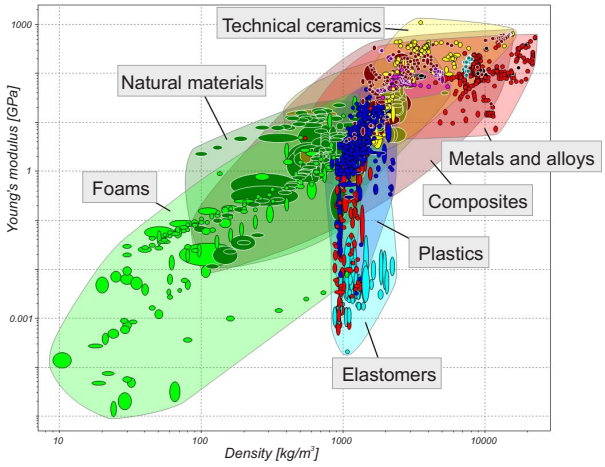

Figure 1.1.: Young's modulus versus mass density plot for different groups of materials, adapted from [Granta Design, 2014].

lithic coatings made of elastomeric polymers have also shown excellent mitigation properties in the event of powerful explosions, as well as the capability of retaining structural fragments produced by blast impact. They can easily be applied via spray-on or cast-on techniques, and different types of reinforcement and laminated designs have been investigated by several researchers [Colakoglu et al., 2007; Grujicic et al., 2006; Wambua et al., 2007]. A solution methodology for projectile impact on such structures was developed based on contact load duration, through-thickness and lateral transit times in [Lin and Fatt, 2006]. From their typical application as a protective coating of concrete and steel structures, it follows that such elastomeric coatings have to withstand rapid loadings such as during impact, collisions or explosions up to total failure of the material. An example of an elastomeric polymer used as a structural material is polyurea, an elastomer that is derived from the chemical reaction of an isocyanate component and a synthetic resin blend. Polyurea has been shown to exhibit beneficial properties for shock mitigation. In particular, it is characterized by a high strain rate sensitivity, large maximum deformations and good adhesion properties to many materials. These characteristics make it suitable for protective coatings on structures and have motivated its experimental characterization [Chakkarapani et al., 2006; Jiao et al., 2006, 2007, 2009; Knauss and Zhao,

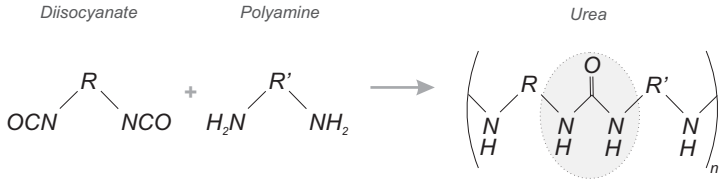

Figure 1.2.: Chemical reaction between an isocyanate component and a synthetic resin blend forming polyurea.

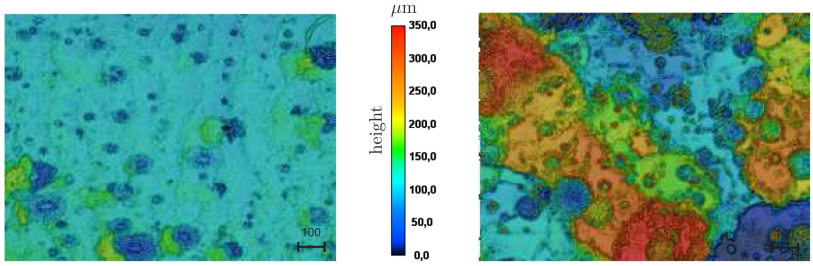

Figure 1.3.: Surface profiles (height measured from the deepest point) of a polyurea specimen tested in uniaxial tension Weinberg and Reppel [2013]. Left: Initial profile showing initial porosity. Right: Profile after fracture showing proliferation of voids.

2007; Roland and Casalini, 2007; Roland et al., 2007; Sarva et al., 2007].

With a quasistatic elastic modulus of about 70MPa [Knauss and Zhao, 2007], polyurea lies in the range of elastomers shown in Figure 1.1. However, as investigated in [Jiao et al., 2006, 2007, 2009], a ring-up in pressure due to wave propagation and reflection in thin material samples under pressure shear-plate impact loading greatly increases the material's strength.

1.1.2. Limitations and failure

The use of polymers as structural materials is critically limited by their tendency to degrade by distributed damage or to fail by fracture, sometimes in a brittle manner (cf., e. g., Andrews [1968]; Argon [2013]; Bikales [1971]; Grellmann and Seidler [2001]; Kausch

[1985]; Kinloch and Young [1983]; Williams [1984] for reviews). Damage in polymers deformed under tensile loading often takes the form of distributed voids [Jiao et al., 2006, 2007, 2009; Weinberg and Reppel, 2013], cf. Fig. 1.3. Voids nucleate heterogeneously from flaws or inclusions, Fig. 1.3a, and subsequently grow under tension, Fig. 1.3b, resulting in softening or loss of bearing capacity of the material (cf., e. g., Cho and Gent [1988]; Gent [1973]; Gent and Wang [1991]). Likewise, fracture in polymers can often be traced to the formation of crazes (cf., e. g., Donald and Kramer [1982]; Henkee and Kramer [1986]; Kausch [1983]; Kramer and Berger [1990]; Sanderson and Pasch [2004]), Fig. 1.4.

Crazes are thin layers of highly localized tensile deformation. Craze surfaces are bridged by numerous fine fibrils, themselves consisting of highly oriented chains, separated by connected voids. Crazes undergo several stages along their formation, including nucleation, growth and final breakdown, resulting in the formation of a traction-free crack, or fracture. Craze initiation is likely the result of heterogeneous cavitation at flaws loaded under conditions of high triaxiality. Craze propagation has been linked to a meniscus instability resulting in the formation of fibrils. This analogy is immediately suggestive of some role played by surface energy or other similar physical properties not accounted for by bulk behavior. Eventually, crazes break down to form cracks. Experimentally, crazes are easily identified and observed fractographically by a variety of techniques including optical interferometry, light reflectometry, dark-field electron microscopy, and others.

Owing to its engineering importance, polymer damage and fracture have been the focus of extensive modeling. A number of micromechanical and computational models, ranging from atomistic to continuum, have been put forth (cf., e. g., Baljon and Robbins [2001]; Basu et al. [2005]; Drozdov [2001]; Estevez et al. [2000a,b]; Krupenkin and Fredrickson [1999a,b]; Leonov and Brown [1991]; Reina et al. [2013]; Rottler and Robbins [2003, 2004]; Saad-Gouider et al. [2006]; Seelig and Van der Giessen [2009]; Socrate et al. [2001]; Tijssens and van der Giessen [2002]; Tijssens et al. [2000a,b]; Zairi et al.

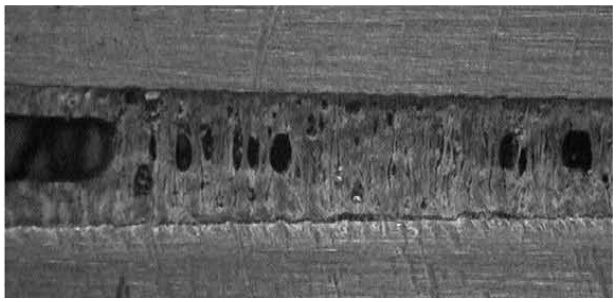

Figure 1.4.: Crazing process in a steel/polyurea/steel sandwich specimen under opening mode fracture [Yong et al., 2009].

[2008]). These models include consideration of nucleation and growth of voids, craze nucleation, network hardening and disentanglement, chain strength, surface energy and others, which account, to varying degrees, for the observational evidence and relate macroscopic properties to material structure and behavior at the microscale. In parallel, a large mathematical literature has evolved, discussing the possibility of cavitation in local models and nonlocal extensions which may ensure existence of minimizers; see, for example, Ball [1982]; Conti and DeLellis [2003]; Henao and Mora-Corral [2010]; James and Spector [1991]; Müller and Spector [1995].

Despite these advances, the connection between micromechanical properties and polymer fracture, and specifically any scaling laws thereof, has defied rigorous analytical treatment and characterization. Of special interest is the identification of optimal scaling laws relating the macroscopic behavior to micromechanical and loading parameters. Such optimal scaling laws are established by producing upper and lower bounds of a power-law type with matching exponents for all parameters in both bounds. Optimal scaling methods were pioneered by Kohn and Müller [1992] as part of their seminal work on branched structures in martensite, and have since been successfully applied to a number of related problems, including shape-memory alloys, micromagnetics, crystal plasticity, and others [Choksi et al., 1999; Conti, 2000; Conti and Ortiz, 2005; Kohn and Müller, 1992, 1994].

Fokoua et al. [2014a,b] have recently applied those analysis tools to ductile fracture of metals. They specifically considered the deformation, ultimately leading to fracture, of a slab of finite thickness subject to monotonically-increasing normal opening displacements on its surfaces. In addition, they posited two competing constitutive properties, namely sublinear energy growth and strain-gradient hardening. Sublinear growth (for comparison, the energy of linear elasticity exhibits quadratic growth) is a reflection of the work-hardening characteristics of conventional metallic specimens, and gives rise to well-known geometric instabilities such as the necking of bars, sheet necking, strain localization and others (cf., e. g., McClintock and Argon [1966]). In metals undergoing ductile fracture, this inherently unstable behavior is held in check by a second fundamental property of metals, namely strain-gradient hardening [Fleck and Hutchinson, 1993, 1997, 2001; Fleck et al., 1994]. Under these assumptions, Fokoua et al. [2014a,b] showed, through rigorous mathematical proofs, that ductile fracture emerges as the net outcome of two competing effects: while the sublinear growth of the energy in the large-body limit promotes localization of deformation to failure planes, strain-gradient plasticity stabilizes this localization process in its advanced stages, thus resulting in a well-defined specific fracture energy.

1.2. Models of polymer elasticity

The mathematical description of polymeric materials commonly occurs on two different scales. On the one hand, the framework of continuum mechanics (see Section A.2 for a brief review) is used to describe hyperelastic materials in the finite deformation range; on the other hand, an alternative approach derives from statistical mechanics by describing individual polymer chains. The latter approach for modeling polymers offers the advantage of being able to derive the free energy of an individual polymer chain from first principles only, whereas hyperelastic material models are more phenomenological in nature Gloria et al. [2013].

However, bridging these scales and relating energy densities in the continuum description to the energy of a network of polymer chains bears several difficulties. First and foremost, assumptions on the interactions between different chains are necessary to facilitate the analysis and pass from individual polymer chains to a network of chains. Furthermore, the way in which the total energy decomposes into the different contributions from the lower scales must be specified.

1.2.1. Macromolecular polymer models

Derived from their macromolecular structure, polymers can be modeled as ensembles of chains with energy $f(\lambda,\mathrm{T})$, where λ is the stretch of the relative position vector between the chain ends and T is the absolute temperature. Prime examples of both uncorrelated and correlated chain models are the freely jointed chain model (FJC) in a microcanonical ensemble formulation for Gaussian and non-Gaussian statistical approximations as well as the Kratky-Porod and wormlike chain (WLC) models as representatives of stiffer polymer models, see e.g. [Weiner, 2002].

The freely jointed chain model

The freely jointed chain model approximates a polymeric structure of total length l_t as an ideal chain of monomers possessing equal lengths l_m and directions that are uncorrelated to the neighboring ones, cf. Figure 1.5.

Based on the large number of monomers N in a polymer, the probability density of the relative endpoint position vector approaches a Gaussian distribution, which in three dimensions results in

$$p_{\mathrm{FJC}}(l_e) = \frac{p_0}{(\sqrt{2\pi}\sigma)^3} e^{-\frac{l_e^2}{2\sigma^2}} \tag{1.1}$$

with variance $\sigma = \sqrt{N l_m^2/3}$ and normalizing constant p_0. The total free energy of a single chain then follows as

$$f_{\mathrm{FJC}} = -k_B T \ln \Omega = f_{\mathrm{FJC}}^0 + \frac{3}{2} k_B T N \lambda_r^2, \tag{1.2}$$

where f_{FJC}^0 denotes the free energy of the undisturbed freely jointed chain, k_B and T are the Boltzmann constant and absolute temperature, respectively, Ω stands for the probability of obtaining a certain endpoint position and λ_r is the relative stretch of the chain as the end-to-end length l_e divided by l_t. For a graphical interpretation of the different lengths describing the polymeric structure, please refer to Figure 1.5. From Equation (1.2), the force-stretch relation of a single polymer chain can be calculated as

$$F_{\mathrm{FJC}} = \frac{3 k_B T}{l_m} \lambda_r. \tag{1.3}$$

This expression, however, is only valid in the small strain regime due to the Gaussian approximation with regard to changes in entropy [Weiner, 2002]. Following a non-Gaussian statistical approach (Kuhn and Grün [1942]) with probability

$$\Omega_{\mathrm{FJC}}(l_e) = \Omega_0 \exp\left(-N\left(\lambda_r L^{-1} + \ln \frac{L^{-1}}{\sinh(L^{-1})}\right)\right) \tag{1.4}$$

and recalling that $\lambda_r = l_e/l_t$, the free energy of a single chain follows as

$$f_{\mathrm{FJC}} = f_{\mathrm{FJC}}^0 + k_B T N (\lambda_r L^{-1} + \ln L^{-1} \sinh(L^{-1})^{-1}). \tag{1.5}$$

Furthermore, the force-stretch relation of a polymer chain, which is not restricted to the small strain regime, now specifies to

$$F_{\mathrm{FJC}} = \frac{1}{\beta l_m} L^{-1}(\lambda_r). \tag{1.6}$$

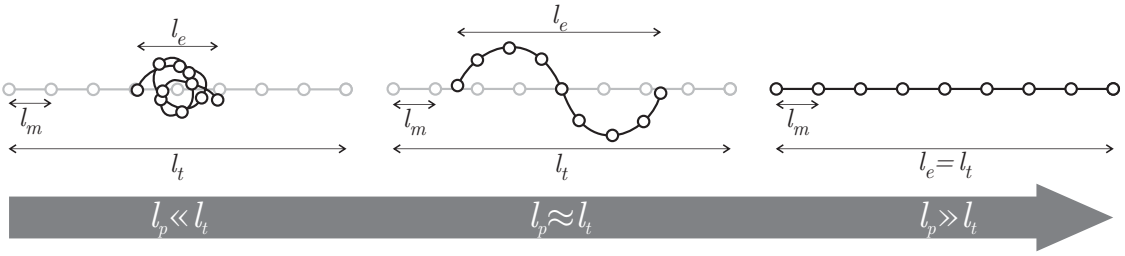

Figure 1.5.: Graphical interpretation of different length measures describing polymeric structures.

In these expressions, β is the reciprocal thermodynamic temperature according to $\beta = 1/k_B T$, and L^{-1} denotes the inverse Langevin function with

$$L(\lambda_r) = \coth(\lambda_r) - \lambda_r \, . \tag{1.7}$$

The inverse of Equation (1.7) can be restated using a Padé approximation [Miehe et al., 2004] resulting in

$$L^{-1} = \frac{3 - \lambda_r^2}{1 - \lambda_r^2} \lambda_r \, , \tag{1.8}$$

and it thus can be seen that in the small strain limit, the force-stretch relation based on Gaussian and non-Gaussian statistics coincide.

The wormlike chain model

The freely jointed chain model oversimplifies the macromolecular structure, resulting, e.g., in a non-existing stiffness against bond bending. Consequently, more elaborate models have been developed, which correlate the different chain segments.

The Kratky-Porod model for example introduces an energy dependency on the bonding angle, and thus penalizes chain rotations [Cross, 2006]. The free energy and force-stretch

relation of a single chain derived in this way take the forms, respectively,

$$f_{\mathrm{WLC}} = f^0_{\mathrm{WLC}} + \frac{k_B T l_t}{l_p}\left(\frac{1}{2}\lambda_r^2 + \frac{1}{4}\frac{1}{1-\lambda_r} - \frac{1}{4}\lambda_r\right) \quad \text{and} \tag{1.9}$$

$$F_{\mathrm{WLC}} \approx \frac{k_B T}{l_p}\left(\lambda_r + \frac{1}{4}\frac{1}{(1-\lambda_r)^2} - \frac{1}{4}\right), \tag{1.10}$$

with l_p denoting the persistence length as a measure of the stiffness of the tangled polymer chains.

1.2.2. From macromolecular to continuum scales

Approaches for bridging the scales between single polymer chains and cross-linked chain networks forming a continuum mainly differ by the set of assumptions on which they rely. A first and common assumption is that the sum over all free energies of the individual chains gives the total free energy of the polymer network [Gloria et al., 2013]. Further assumptions concern the specification of how isolated chains interact with each other, and different models are summarized below.

The Treloar model

First introduced by Treloar [1949], single chains are assumed to move in an affine manner according to the global deformation gradient (also known as the affine assumption or Cauchy-Born rule). The total strain energy density of the polymer network then follows as

$$W_{\mathrm{Treloar}}(\mathbf{F}) = \int_{\mathbb{R}^+}\int_{\mathbb{R}^+}\int_{S^2} W_{\mathrm{chain}}\left(l_t, \lambda_\zeta, N\right) d\sigma(\zeta)\, d\rho(l_t, N)\, d\nu(N), \tag{1.11}$$

where $\nu(N)$ specifies the distribution of polymer chains consisting of N monomers, and $\rho(l_t, N)$ describes the probability distribution of chains consisting of N monomers having length l_t in the undeformed configuration. Furthermore, S^2 denotes the unit sphere and $\zeta \in S^2$.

Simplifications to this model can be introduced by assuming that the number of monomers of each polymer chain is constant and that the total chain length in the undeformed configuration is given by $l_t = \sqrt{N} l_m$ [Flory, 1969]. Under these conditions, the total strain energy density of the network may be written as

$$W_{\text{Treloar}}(\mathbf{F}) = \int_{S^2} W_{\text{chain}}\left(\sqrt{N} l_m, \lambda_\zeta\right) d\sigma(\zeta). \tag{1.12}$$

The Arruda-Boyce model

In the large deformation limit, the Treloar model overestimates the energy stored in the material upon deformation. In order to remedy this deficiency, different ways of relaxing the affine assumption have been proposed in the literature. One of these models was introduced by Arruda and Boyce [1993], which relaxes the affine assumption by evaluating a representative volume element and its geometric response. Thereby, the representative volume element is a cube consisting of eight individual polymer chains originating from its center and connecting to each of its corners (see Figure 1.6 for reference).

The model rests upon the assumption that the representative volume element aligns itself based on the principal directions of the macroscopic deformation gradient and deforms according to its principal stretches (whereby no repulsion between polymer chains is taken into account) [Gloria et al., 2013]. Following this assumption, the total strain energy density is proportional to the energy of individual chains in the deformed representative volume element. By noting that the deformation ratio of each chain may be

calculated as

$$\frac{\lambda_{\text{chain}}}{l_t} = \sqrt{\frac{\lambda_1^2 + \lambda_2^2 + \lambda_3^2}{3}} = \sqrt{\frac{I_1}{3}} \tag{1.13}$$

with total chain length $l_t = \sqrt{3}/2$ in the undeformed configuration, the energy density of the polymer network (assuming isochoric deformations) may be written as

$$W_{\text{Arruda-Boyce}}(\mathbf{F}) = \frac{n}{\beta} N \left[\sqrt{\frac{I_1}{3}} \frac{\sqrt{N}l}{Nl} L^{-1}\left(\sqrt{\frac{I_1}{3}} \frac{\sqrt{N}l}{Nl} \right) \right. \tag{1.14}$$

$$\left. + \log\left(\frac{L^{-1}\left(\sqrt{\frac{I_1}{3}} \frac{\sqrt{N}l}{Nl} \right)}{\sinh L^{-1}\left(\sqrt{\frac{I_1}{3}} \frac{\sqrt{N}l}{Nl} \right)} \right) \right]. \tag{1.15}$$

Here, n denotes the chain density and, as introduced above, β stands for the reciprocal absolute temperature. In order to expand this energy and include volumetric effects, strain energies modeling the volumetric material response upon deformation may be added, such as the well-known Helmholtz volumetric energy [Weiner, 2002]

$$W_{\text{Helmholtz}}(\mathbf{F}) = \kappa\Big(J^2 - 1 - 2\log(J)\Big). \tag{1.16}$$

The variational model

A different way of relaxing the affine assumption lies in the introduction of a minimization principle (also known as the variational model) [Gloria et al., 2013], which rests upon the idea that the total free energy of the polymer is minimized by the positions of cross-linking points when the system reaches equilibrium. Starting from a macroscopic sample Ω consisting of a network of cross-linked polymer chains (whereby cross-links are assumed permanent and entanglements of chains are neglected), the Hamiltonian of

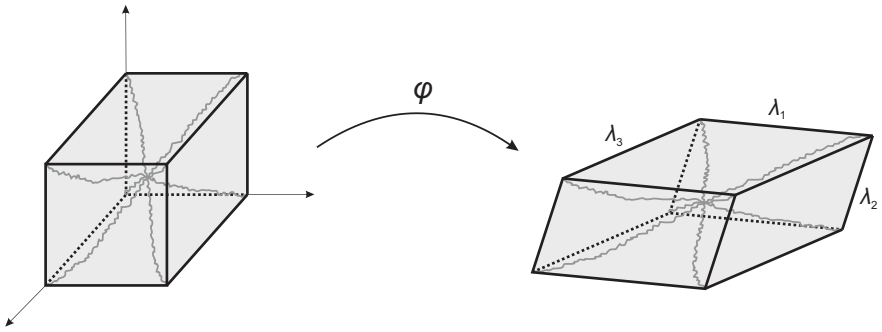

Figure 1.6.: Representative volume element used in the eight-chain-model [Arruda and Boyce, 1993].

the system follows as

$$H(u,s) = H_{\text{vol}}(u,s) + \sum_i H_i(u,s_i). \tag{1.17}$$

Here, u denotes the positions of cross-links, and s_i are the positions of monomers associated with chain i. Furthermore, the additive decomposition of the Hamiltonian enables a split into volumetric contributions H_{vol} and individual chain contributions H_i. The free energy of the variational model can then be stated as

$$A(\mathbf{F}) = -\frac{1}{\beta}\ln(Z), \tag{1.18}$$

with Z being the partition function according to

$$Z = \int_U \int_{S_1(u)} \int_{S_2(u)} \dots \int_{S_n(u)} e^{-\beta H(u,s)}\, ds_n \dots ds_2\, ds_1\, du. \tag{1.19}$$

In this expression, U and $S_i(u)$ are the sets of admissible positions of cross-links and monomers, respectively. Further simplifications introduced in the model are a restriction of chain interactions via cross-links only, as well as the assumption that monomer positions s_i are decoupled. These simplifications lead to a coarse-grained model that only

depends on cross-link positions u:

$$A(\mathbf{F}) = -\frac{1}{\beta}\ln\left(\int_U \exp^{-\beta H_{\mathbf{F}(u,\beta)}}\, du\right), \tag{1.20}$$

where

$$H_{\mathbf{F}}(u,\beta) = H_{vol}(u) - \sum_i \frac{1}{\beta}\ln\left(\int_{S_i(u)} \exp(\beta H_i(u,s_i))ds_i\right). \tag{1.21}$$

The Treloar assumption of a polymer network deforming affinely according to the macroscopic deformation gradient may be interpreted in this context as restricting the integral $\int_U$ in Equation (1.20) to evaluations at $u(x) = \mathbf{F}\cdot x$ only. In the variational model, however, the affine assumption only restricts the admissible set of cross-link positions U on the boundary, whereas the minimum of the coarse-grained Hamiltonian $A(\mathbf{F}) \simeq \inf_u H_{\mathbf{F}}(u,\beta)$ (with $\Omega \to \infty$ in the thermodynamic limit) gives the free energy in the interior.

In order to further specify $H_{\mathbf{F}}(u,\beta)$, the notion of a discrete network is introduced, and its main features and results for the variational model are summarized here (a more detailed description can be found in Gloria et al. [2013]). With a stochastic point process $\mathcal{L}$ in $\mathbb{R}^3$ as a sequence of random points in $\mathbb{R}^3$, and a Delaunay tesselation $\mathcal{T}$ of $\mathcal{L}$ in $\mathbb{R}^3$ specified by the tetrahedral mesh associated with $\mathcal{L}$, a scaling according to

$$\mathcal{L}_\epsilon = \epsilon\mathcal{L} \quad \text{and} \quad \mathcal{T}_\epsilon = \epsilon\mathcal{T} \tag{1.22}$$

can be introduced. The energy associated with a deformation field $u_\epsilon \in \mathcal{S}(\mathcal{T}_\epsilon)$ then follows as

$$A_\epsilon(u_\epsilon, D) = \epsilon^3 \sum_{e\in E} W_{nn}\left(|e_1 - e_2|, \frac{|u_\epsilon(\epsilon e_1) - u_\epsilon(\epsilon e_2)|}{\epsilon|e_1 - e_2|}\right) \tag{1.23}$$

$$+ \sum_{T\in\mathcal{T}} |\epsilon T| W_{vol}(\det\nabla u_\epsilon), \tag{1.24}$$

where $e = (e_1, e_2)$, W_{nn} and W_{vol} denote the edge between vertices, energy of the deformed edges and volumetric energy, respectively.

Now, only W_{nn} remains to be specified. By introducing N_e as the number of monomers per edge, and after some simplifications, the energy of the deformed edges follows as

$$W_{nn}(|e|, \lambda) = \frac{n}{\beta} N_e \left(\frac{\lambda}{\sqrt{N_e}} L^{-1}\left(\frac{\lambda}{\sqrt{N_e}}\right) + \log \frac{L^{-1}\left(\frac{\lambda}{\sqrt{N_e}}\right)}{\sinh L^{-1}\left(\frac{\lambda}{\sqrt{N_e}}\right)} \right), \tag{1.25}$$

which completes the model.

The Böl-Reese model

A similar approach to the variational model may be found in [Böl and Reese, 2005], in which both volumetric and polymer chain energies are considered. In this model, a tetrahedral mesh of a macroscopic sample Ω is generated.

Subsequently, the volumetric material response is associated with each tetrahedron of the mesh, whereas the edges of each element represent polymer bundles and thus introduce discrete energies associated with individual polymer chains.

For simplicity, the energies of polymer bundles are taken to be multiples of the energy of a single polymer chain. These energies can thus be written as a function $W_{\text{edge}}(\lambda_{\text{edge}}) = W_{\text{edge}}\left(\frac{l_{\text{edge}}}{L_{\text{edge}}}\right)$, whereby L_{edge} and l_{edge} denote edge lengths in the reference and deformed configurations, respectively.

With decreasing mesh size, the Böl-Reese model converges to a continuum model. However, it is important to note that the resulting model highly depends on the details of the tetrahedral mesh, as discussed further in Böl and Reese [2005].

Network theory of entropic elasticity

In a different framework originating from statistical mechanics, a standard description to go from single polymer chains to a network description is purely based on entropic contributions. Here, an amorphous network of cross-linked long-chain molecules is considered, and the undeformed configuration is given by a unit volume comprising a total of $\nu = 1,...,N$ cross-linked long-chain molecules, with respective numbers of links n_ν and link lengths b. Under the assumptions of sufficiently long chains which are far away from the fully extended limit, as well as a motion of cross-linking points according to superimposed deformations (neglecting thermal motion), the change in entropy of the amorphous network upon deformation can be written as [Weiner, 2002]

$$\Delta S_\nu = -\frac{3k_B}{2n_\nu b^2}\Big(r^2(\nu) - R^2(\nu)\Big). \tag{1.26}$$

In this expression, $\mathbf{R}(\nu)$ and $\mathbf{r}(\nu)$ denote the end-to-end vector of the νth chain before and after deformation, respectively (see Figure 1.7 for reference), and R and r denote their lengths, respectively. By further assuming the same affine transformation described in terms of the strain tensor $E_{IJ} = \frac{1}{2}(C_{IJ} - I_{IJ})$ for all cross-linking points (which is the affine assumption used in Treloar's model) and using the relation $r(\nu)^2 - R(\nu)^2 = 2E_{IJ}R_I(\nu)R_J(\nu)$, the total entropy of the system evaluates to

$$S(E_{IJ}) = -\frac{3kE_{IJ}}{b^2}\sum_{\nu=1}^{N}\frac{R_I(\nu)R_J(\nu)}{n_\nu}, \tag{1.27}$$

where the entropy of the undeformed network is taken as a reference point. A material tensor describing the undeformed configuration may be introduced as

$$K_{IJ} = \frac{3}{b^2}\sum_{\nu=1}^{N}\frac{R_I(\nu)R_J(\nu)}{n_\nu}, \tag{1.28}$$

which in the case of an homogeneous and isotropic undeformed network results in $K_{IJ} = K\delta_{IJ}$ with

$$K = \frac{1}{b^2} \sum_{\nu=1}^{N} \frac{R^2(\nu)}{n_\nu}. \tag{1.29}$$

For both E_{IJ} and K_{IJ}, the subscripts in uppercase letters refer to components of tensors in the reference configuration (as opposed to lowercase letters, which denote the deformed configuration as further described in Section A.2). Details regarding the evaluation of K and its dependence on the cross-linking process may be found in [Weiner, 2002], and the main results and assumptions are summarized below. Based on the observation that K describes the undeformed network of polymer chains, it can be seen that its value can only be specified further by details describing the cross-linking process. For simplicity, all cross-links between polymer chains are assumed to occur simultaneously and form at adjacent points of different chains. The total of N chains is furthermore subdivided into m groups, whereby each group consists of c_α chains having n_α links ($\alpha = 1,...,m$). With an end-to-end chain distance expressed by $R(p,\alpha)$ with $p = 1,...,c_\alpha$, it follows that

$$K = \frac{1}{b^2} \sum_{\alpha=1}^{m} \frac{1}{n_\alpha} \sum_{p=1}^{c_\alpha} R^2(p,\alpha). \tag{1.30}$$

Assuming a random cross-linking process, $R^2(p,\alpha)$ may be calculated via a Gaussian distribution with variance $n_\alpha b^2$ so that

$$\sum_{p=1}^{c_\alpha} R^2(p,\alpha) = c_\alpha n_\alpha b^2, \tag{1.31}$$

and thus $K = N$. Using these simplifications, Equation (1.27) may be restated as

$$S(E_{IJ}) = -k_B N E_{LL}, \tag{1.32}$$

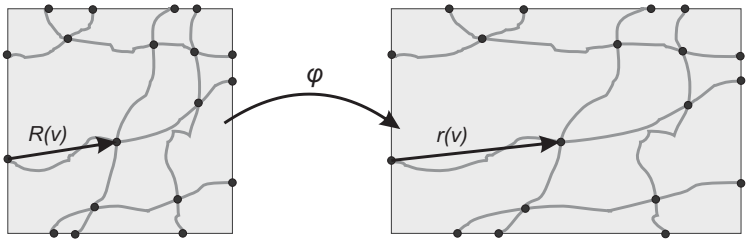

Figure 1.7.: Network of cross-linked polymer chains upon deformation (adapted from Weiner [2002]).

which can be reformulated in principal stretches as

$$S(\lambda_1, \lambda_2, \lambda_3) = -\frac{k_B N}{2} \sum_{L=1}^{3} (\lambda_L^2 - 1). \tag{1.33}$$

Finally, the Helmholtz free energy F of the full unit volume network subject to an arbitrary deformation requires the addition of an energy component $U(v, T)$, which depends on volumetric changes. The free energy of the amorphous network then follows as

$$F(\lambda_1, \lambda_2, \lambda_3, T) = U(v, T) + \frac{k_B T N}{2} \sum_{L=1}^{3} (\lambda_L^2 - 1), \quad \text{with} \quad v = \lambda_1 \lambda_2 \lambda_3. \tag{1.34}$$

In strain energy density form, and with an exemplary volumetric contribution $\hat{W}(J, T)$ added, we arrive at

$$W(\mathbf{F}, T) = \hat{W}(J, T) + \frac{kT}{2} K_{IJ} E_{IJ} = \hat{W}(J, T) + \frac{kTN}{2} \delta_{IJ} E_{IJ}. \tag{1.35}$$

This energy density is the basic representation of a *Neo-Hookean* solid, and it is furthermore the three-dimensional extension of Equation (1.2). Here and in the following, $\mathbf{F}$ denotes the deformation gradient tensor, and the Jacobian $J = \det \mathbf{F}$ represents the relative volumetric change.

1.3. Formulations of non-local damage

A number of non-local regularization models have been put forth in the literature in an attempt to overcome ill-posed boundary value problems arising in continuum damage models. Due to the presence of softening in these models, the governing field equations loose ellipticity, and a unique solution to the resulting algebraic system does not exist (as shown analytically for the case of wave propagation in a strain-softening bar in [Bažant and Belytschko, 1985]). As a result, deformations are observed to localize in narrow bands, with band widths restricted by the spatial discretization size.

Solution approaches to stabilize this process introduce an internal material length scale as well as non-local terms. Two main strategies can be distinguished in the introduction of non-local terms, which are of integral and gradient type. Prime examples of both approaches will be reviewed in this section. For a comprehensive review, see, e.g., [Bažant and Jirásek, 2002], which forms the basis for the following brief review.

1.3.1. Motivation

Nonpolar materials as discussed in [Noll, 1972] constitute a class of materials, for which the stress value at a given point depends on the deformation and temperature evaluated at this point only (and, in some cases, also the history of deformation). The underlying assumption that the material can be treated as a continuum even at an arbitrarily small scale implies the possibility of decomposing a finite body into infinitesimal material volumes whose interactions are restricted to the level of balance equations. This assumption, however, is an idealization, and neglects any internal material structure or microstructural details. Microstructural details may be described by spatial variations of material properties, yet their size range over different orders of magnitude renders this approach expensive in practical applications. More importantly, the continuum assumption breaks down at smaller scales and is hence no longer applicable . Therefore, it is important to

choose a resolution level below which the details of the internal structure are only indirectly taken into account as effective material properties. This continuum assumption is justified if the characteristic wave length of the deformation field does not lie below the material model's resolution level. For static applications, the characteristic wave length may be viewed as the minimum region size into which strain is able to localize. One way of avoiding the need for resolution refinement in the case of characteristic wave lengths below resolution level is to introduce generalized continuum formulations.

The first generalized continuum formulation can be found in [Cosserat and Cosserat, 1909], in which material particles have not only translational but also rotational degrees of freedom. These additional degrees of freedom are defined by rotations of a rigid frame of mutually orthogonal unit vectors. In the time that followed, generalizations of Cosserat's original theory were developed using additional fields independent of the displacement field. An example can be found in the continuum with microstructure [Mindlin, 1974], in which a microscopic deformation gradient is introduced (which gives, in the special case of orthogonal tensors, the previously described Cosserat micropolar continuum).

A different group of enriched continua (also known as higher-grade materials or gradient theories) is formed by constitutive models incorporating gradients of strain, thus keeping the displacement field as the only independent kinematic field. First, gradients of rotations were considered, which are the strain gradient components corresponding to curvature (see, e.g., [Grioli, 1960]). Afterwards, gradients of stretch were included into the theory [Toupin, 1962], as well as higher-order gradients [Green and Rivlin, 1964].

In addition to deviations from local constitutive models at small scales, which are based on microstructural heterogeneities on the characteristic length scale, different motivations of non-locality were proposed in the 1970s. The second main motivation was the strain-softening character of distributed damage. In the case of a local inelastic constitutive law with strain-softening damage, numerical as well as analytical results showed

localization of damage into a zone of zero volume [Bažant, 1976]. As a result, the numerical solution becomes unobjective with regard to the chosen mesh and converges, for decreasing mesh size, to a solution characterized by zero energy dissipation during failure. Two different reasonings can be given for this behavior, and for a one-dimensional dynamic problem, these reasons can be explained as follows:

- In the case of negative tangential stiffness, materials are characterized by an imaginary wave speed, and thus lose (apart from special cases of materials) the ability to propagate waves.
- The initial boundary value problem becomes ill-posed, and transitions from a hyperbolic to an elliptic type. Owing to this change in type, finite changes in the dynamic solution can result from infinitesimal changes in the initial conditions.

For multidimensional tangential stiffness tensors lacking positive definiteness, materials can still possess some real wave speeds and therefore propagate stress waves. The direction of stress propagation however is no longer arbitrary, resulting in ill-posed initial boundary value problems that are not necessarily of elliptic type. It has been shown in later investigations (please refer to [Bažant, 1976, 1984; Bažant and Cedolin, 1979; Bažant and Oh, 1983; Bažant et al., 1984; Cedolin and Bažant, 1980; Pietruszczak and Mròz, 1981] for details) that by introducing a characteristic length in order to model non-local strain softening behavior, the localization of damage can be prevented by regularizing the boundary value problem and making it well-posed. As a result, convergence to physically meaningful solutions is achieved.

A final motivation for the introduction of non-locality into constitutive theories is given by size effects. Here, the term size effects denotes the dependence of nominal strength on structure size. For purely local material behavior independent of a characteristic material length, size effects may be described by power laws (e.g. in linear elastic fracture mechanics). In case of non-locality on the other hand, size effects are of transitional

type, and different power laws are needed in order to describe size effects at scales much smaller/larger than the characteristic length.

The different motivations leading to an introduction of non-local behavior into constitutive theories can hence be summarized as follows:

- material heterogeneities leading to small-scale deviations from local continuum models,
- ill-posed initial boundary value problems, which arise in strain-softening damage formulations and lead to unobjective numerical solutions,
- size effects observed in experiments and discrete simulations.

1.3.2. Strong and weak non-locality

Two main strategies can be distinguished in the field of non-local regularization models, which are of integral and gradient type. The former category describes models in which non-local terms are included by introducing weighted averages of local internal variables, whereby averaging is performed over a set of neighboring points close to the point under consideration. In gradient-type approaches, on the other hand, the introduction of non-locality relies on higher-order gradients of non-local variables. Differential equations then describe the evolution of control variables, which allows for different ways for the non-local representation.

Following a mathematical description of non-locality [Rogula, 1982], an abstract form of the fundamental equations governing any physical theory can be expressed as

$$Au = f, \tag{1.36}$$

whereby f is a given excitation, u denotes the unknown response, and A is the corre-

sponding operator which characterizes the system and may possibly be non-linear. Since A characterizes the system, it also determines its locality properties. For A to be *local*, the following property must be satisfied:

Definition 1. *If two functions u and v are identical in an open set O, then their images Au and Av are also identical in O.*

In other words, whenever the identity $u(\mathbf{x}) = v(\mathbf{x})$ holds for all points $\mathbf{x}$ in a neighborhood of $\mathbf{x}_0$, then it also follows that $Au(\mathbf{x}_0) = Av(\mathbf{x}_0)$. This condition is satisfied for differential operators, and we may hence define local theories as those being fully described by differential equations. Non-local theories, on the other hand, are based on integrodifferential equations.

However, this definition of locality is of a somewhat narrow nature, and a different description relating to the absence or presence of a characteristic length can be given. In theories in which a characteristic length is absent, the fundamental equations are invariant under scaling of the spatial coordinates [Rogula, 1982]. Local theories satisfying this property are denoted *strictly local*, whereas local theories not invariant under spatial scaling are called *weakly non-local*. Typically, theories of the weakly non-local group contain differential equations with derivatives of different orders. By taking the ratio of coefficients multiplying these terms of different order (which have different physical dimensions), it is then possible to find a characteristic length.

As a simple example of weakly non-local theories, we may look at a Timoshenko beam, which relates to the previously mentioned Cosserat continuum as a specific one-dimensional version. In this case, the characteristic length is given by the ratio of the square roots of the bending and shear stiffness values of a cross-section. Under the assumption of a fixed cross-sectional shape, it follows that the characteristic length is proportional to the depth of a Timoshenko beam. Hence, only the beam span remains as an actual geometric dimension of the model, whereas the depth is described by means of a generalized

material model and given in terms of moment–curvature (or shear force to shear distortion) relations. Therefore, in this example the material length scale can be traced back to a geometric dimension that is not explicitly resolved anymore, viz. the beam's depth. Similarly, characteristic lengths in generalized continuum models are the result of a homogenization procedure; they thus represent characteristics of the heterogeneity, which are not explicitly resolved anymore.

In summary, continuum models may be classified according to:

- strictly local models (non-polar simple materials),
- weakly non-local models (polar and gradient theories),
- strongly non-local materials (models of integral type).

1.3.3. Non-local models of integral type

Non-local elasticity

As introduced in [Edelen and Laws, 1971; Eringen, 1972], non-local elasticity theories involve many different fields of non-local character (e.g. body forces, mass or internal energy), which made their application to real problems a challenging task. In further developments, theories of non-locality were reduced to only include a non-local character in their stress-strain relations, while keeping the local character of equilibrium and kinematic equations, as well as of the corresponding boundary conditions [Eringen and Kim, 1974]. More recently, a variational model has been developed [Polizzotto, 2001], which introduces the quadratic energy functional

$$W = \frac{1}{2} \int_V \int_V \boldsymbol{\varepsilon}(\mathbf{x}) \mathbf{C}_l(\mathbf{x}, \boldsymbol{\zeta}) \boldsymbol{\varepsilon}(\mathbf{x}) \, d\mathbf{x} \, d\boldsymbol{\zeta} \tag{1.37}$$

under the assumptions of small strains and linear elasticity. Here, $\boldsymbol{\varepsilon}(\mathbf{x})$ denotes the strain field and $\mathbf{C}_l(\mathbf{x},\boldsymbol{\zeta})$ is the elastic stiffness in a generalized form. In this form, locality is recovered for

$$\mathbf{C}_l(\mathbf{x},\boldsymbol{\zeta}) = \mathbf{C}_l(\mathbf{x})\delta(\mathbf{x}-\boldsymbol{\zeta}). \tag{1.38}$$

In the following, it is assumed that the generalized stiffness matrix satisfies the symmetry relations $\mathbf{C}_l = \mathbf{C}_l^T$ as well as $\mathbf{C}_l(\mathbf{x},\boldsymbol{\zeta}) = \mathbf{C}_l(\boldsymbol{\zeta},\mathbf{x})$. Furthermore, a macroscopically homogeneous body is considered, and stiffness coefficients as well as interactions between points $\mathbf{x}$ and $\boldsymbol{\zeta}$ are assumed to decay with increasing distance between them (also known as the attenuating neighborhood hypothesis). Due to these decaying properties, a modified generalized stiffness may be introduced as

$$\mathbf{C}_l(\mathbf{x},\boldsymbol{\zeta}) = \mathbf{C}_l\,\alpha(\mathbf{x},\boldsymbol{\zeta}), \tag{1.39}$$

where α denotes an attenuation function. Under the assumption of an infinite and isotropic body, α is only a function of the distance between points $\mathbf{x}$ and $\boldsymbol{\zeta}$ and hence follows from

$$\alpha(\mathbf{x},\boldsymbol{\zeta}) = \alpha_\infty(\|\mathbf{x}-\boldsymbol{\zeta}\|). \tag{1.40}$$

The attenuation function α_∞, which is also known as the non-local averaging function or non-local weight function, may further be assumed as a Gauss distribution function according to

$$\alpha_\infty(r) = \left(l\sqrt{2\pi}\right)^{-N_{dim}} \exp\left(-\frac{r^2}{2l^2}\right) \tag{1.41}$$

with number of spatial dimensions N_{dim} and length parameter l. In order to increase computational efficiency, attenuation functions with finite support may be chosen, such

as a polynomial bell-shaped function

$$\alpha_\infty(r) = c\left\langle 1 - \frac{r^2}{R^2} \right\rangle^2, \tag{1.42}$$

where the Macaulay brackets denote the positive part according to $\langle x \rangle = max(0, x)$.

Non-local averaging operator

The integral approach includes non-local terms by introducing weighted averages of local internal variables, whereby averaging is performed over a set of neighboring points close to the point under consideration [Dimitrijevic and Hackl, 2007]. An example of this approach can be found in [Červenka et al., 2005]. Here, a non-local field is defined as

$$\tilde{f}(\mathbf{x}) = \int_V \alpha(\mathbf{x}, \zeta) f(\zeta)\, d\zeta, \tag{1.43}$$

whereby $f(\mathbf{x})$ is an arbitrary local field, and $\alpha(\mathbf{x}, \zeta)$ is the chosen non-local weight function. Since non-local operators in softening materials should not influence a uniform field, the weight function is expected to comply with the normalization condition

$$\int_V \alpha(\mathbf{x}, \zeta)\, d\zeta = 1 \quad \forall \quad \mathbf{x} \in V. \tag{1.44}$$

As introduced in Section 1.3.3, the weight function only depends on the distance between two points $\mathbf{x}$ and ζ under the assumptions of isotropy and homogeneity of an infinite sample. Here, $\mathbf{x}$ is also denoted as a receiver point, whereas ζ is called the source point. A non-negative bell function is then usually chosen for $\alpha_\infty(r)$ in Equation (1.40). It is now possible to define a minimum distance r characterized by vanishing or negligible interaction weights, which is known as the non-local interaction radius R. The resulting region of radius R (centered at $\mathbf{x}$) gives the domain of influence of point $\mathbf{x}$. Cases for which this definition does not hold are locations in the vicinity of a boundary. Under these

circumstances, averaging is restricted to sections of the domain of influence that lie inside the body. Furthermore, a way of satisfying normalization conditions is a modification of weight function $\alpha(\mathbf{x}, \zeta)$ according to

$$\alpha(\mathbf{x}, \zeta) = \frac{\alpha_\infty(\|\mathbf{x} - \zeta\|)}{\int_V \alpha_\infty(\|\mathbf{x} - \zeta\|)\, d\zeta}. \tag{1.45}$$

With regard to numerical implementations, the non-local average at $\mathbf{x}$ is computed as a weighted sum over values at all integration points ζ that lie within R. Furthermore, as a main penalty of non-local models of integral type, the increased bandwidth of the stiffness matrix has to be taken into account. Linearization of the resulting set of equations is hence complicated, and computational efficiency impaired. The following section is therefore aimed at giving an overview of different approaches to the introduction of non-locality, viz. non-local models of gradient type.

1.3.4. Non-local models of gradient type

Gradient-type approaches to non-locality utilize higher-order gradients of the non-local variables. Differential equations then describe the evolution of said control variables, whereby different ways of the non-local representation can be chosen. One possibility lies in the introduction of an equivalent strain measure as shown in [Simone et al., 2003]. Following this strategy, calculations of the state of damage are based on the strain measure's non-local part. The resulting differential equation to be solved involves Laplacians of non-local variables, and integration can be performed by resorting to the principle of virtual work.

Alternatively, as in the works of [Nedjar, 2001] and [Makowski et al., 2006], a Laplacian term may also be introduced directly in the differential equation describing the evolution of the damage variable. Integration of the resulting system of equations then follows

from the principle of virtual power.

A different way of gradient-type enhancement of the free-energy functional is presented in [Dimitrijevic and Hackl, 2007], in which C^0 interpolation of the variables is preserved. In general, C^1 interpolation of the displacements is required if damage variable gradients are introduced, leading to cumbersome numerical implementations. However, by introducing a new variable serving the purpose of transporting values of inelastic variables across finite element boundaries, C^0 interpolation order of the variables can be preserved while introducing non-locality into the model [Dimitrijevic and Hackl, 2007]. As a result, an additional set of equations must be solved on the structural level. Under the assumptions of isotropy and scalar damage, the enhanced free energy function of this approach follows as

$$\tilde{\psi} = \frac{1}{2} f(d)\, \varepsilon_{ij} C_{ijkl} \varepsilon_{kl} + \frac{c_d}{2} \|\boldsymbol{\nabla}\varphi\|^2 + \frac{\beta_d}{2} (\varphi - \gamma_1 d)^2 , \tag{1.46}$$

where φ represents the non-local variable, and $f(d)$ is an appropriate function of scalar variable d measuring the state of damage. Furthermore, β_d penalizes the difference between non-local and local field, and c_d defines the degree of gradient regularization and internal length scale. Taking variations of the potential functional

$$\Pi = \int_\Omega \tilde{\psi}\, dV - \int_\Omega \mathbf{u} \cdot (\rho \mathbf{b})\, dV - \int_{\partial\Omega_\sigma} \mathbf{u} \cdot \mathbf{t}\, dA \tag{1.47}$$

with external loading per unit surface $\mathbf{t}$ and force per unit volume $\rho\mathbf{b}$ then gives, by further applying natural boundary conditions of vanishing non-local flux across boundaries, a second-order differential equation for the evolution of φ according to

$$\beta_d (\varphi - \gamma_1 d) - c_d \boldsymbol{\nabla}^2 \varphi = 0. \tag{1.48}$$

2. Analytical description of crazing mechanisms

This section describes a simple local model for the bulk behavior as introduced in [Heyden et al., 2014], which is based on the classical statistical mechanical treatment of freely-jointed polymer chains presented in Section 1.2, extended to account for chain failure. Furthermore, a model of nonlocal energy based on the assumption of isotropy and of linear growth of the strain-gradient elastic energy density is introduced, based on the use of fractional derivatives. Evidently, more elaborate statistical-mechanical models of polymer elasticity, failure and strain-gradient elasticity can be considered within the general framework developed here. However, models such as the ones described below suffice to illustrate the general framework. Further enhancements will be discussed in Section 6.

2.1. Competing constitutive effects

neo As introduced in Section 1.1.2, the modeling of competing constitutive properties in the form of sublinear energy growth and strain-gradient hardening was recently applied to the analysis of ductile fracture of metals Fokoua et al. [2014a,b]. The present section follows a similar strategy for polymers. Thus, it is posited that fracture in polymers results from a competition between distributed damage, due to progressive chain failure, and fractional strain-gradient elasticity. Moreover, the material behavior is assumed to have two components, local and nonlocal. The local behavior is characteristic of large material samples deforming uniformly, and it represents the configurational statistics of a polymeric chain network in the thermodynamic limit (cf., e. g., Flory [1989]; Weiner

[2002]).

We note that in general, damage is a time-dependent process governed by equations of evolution. In particular, for arbitrary loading paths, the rate of damage can be zero below a certain threshold, and non-zero when the threshold is attained. In order to simplify the analysis, the present analysis is restricted to monotonic and proportional loading processes for which damage accumulates continuously.

The classical network theory (for details, please refer to Section 1.2 and references therein) is thus extended by assuming that the chain bonds have a finite strength. When the strength of the chain is reached, the chain is assumed to fail and to subsequently have no load-bearing capacity. In this case, the behavior of the solid is characterized by an effective strain-energy density referred to as "deformation-theoretical" (an extensive account of deformation theory, as it applies to general inelastic solids, may be found in Martin [1975]). Therefore, this effective free energy combines the chain elasticity and the dissipation due to chain failure. As shown in the following, for large deformations, the deformation-theoretical free energy has zero growth; i. e., it is bounded from above and below by a constant.

Energies with sublinear growth relax to zero, i. e., they allow the material to fracture with zero expenditure of energy and thus fail to supply useful information about the fracture properties. As a way to hold this inherently unstable behavior in polymers undergoing fracture in check, a second fundamental property, viz. fractional strain-gradient elasticity, may be applied. Fractional strain-gradient elasticity refers to a generalization of conventional strain-gradient elasticity (cf., e. g., Hermann [1974]; Kröner [1968]; Maugin and Metrikine [2010]) in which the strain-energy density depends on fractional derivatives (cf., e. g., [Adams, 1975]) of the deformation gradient.

The need to consider fractional derivatives in the definition of the energy stems from the fact that conventional strain-gradient elasticity is too rigid to enable the type of deforma-

tions involving in the crazing mechanism and, hence, is incompatible with experimental observation. Thus, if the strain-energy density has at least linear growth in the second deformation gradient $\nabla^2 \boldsymbol{y}$, then, for all configurations of finite energy, $\nabla^2 \boldsymbol{y}$ is necessarily integrable and, hence, the deformation mapping $\boldsymbol{y}$ is continuous on almost every plane by Sobolev embedding (cf., e. g., [Adams, 1975]). This continuity of $\boldsymbol{y}$, in turn, precludes the formation of fibrils characteristic of the crazing mechanism, which necessarily entails discontinuous deformation mappings (hence leading to discontinuous displacements). By contrast, as shown in the following sections, the use of fractional derivatives removes sufficient rigidity from conventional strain-gradient elasticity to allow for crazing deformations, thus bringing the theory within the realm of experimental observation.

In the present context, fractional strain-gradient elasticity encodes key aspects of polymer behavior, such as surface and interfacial energy, not accounted for in the local model. The fractional strain-gradient elasticity of the polymer results in deviations from volume scaling, i. e., in nonlocal behavior and size dependency, in sufficiently small material samples. Under these conditions, polymer fracture emerges as the net result of two competing effects: while the zero growth of the local energy promotes localization of deformation to failure planes, or crazes, fractional strain-gradient elasticity stabilizes this process of localization, thus resulting in an orderly progression towards failure and a well-defined specific fracture energy.

2.2. Local behavior

One of the simplest models of the thermoelasticity of polymers, known as the network theory of rubber elasticity [Flory, 1989; Weiner, 2002] (as introduced in Section 1.2), regards the polymer as an amorphous network of cross-linked long-chain molecules. The chains are freely-jointed, long and far from full extension. In order to connect the behavior of the chains to the deformation of the continuum, the cross-linking points are

assumed to move affinely according to the local macroscopic deformation. In addition, the polymer is assumed to be ostensibly incompressible at the macroscale. The standard analysis (cf., e. g., Weiner [2002]) then gives the free-energy density per unit volume of the undamaged material as

$$A_{\text{loc}}(\boldsymbol{F}) = \begin{cases} nk_BTK_{IJ}C_{IJ}, & \text{if } \det(\boldsymbol{F}) = 1, \\ +\infty, & \text{otherwise,} \end{cases} \tag{2.1}$$

where n is the number of chains per unit volume, $\boldsymbol{F}$ is the local deformation gradient, $\boldsymbol{C} = \boldsymbol{F}^T\boldsymbol{F}$ is the right Cauchy-Green deformation tensor, k_B is Boltzmann's constant, T is the absolute temperature, and incompressibility (i. e. $\det(\boldsymbol{F}) = 1$) is enforced through a hard constraint.

In addition, the structure tensor $\boldsymbol{K}$ follows as

$$K_{IJ} = \frac{3l^2}{b^2}\int_{S^2} p(\boldsymbol{\xi})\xi_I\xi_J\, d\Omega, \tag{2.2}$$

where b is the link length, l is the end-to-end distance of the chains, ξ is the chain end-to-end unit vector, $p(\boldsymbol{\xi})$ is the fraction of chains in the ensemble having a chain end-to-end unit vector $\boldsymbol{\xi}$, S^2 is the unit sphere and $d\Omega$ is the element of solid angle.

The density $p(\boldsymbol{\xi})$ is subject to the normalization condition

$$\int_{S^2} p(\boldsymbol{\xi})\, d\Omega = 1. \tag{2.3}$$

For an isotropic distribution of chains, $p = \frac{1}{4\pi}$, we have

$$\int_{S^2} p(\boldsymbol{\xi})\xi_I\xi_J\, d\Omega = \frac{1}{3}\delta_{IJ}, \tag{2.4}$$

and Equation 2.2 reduces to

$$K_{IJ} = \frac{l^2}{b^2}\delta_{IJ}, \tag{2.5}$$

whence Equation (2.1) in turn reduces to the polyconvex strain-energy density of a Neo-Hookean solid. In principal directions, $\boldsymbol{C} = \mathrm{diag}(\lambda_1^2, \lambda_2^2, \lambda_3^2)$ and

$$K_{IJ}C_{IJ} = K_1\lambda_1^2 + K_2\lambda_2^2 + K_3\lambda_3^2, \tag{2.6}$$

where

$$K_I = \frac{3l^2}{b^2}\int_{S^2} p(\boldsymbol{\xi})\xi_I^2\, d\Omega. \tag{2.7}$$

Furthermore, application of the arithmetic mean-geometric inequality and incompressibility gives

$$K_1\lambda_1^2 + K_2\lambda_2^2 + K_3\lambda_3^2 \geq 3[(K_1\lambda_1^2)(K_2\lambda_2^2)(K_3\lambda_3^2)]^{\frac{1}{3}} = 3(K_1K_2K_3)^{\frac{1}{3}}. \tag{2.8}$$

Combining these inequalities leads to

$$A_{\mathrm{loc}}(\boldsymbol{F}) \geq 3(K_1K_2K_3)^{\frac{1}{3}}nk_BT \equiv A_0. \tag{2.9}$$

For an isotropic polymer, we additionally have $K_1 = K_2 = K_3 = l^2/b^2$ and

$$A_0 = \frac{3nk_BTl^2}{b^2} = A_{\mathrm{loc}}(\boldsymbol{I}). \tag{2.10}$$

The classical model of polymer elasticity just described can be extended to account for damage in the form of broken chains. Suppose that chains break when the end-to-end vector attains a critical stretch $\lambda_c > 1$, and that the failure of one chain costs energy in

the amount E_b. Thus, according to this criterion, a previously intact chain of end-to-end direction $\boldsymbol{\xi}$ fails when

$$\boldsymbol{\xi}^T \boldsymbol{C} \boldsymbol{\xi} = \lambda_c^2. \tag{2.11}$$

The state of damage of the network can be described by means of the damage distribution function

$$D(\boldsymbol{\xi}) = \begin{cases} 0, & \text{if the chains of end-to-end direction } \boldsymbol{\xi} \text{ are broken,} \\ 1, & \text{if the chains of end-to-end direction } \boldsymbol{\xi} \text{ are unbroken.} \end{cases} \tag{2.12}$$

The corresponding structure constant now depends on the state of damage via

$$K_{IJ}(D) = \frac{3l^2}{b^2} \int_{S^2} p(\boldsymbol{\xi}) D(\boldsymbol{\xi}) \xi_I \xi_J \, d\Omega, \tag{2.13}$$

and the free-energy density takes the form

$$A_{\text{loc}}(\boldsymbol{F}, D) = \begin{cases} nk_B T K_{IJ}(D) C_{IJ} + nf(D), & \text{if } \det(\boldsymbol{F}) = 1, \\ +\infty, & \text{otherwise,} \end{cases} \tag{2.14}$$

where

$$f(D) = \frac{3E_b l^2}{b^2} \int_{S^2} p(\boldsymbol{\xi})(1 - D(\boldsymbol{\xi})) \, d\Omega \tag{2.15}$$

is the total energy dissipated through chain-breaking. This dissipative term accumulates during deformation due to contributions from all polymer chains stretched beyond their critical limit.

For arbitrary local deformation histories $\boldsymbol{C}(t)$, the corresponding evolution $D(\boldsymbol{\xi}, t)$ of the

damage distribution function is governed by the rate-independent kinetics

$$D(\boldsymbol{\xi}, t) = \begin{cases} 1, & \text{if } \boldsymbol{\xi}^T \boldsymbol{C}(t')\boldsymbol{\xi} \leq \lambda_c^2 \quad \forall \quad t' \leq t, \\ 0, & \text{otherwise.} \end{cases} \tag{2.16}$$

However, for the present purpose, it suffices to confine attention to monotonic deformation processes such that the stretch $\sqrt{\boldsymbol{\xi}^T \boldsymbol{C}(t)\boldsymbol{\xi}}$ is monotonically increasing (or monotonically decreasing) in all directions. Of course, for practical applications, an extension to account for arbitrary load histories is desirable, but goes beyond the scope of the investigation here.

Also, in polymers undergoing crazing under predominantly tensile loading, the deformations leading to failure may be reasonably approximated as being monotonic. Under these conditions, the damage distribution function is determined as a function of the right Cauchy-Green deformation tensor $\boldsymbol{C}$, namely

$$D(\boldsymbol{\xi}, \boldsymbol{C}) = \begin{cases} 1, & \text{if } \boldsymbol{\xi}^T \boldsymbol{C}\boldsymbol{\xi} \leq \lambda_c^2, \\ 0, & \text{otherwise.} \end{cases} \tag{2.17}$$

The structure tensor $K_{IJ}(\boldsymbol{C})$ and the dissipated energy $f(\boldsymbol{C})$ follow likewise as a direct function of $\boldsymbol{C}$, namely

$$K_{IJ}(\boldsymbol{C}) = \frac{3l^2}{b^2} \int_{S^2} p(\boldsymbol{\xi}) D(\boldsymbol{\xi}, \boldsymbol{C}) \xi_I \xi_J \, d\Omega \tag{2.18}$$

and

$$f(\boldsymbol{C}) = \frac{3E_b l^2}{b^2} \int_{S^2} p(\boldsymbol{\xi})(1 - D(\boldsymbol{\xi}, \boldsymbol{C})) \, d\Omega. \tag{2.19}$$

The corresponding free energy density takes on the deformation-theoretical form

$$W_{\mathrm{loc}}(\boldsymbol{F}) = \begin{cases} nk_BTK_{IJ}(\boldsymbol{C})C_{IJ} + nf(\boldsymbol{C}), & \text{if } \det(\boldsymbol{F}) = 1, \\ +\infty, & \text{otherwise.} \end{cases} \tag{2.20}$$

Thus, as long as the deformation history remains monotonic, the free energy density of the polymer is indistinguishable from that of a thermoelastic solid.

2.3. Growth properties of the deformation-theoretical strain energy density

In order to make contact with macroscopic fracture properties, the growth properties of the deformation-theoretical free energy density $W_{\mathrm{loc}}(\boldsymbol{F})$, Equation (2.20), are of critical importance, cf. Section 3. Therefore, it is necessary to investigate the growth characteristics of $W_{\mathrm{loc}}(\boldsymbol{F})$ for large $\boldsymbol{C}$.

2.3.1. Upper bound

An upper bound can be constructed as follows. The estimate

$$\begin{aligned} K_{IJ}(\boldsymbol{C})C_{IJ} &= \frac{3l^2}{b^2}\int_{S^2} p(\xi)D(\xi,\boldsymbol{C})\xi^T\boldsymbol{C}\xi\, d\Omega \\ &\leq \frac{3l^2}{b^2}\int_{S^2} p(\xi)\lambda_c^2\, d\Omega = \frac{3l^2\lambda_c^2}{b^2} \end{aligned} \tag{2.21}$$

supplies a bound for the first term in $W_{\mathrm{loc}}(\boldsymbol{F})$, which represents the strain energy term. In order to estimate the damage energy, it is noted that

$$f(\boldsymbol{C}) = \frac{3E_bl^2}{b^2}\int_{S^2} p(\xi)(1 - D(\xi,\boldsymbol{C}))\, d\Omega \leq \frac{3E_bl^2}{b^2}\int_{S^2} p(\xi)\, d\Omega = \frac{3E_bl^2}{b^2}. \tag{2.22}$$

Combining the above estimates finally gives the constant upper bound

$$W_{\mathrm{loc}}(\boldsymbol{F}) \leq 3(E_b + k_B T \lambda_c^2)\frac{l^2}{b^2}. \tag{2.23}$$

2.3.2. Lower bound

The next step is to bound $W_{\mathrm{loc}}(\boldsymbol{F})$ from below for large $\boldsymbol{F}$. Evidently, $W_{\mathrm{loc}}(\boldsymbol{F})$ is, at least, the damage energy, i. e.,

$$W_{\mathrm{loc}}(\boldsymbol{F}) \geq nf(\boldsymbol{C}). \tag{2.24}$$

In terms of the principal stretches (with λ_i^2 being the eigenvalues of $\boldsymbol{C}$) Equation (2.17) leads to

$$1 - D(\boldsymbol{\xi}, \boldsymbol{C}) = \begin{cases} 1, & \text{if } \lambda_1^2\xi_1^2 + \lambda_2^2\xi_2^2 + \lambda_3^2\xi_3^2 \geq \lambda_c^2, \\ 0, & \text{otherwise,} \end{cases} \tag{2.25}$$

where $(\lambda_1, \lambda_2, \lambda_3)$ are the principal stretches. Suppose now that $\lambda_1 \geq \lambda_2 \geq \lambda_3$ and $|\boldsymbol{F}| = \sqrt{\lambda_1^2 + \lambda_2^2 + \lambda_3^2} \to +\infty$ while $\lambda_1\lambda_2\lambda_3 = 1$ for incompressibility. Suppose, in addition, that $\operatorname{essinf}(p) \geq p_{\min} > 0$, i. e., the chain density is positive in all chain directions. Then,

$$1 - D(\boldsymbol{\xi}, \boldsymbol{C}) \geq g(\boldsymbol{\xi}, \boldsymbol{C}) = \begin{cases} 1, & \text{if } \lambda_1^2\xi_1^2 \geq \lambda_c^2, \\ 0, & \text{otherwise} \end{cases} \tag{2.26}$$

and

$$f(\boldsymbol{C}) \geq = \frac{3E_b l^2}{b^2}\int_{S^2} p(\boldsymbol{\xi})g(\boldsymbol{\xi}, \boldsymbol{C})\, d\Omega = \frac{3E_b l^2}{b^2}\int_{S^2\setminus\{|\xi_1| \geq \lambda_c/\lambda_1\}} p(\boldsymbol{\xi})\, d\Omega, \tag{2.27}$$

and as $\lambda_1 \to +\infty$,

$$W_{\text{loc}}(\boldsymbol{F}) \geq 4\pi p_{\min} n \frac{3E_b l^2}{b^2}, \tag{2.28}$$

which establishes a constant lower bound for the deformation-theoretical strain energy density. The bound simply expresses the fact that, in the limit under consideration, all chains are likely to be broken under sufficiently large deformations.

2.3.3. Illustrative examples

The preceding bounds show that the deformation-theoretical strain energy density $W_{\text{loc}}(\boldsymbol{F})$ has zero growth, i. e., it saturates to a constant for sufficiently large deformations. Correspondingly, the first Piola-Kirchhoff stress decays to zero in the same limit. This behavior is illustrated in Fig. 2.1 through the example of a polymer deformed in uniaxial tension with $\boldsymbol{F} = \text{diag}(\lambda^{-1/2}, \lambda^{-1/2}, \lambda)$.

In the examples, the polymer is assumed isotropic, $p = \frac{1}{4\pi}$, and the chains fail at a critical stretch $\lambda_c = 2$. Two different examples of bond-binding energies are considered. Fig. 2.1a corresponds to a bond-binding energy $\frac{E_b}{k_B T} = 2$, or strong chains, whereas Fig. 2.1b corresponds to a bond-binding energy $\frac{E_b}{k_B T} = 0.2$, or weak chains.

The zero growth of the deformation-theoretical strain energy for large deformations is evident in both cases. However, the saturation value of the energy is attained from below in the case of strong chains, and from above in the case of weak chains. This difference of behavior is expected, as strong chains (respectively, weak chains) dissipate large (respectively, small) amounts of energy upon failure. We note that the strong chain condition $\frac{E_b}{k_B T} > 1$ (respectively, weak chain condition $\frac{E_b}{k_B T} < 1$) corresponds to the range $E_b > A_0$ (respectively, $E_b < A_0$), with A_0 from Equation (2.10).

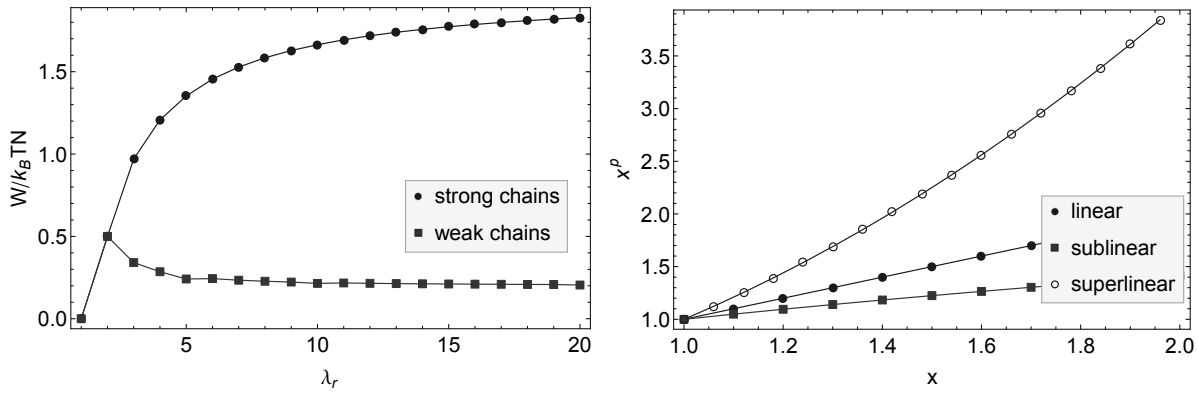

(a) (b)

Figure 2.1.: a) Deformation-theoretical strain energy density $W_{loc}(\mathbf{F})$ for an isotropic polymer deforming in uniaxial extension. The strong and weak chains both fail at a critical stretch $\lambda_c = 2$ and have bond-binding energies of $\frac{E_b}{k_B T} = 2$ and $\frac{E_b}{k_B T} = 0.2$, respectively. b) Schematic of functions with linear, sublinear and superlinear growth (reproduced from [Heyden et al., 2014]) .

2.4. Nonlocal regularization

Mathematically, energies exhibiting sublinear growth may be expected to relax to zero via strain localization to small volumes, a degenerate limit that provides no useful information about fracture properties (for a more detailed discussion, please refer to Section 1.3).

The present model rests on the assumption that this unstable behavior is stabilized by nonlocal or strain-gradient effects. For metals, this property has been extensively investigated and demonstrated by means of torsion tests in wires [Fleck et al., 1994], nanoindentation [Huang et al., 2000; Nix and Gao, 1998; Xue et al., 2000], and by other means. Specifically, for fixed local deformation, the energy density of solids is often observed to be an increasing function of the local strain gradient, or the second deformation gradient. This property results in deviations from volume scaling, i. e., in nonlocal behavior and size dependency, in sufficiently small material samples.

A first candidate means of accounting for strain-gradient effects, along the lines of Fok-

oua et al. [2014a,b], is provided by strain-gradient elasticity (cf., e. g., Hermann [1974]; Kröner [1968]; Maugin and Metrikine [2010]). This framework assumes an extended deformation-theoretical free energy density of the form $W(\boldsymbol{F}, \nabla\boldsymbol{F})$ with the limiting property that

$$W(\boldsymbol{F}, \boldsymbol{0}) = W_{\mathrm{loc}}(\boldsymbol{F}), \tag{2.29}$$

i. e., the local deformation-theoretical free energy density $W_{\mathrm{loc}}(\boldsymbol{F})$ is recovered for uniform deformations. The precise form of $W(\boldsymbol{F}, \nabla\boldsymbol{F})$ is unknown for most polymers. Conveniently, for purposes of optimal scaling only the growth properties of $W(\boldsymbol{F}, \cdot)$ are required. A hint at the likely growth properties of $W(\boldsymbol{F}, \cdot)$ is provided by observations of sharp twin interfaces in crystalline polymers deformed in shear [Agar et al., 1959; Alcazar et al., 2006; Geil, 1963; Keller, 1968; Kiho et al., 1964; Kovacs et al., 1969; Pradère et al., 1988; Reneker and Geil, 1960; Wittmann and Kovacs, 1970]. Atomistic simulations of shear deformation in polymers also provide evidence of lamination and of the development of sharp interfaces (cf., e. g., Fortunelli and Ortiz [2007]; Fortunelli et al. [2004] and references therein). Mathematically, sharp interfaces can only arise in strain-gradient elasticity if $W(\boldsymbol{F}, \nabla\boldsymbol{F})$ exhibits linear growth with respect to $\nabla\boldsymbol{F}$.

However, the strain-gradient framework just described has the deficiency of not allowing for crazing and, hence, is incompatible with experimental observation. Thus, if $W(\boldsymbol{F}, \nabla\boldsymbol{F})$ has linear growth in $\nabla\boldsymbol{F}$, then, for a configuration of finite energy, $\nabla^2\boldsymbol{y}$ is integrable and, hence, $\boldsymbol{y}$ is continuous [Adams, 1975]. The continuity of $\boldsymbol{y}$, in turn, precludes the formation of the fibrils characteristic of the crazing mechanism. It should be noted that, by contrast, the void-sheet mechanism characteristic of ductile fracture in metals is compatible with strain-gradient plasticity (cf. Fokoua et al. [2014a,b]).

The deficiency of conventional strain-gradient elasticity can be remedied by assuming instead an extended deformation-theoretical free energy density with growth controlled

by a fractional Sobolev seminorm $|D\boldsymbol{y}|_{W^{\sigma,1}(\Omega)}$ of the deformation gradient, with $0 < \sigma < 1$ (cf. Adams [1975] for a discussion of fractional Sobolev spaces, and for explicit formulas for the computation of the corresponding norms). Hereby, $|D\boldsymbol{y}|_{W^{\sigma,1}(\Omega)}$ still implies linear growth of the nonlocal energy density, but may be regarded as the integral of a fractional derivative $|D^{1+\sigma}\boldsymbol{y}|$ of the deformation gradient $D\boldsymbol{y}$. This assumption effectively weakens the strain-gradient effect sufficiently to allow for crazing deformations. In particular, it is shown in the sequel that, in fractional strain-gradient solids, the crazing mechanism indeed delivers an optimal bound of the energy in the sense of optimal scaling.

3. Optimal scaling and specific fracture energy

The goal of this section is to derive rigorous optimal scaling laws for the macroscopic fracture energy from the micromechanical model just described. Such optimal scaling laws are established by producing upper and lower bounds of a power-law type with matching exponents for all parameters in both bounds. In order to facilitate the analysis, it is assumed that the effective deformation-theoretical energy is additive in the first and second deformation gradients, with zero growth of the former and linear growth of the latter.

Consider the specific problem of a material sample in the form of an infinite slab of finite thickness subjected to prescribed opening displacements on its two surfaces. Under these conditions, optimal scaling laws for the dependence of the effective energy on cross-sectional area, micromechanical parameters, opening displacement and intrinsic length of the material are derived. In particular, the upper bound is obtained by means of a construction that mimics, in a particular simple manner, the crazing mechanism. The scaling laws thus derived supply a rigorous link between micromechanical properties and macroscopic fracture properties of polymers. In particular, they reveal the relative role that surface energy, chain elasticity, and damage play as contributors to the specific fracture energy of the material.

In addition, it is important to note that the optimal scaling laws derived in the sequel, which effectively bridge the micro and macroscales, do not depend on the fine details of the energy density but only on its growth properties for large deformations and deformation gradients. In this sense, the optimal scaling laws apply uniformly to classes of

material models having identical growth properties, and the fine details of the models can be conveniently ignored.

We recall that an energy functional $E(\cdot, \epsilon_1, \ldots, \epsilon_N)$, depending on N parameters $(\epsilon_1, \ldots, \epsilon_N)$, is said to exhibit optimal scaling if it satisfies matching upper and lower bounds of the form [Choksi et al., 1999; Kohn and Müller, 1992, 1994]

$$C_L \epsilon_1^{\alpha_1} \ldots \epsilon_N^{\alpha_N} \leq \inf E(\cdot, \epsilon_1, \ldots, \epsilon_N) \leq C_U \epsilon_1^{\alpha_1} \ldots \epsilon_N^{\alpha_N}, \tag{3.1}$$

where $C_L > 0$ and $C_U > 0$ are constants, and the exponents $(\alpha_1, \ldots, \alpha_N)$ are identical in both the lower and the upper bounds. The constants C_L and C_U appearing in Equation (3.1) provide rigorous lower and upper bounds and are not uniquely determined. Their precise values depend on the chosen strategy of the proof, and there is often a tradeoff between simplicity of the argument and the distance between C_L and C_U. By contrast, the exponents $(\alpha_1, \ldots, \alpha_N)$ are uniquely determined and represent intrinsic properties of the problem considered.

Rigorous optimal scaling laws for fractional strain-gradient solids with constant-linear energy growth of the type described in the foregoing have been derived by Conti et al. [2014]. In the following, the main arguments pertaining to the derivation of the optimal scaling laws are summarized, and their connection to fracture is discussed. The optimal scaling laws show that the materials under consideration do indeed fail by fracture, i. e., by localization of deformation to a plane, and that the fracture process requires the expenditure of a well-defined fracture energy, or critical energy-release rate, G_c.

3.1. Problem formulation

Based on the considerations in the preceding section, it is assumed that the deformation-theoretical free energy $E(\boldsymbol{y})$ obeys the growth properties

$$\int_\Omega W_L(\nabla \boldsymbol{y})\,dx + k_L \ell^\sigma |D\boldsymbol{y}|_{W^{\sigma,1}(\Omega)} \leq E(\boldsymbol{y}), \tag{3.2a}$$

$$E(\boldsymbol{y}) \leq \int_\Omega W_U(\nabla \boldsymbol{y})\,dx + k_U \ell^\sigma |D\boldsymbol{y}|_{W^{\sigma,1}(\Omega)}, \tag{3.2b}$$

where $0 < k_L \leq k_U < +\infty$ are constants,

$$W_L(\boldsymbol{F}) = \begin{cases} \min\{k_L, nk_BTK_{IJ}C_{IJ}\}, & \text{if } \det(\boldsymbol{F}) = 1, \\ +\infty, & \text{otherwise,} \end{cases} \tag{3.3}$$

and

$$W_U(\boldsymbol{F}) = \begin{cases} \min\{k_U, nk_BTK_{IJ}C_{IJ}\}, & \text{if } \det(\boldsymbol{F}) = 1, \\ +\infty, & \text{otherwise,} \end{cases} \tag{3.4}$$

are truncated local energy densities, $\ell > 0$ is an intrinsic or characteristic length, and $|D\boldsymbol{y}|_{W^{\sigma,1}(\Omega)}$ is a fractional Sobolev seminorm. Here, the structure tensor K_{IJ} corresponds to the undamaged material, as was defined in Equation (2.2). In addition, the density $p(\boldsymbol{\xi})$ is assumed to be such that the minimum of W_U and W_L is attained at the identity. The free energy of the polymer network is then denoted as

$$A_0 = \min W_U = \min W_L = W_U(\boldsymbol{I}) = W_L(\boldsymbol{I}). \tag{3.5}$$

For example, the isotropic density $p(\boldsymbol{\xi}) = 1/4\pi$ has the property described in Equation (3.5), and A_0 is given by Equation (2.10). However, it is important to note that the analysis is meaningful only if the truncated energy densities are not constant, resulting in the constraint $A_0 < k_L \leq k_U$ on the parameters. It should also be emphasized that the

deformation-theoretical free energy $E(\boldsymbol{y})$ itself does not have to be of the form expressed by the bounds in Equation (3.2), which merely define the growth properties of the energy.

In order to make connection with fracture, periodic deformations of a slab of thickness $2H$ occupying the domain $\{|x_3| \leq H\}$ and subject to prescribed opening displacements δ on its surfaces are considered. A periodic unit cell $\Omega = [0, L]^2 \times (-H, H)$ is identified, and the deformation of the slab is described by means of a $[0, L]$-periodic deformation mapping $\boldsymbol{y} : \Omega \to \mathbb{R}^3$ subject to the constraint of volume conservation in Ω and to displacement boundary conditions

$$y_3(x_1, x_2, -H) = -H - \delta, \tag{3.6a}$$

$$y_3(x_1, x_2, H) = H + \delta, \tag{3.6b}$$

with $(x_1, x_2) \in [0, L]^2$. The aim of the analysis is to derive optimal, or matching, upper and lower bounds for the energy of the slab as functions of L, ℓ and δ.

3.2. Upper bound

Owing to the minimum principle which governs the deformation theory of plasticity, an upper bound can be obtained simply by direct evaluation of the energy for an admissible test mapping. A deformation mapping that describes, in a simple manner, the process of crazing is considered here and shown schematically in Figure 3.2. The deformation is localized to the layer $(0, L)^2 \times (-a, a) \subset \Omega$ and, elsewhere, the slab undergoes a rigid translation through the prescribed opening displacement $\pm\delta$. The layer $(0, L)^2 \times (-a, a)$ is then subdivided into $\sim (L/a)^2$ identical cubes of size a. Figure 3.2 specifically depicts the deformation in one of the cubes.

The deformation is volume preserving and results in the formation of a fibril along the vertical axis of the cube by means of cavitation from the four boundary segments on the

symmetry plane of the cube. Furthermore, the deformation mapping $\nabla \boldsymbol{y}$ is integrable, though the second deformation gradient $\nabla^2 \boldsymbol{y}$ is not, as expected from the discontinuous nature of crazing on almost every plane. As noted above, this lack of integrability results in infinite energies in solids obeying strain-gradient elasticity. We relax this excessive rigidity of strain-gradient elasticity by assuming that the solid obeys fractional strain-gradient elasticity instead.

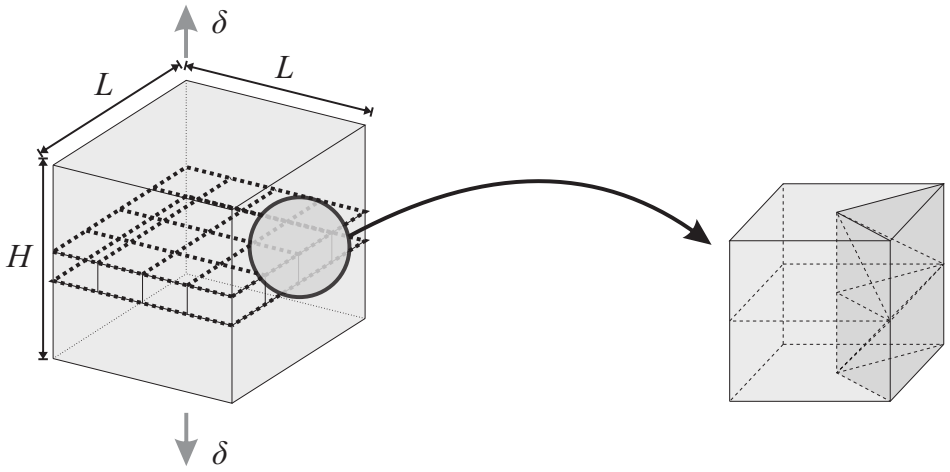

Figure 3.1.: Schematic of the crazing construction showing a slab divided into unit cells under prescribed opening displacements δ.

As mentioned above, the test deformation mapping outside the crazing region $(0, L)^2 \times (-a, a) \subset \Omega$ is chosen as a rigid translation, namely,

$$\boldsymbol{y} = \boldsymbol{x} + \delta \boldsymbol{e}_3, \text{ for } x_3 \geq a, \text{ and } \boldsymbol{y} = \boldsymbol{x} - \delta \boldsymbol{e}_3, \text{ for } x_3 \leq -a, \tag{3.7}$$

where $\boldsymbol{e}_3$ is the transverse unit vector. The local term can be immediately estimated to give A_0 on the entire volume plus a quantity bounded by k_U on the central region, totaling $2L^2 A_0 H + 2k_U L^2 a$. This gives the first two terms in (3.30). It can be remarked that, since the energy has zero growth, the details of the mapping are not needed to estimate the local part of the energy.

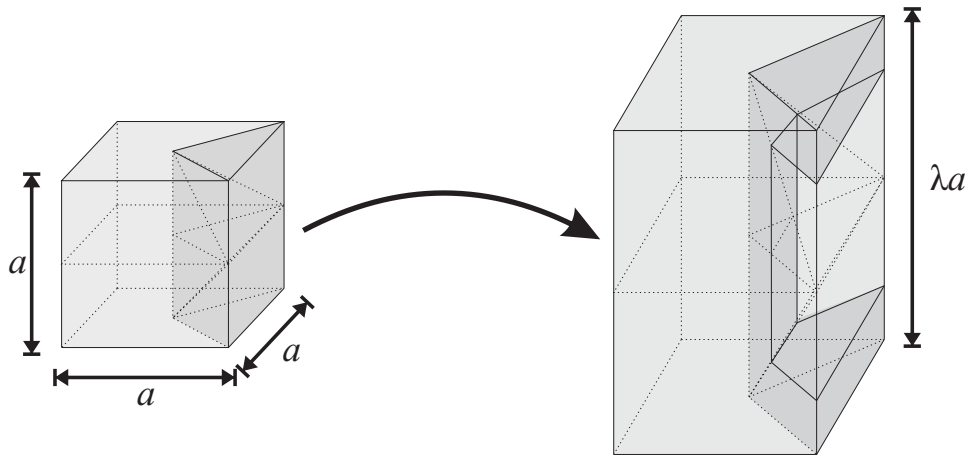

Figure 3.2.: Schematic of the deformation mapping (as shown for one periodic unit cell) used in the upper bound construction.

In order to estimate the nonlocal term, the mapping in $(0,L)^2\times(-a,a)$ must be constructed in detail. First, the layer is subdivided into $\sim L^2/a^2$ cubes of side length $2a$. It is then possible to focus on a single cube $C=(-a,a)^3$, the others being identical up to translations. Additionally, attention is confined to the prism $P=\{x_1\geq 0,\ -x_1\leq x_2\leq x_1, -a\leq x_3\leq a\}$, and the deformation mapping is extended to the remainder of the cube by symmetry. Specifically, the aim is to construct a volume-preserving mapping that opens a cavity around the segment $x_1=a$, $x_3=0$, through the composition of three elementary mappings. Each of these mappings is defined in the following.

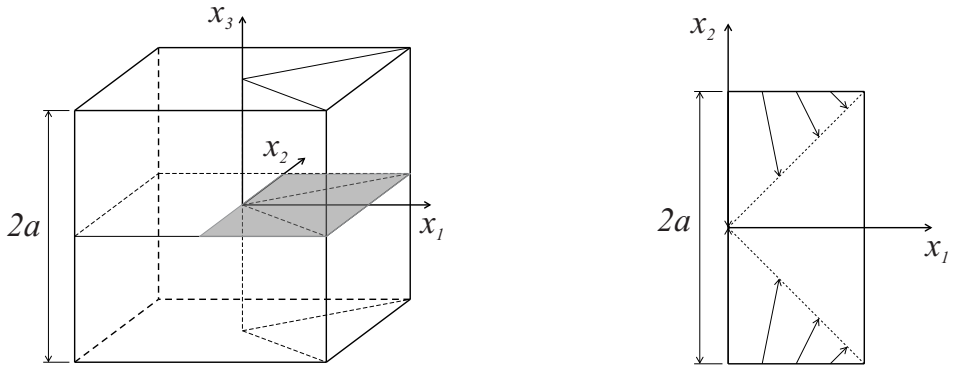

Figure 3.3.: Schematic of the first mapping $\boldsymbol{f}$ used in the upper bound construction.

To define a constant-determinant mapping $\boldsymbol{f}$ that collapses the half-cube $H = C \cap \{x_1 \geq 0\}$ into P (see Fig. 3.3), the class of mappings

$$f_1(\boldsymbol{x}) = h(x_1), \qquad f_2(\boldsymbol{x}) = \frac{x_2}{a} h(x_1), \qquad f_3(\boldsymbol{x}) = x_3, \tag{3.8}$$

subject to the ancillary conditions $h(0) = 0$ and $h(a) = a$ is considered. This class of mappings transforms planes $x_1 =$ constant to planes $y_1 =$ constant. Furthermore, with

$$\det(\nabla \boldsymbol{f}) = \frac{hh'}{a} = C, \tag{3.9}$$

where C is a constant, integrating once gives

$$h = \sqrt{2Cax_1}, \tag{3.10}$$

where the condition $h(0) = 0$ was used. From the second condition, $h(a) = a$,

$$\det(\nabla \boldsymbol{f}) = C = \frac{1}{2} \tag{3.11}$$

can be obtained and

$$f_1(\boldsymbol{x}) = \sqrt{ax_1}, \qquad f_2(\boldsymbol{x}) = x_2 \sqrt{\frac{x_1}{a}}, \qquad f_3(\boldsymbol{x}) = x_3. \tag{3.12}$$

This mapping is readily inverted to give

$$f_1^{-1}(\boldsymbol{y}) = \frac{y_1^2}{a}, \qquad f_2^{-1}(\boldsymbol{y}) = a\frac{y_2}{y_1}, \qquad f_3^{-1}(\boldsymbol{y}) = y_3. \tag{3.13}$$

Next, a second constant-determinant mapping is constructed, which opens up a prismatic cavity around the segment $x_1 = a$, $x_3 = 0$. To this end, attention is restricted to the sub-

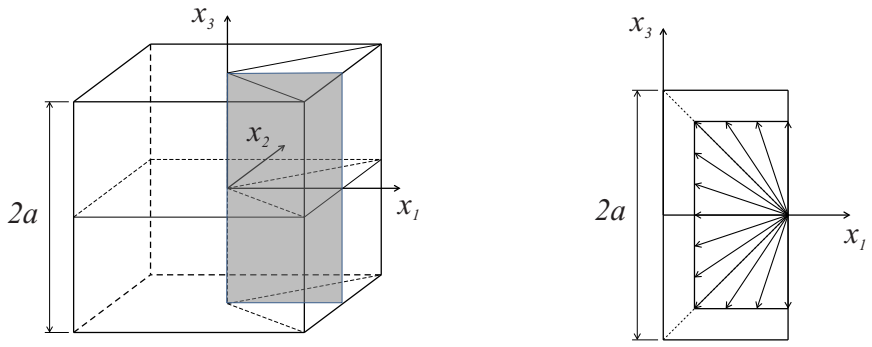

Figure 3.4.: Schematic of the second mapping $\boldsymbol{g}$ used in the upper bound construction.

domain $0 \le x_3 \le a - x_1$ and subsequently, the resulting mapping is extended to the region $x_3 \ge a - x_1$ by exchanging x_3 and $a - x_1$. Finally, the mapping is extended to the entire half-plane $x_1 \ge 0$ by reflection about the plane $x_3 = 0$. The specific class of mappings considered is

$$g_1(\boldsymbol{x}) = k(x_1), \qquad g_2(\boldsymbol{x}) = x_2, \qquad g_3(\boldsymbol{x}) = \frac{a - k(x_1)}{a - x_1} x_3, \tag{3.14}$$

subject to the ancillary condition $k(0) = 0$. This class of mappings transforms planes $x_1 =$ constant into planes $y_1 =$ constant. It follows that

$$\det(\nabla \boldsymbol{g}) = \frac{a - k}{a - x_1} k' = \frac{1}{\lambda}, \tag{3.15}$$

where $\lambda \ge 1$ is a constant. Integrating once and using the condition $k(0) = 0$ gives

$$ak - \frac{k^2}{2} = \frac{1}{\lambda}\left(ax_1 - \frac{x_1^2}{2}\right). \tag{3.16}$$

Solving for k gives, explicitly,

$$k(x_1) = a - \sqrt{a^2 - \frac{2}{\lambda}\left(ax_1 - \frac{x_1^2}{2}\right)}. \tag{3.17}$$

For $a - x_1 \le x_3 \le a$, the mappings used are

$$g_1(\boldsymbol{x}) = a - \frac{a - k(a - x_3)}{x_3}(a - x_1), \quad g_2(\boldsymbol{x}) = x_2, \quad g_3(\boldsymbol{x}) = a - k(a - x_3) \tag{3.18}$$

with the same function k. Finally, a volume-preserving deformation mapping that describes the formation of a fibril around the x_3-axis and that reduces to the identity on the planes $x_3 = \pm a$ can be defined through the composition of mappings

$$y_1 = f_1(\boldsymbol{g}(\boldsymbol{f}^{-1}(\boldsymbol{x}))), \quad y_2 = f_2(\boldsymbol{g}(\boldsymbol{f}^{-1}(\boldsymbol{x}))), \quad y_3 = \lambda f_3(\boldsymbol{g}(\boldsymbol{f}^{-1}(\boldsymbol{x}))), \tag{3.19}$$

where the factor λ represents a uniform extension in the x_3 direction. This operation completes the definition of the test deformation mapping. A direct computation gives, explicitly,

$$\begin{aligned} y_1 &= \sqrt{a^2 - \sqrt{a^4 - \lambda^{-1}(2a^2x_1^2 - x_1^4)}}, \\ y_2 &= \frac{y_1 x_2}{x_1}, \qquad y_3 = \frac{\lambda(a^2 - y_1^2)x_3}{a^2 - x_1^2}, \end{aligned} \tag{3.20}$$

over the domain $P \cap \{a|x_3| + x_1^2 \le a^2\}$, and

$$\begin{aligned} y_1 &= \sqrt{a^2 - \frac{a^2 - x_1^2}{x_3}\sqrt{1 - \lambda^{-1}(a^2 - x_3^2)}}, \\ y_2 &= \frac{y_1 x_2}{x_1}, \qquad y_3 = \lambda \operatorname{sign}(x_3)\sqrt{a^2 - \lambda^{-1}(a^2 - x_3^2)}, \end{aligned} \tag{3.21}$$

over the domain $P \cap \{ax_3 + x_1^2 \ge a^2\}$.

It is readily verified that $\det \nabla \boldsymbol{y} = 1$ everywhere, that the deformation mapping $\boldsymbol{y}$ satisfies the boundary conditions (3.7), that the two expressions match continuously at $|x_3| + x_1^2 = a$, and that $\boldsymbol{y}$ maps the planes $x_1 = \pm x_2$ and the plane $x_1 = a$ onto themselves and can therefore be extended to the rest of the slab by symmetry. It only remains to estimate the fractional norm. For the homogeneous $W^{\sigma,1}(\Omega)$ seminorm of a function $\boldsymbol{u} : \mathbb{R}^3 \to \mathbb{R}^m$, the

definition based on traces is used, viz.

$$|\boldsymbol{u}|_{\sigma,1} = \inf\left\{\int_0^\infty \int_{\mathbb{R}^3} \frac{|\partial_t \boldsymbol{f}| + |D\boldsymbol{f}|}{t^\sigma} dt : \boldsymbol{f}(0,\cdot) = \boldsymbol{u}\right\}; \tag{3.22}$$

see, for example, [Adams, 1975; Lunardi, 2009; Tartar, 2007]. Here, $\boldsymbol{f} : [0,\infty) \times \mathbb{R}^3 \to \mathbb{R}^m$ is an extension of $\boldsymbol{u}$, $D\boldsymbol{f}$ represents its distributional spatial derivative, and $\partial_t \boldsymbol{f}$ its distributional derivative in the new variable t.

Starting with the set $P_a = P \cap \{a|x_3| + x_1^2 \le a^2\}$, where $\boldsymbol{y}$ is defined by (3.20), a straightforward computation shows that in this set,

$$|D\boldsymbol{y}|(\boldsymbol{x}) \le \frac{ca\lambda}{a - x_1}. \tag{3.23}$$

By setting

$$\boldsymbol{f}(\boldsymbol{x}, t) = D\boldsymbol{y}(\boldsymbol{x}) \chi_{[0,a-x_1]}(t) \chi_{P_a}(\boldsymbol{x}), \tag{3.24}$$

it can be estimated from (3.22), after lengthy calculations, that

$$\|D\boldsymbol{y}\chi_{P_a}\|_{\sigma,1} \le \int_0^\infty \int_{\mathbb{R}^3} \frac{|\partial_t \boldsymbol{f}| + |D\boldsymbol{f}|}{t^\sigma} \, dx \, dt \le c\lambda a^{3-\sigma}. \tag{3.25}$$

Computation of the integral of $|D\boldsymbol{f}|$ can be performed using the fact that $D\boldsymbol{y}$ can be written as a sum of a finite number of terms, each of which is monotonic in each variable and obeys a bound of the type (3.23). In addition, the volume integrals are evaluated using Gauss' theorem, as done in Fokoua et al. [2014a,b].

Now, the remaining set, $P_b = P \cap \{ax_3 + x_1^2 \ge a^2\}$, is considered. The estimate (3.23) is replaced by

$$|D\boldsymbol{y}|(\boldsymbol{x}) \le \frac{c\,a^2}{x_3 y_1(\boldsymbol{x})}, \tag{3.26}$$

complemented by

$$y_1(\boldsymbol{x}) \geq \min\left\{\sqrt{\frac{ax_3 + x_1^2 - a^2}{x_3/a}}, \sqrt{\frac{a^2 - x_3^2}{2\lambda}}\right\}. \tag{3.27}$$

We define

$$\boldsymbol{f}(\boldsymbol{x}, t) = D\boldsymbol{y}(\boldsymbol{x})\chi_{[0,T(\boldsymbol{x})]}(t)\chi_{P_a}(\boldsymbol{x}), \qquad T(\boldsymbol{x}) = \sqrt{x_3(x_3 + x_1^2/a - a)}. \tag{3.28}$$

A careful treatment along analogous lines as above leads to an estimate similar to (3.25). Summing over the L^2/a^2 cubes leads to the conclusion that

$$\|D\boldsymbol{y}\|_{W^{\sigma,1}(\Omega)} \leq cL^2\lambda a^{1-\sigma}. \tag{3.29}$$

Recalling that $\lambda = 1 + \delta/a$ finally gives the second term in (3.30). Therefore, by inserting the deformation mapping from Equations (3.20) and (3.21) into Equation (3.2), the above calculations give an energy bound dependent on L, ℓ, δ and a,

$$E(\boldsymbol{y}) \leq 2L^2A_0H + 2k_UL^2a + ck_UL^2\ell^\sigma\frac{\delta}{a^\sigma}, \tag{3.30}$$

where c is a positive constant that depends on the details of the construction. Further minimizing the bound with respect to a results in $a \sim \delta^{1/(1+\sigma)}\ell^{\sigma/(1+\sigma)}$, and gives an upper bound of the form

$$E - 2L^2A_0H \leq c_Uk_UL^2\ell^{\frac{\sigma}{1+\sigma}}\delta^{\frac{1}{1+\sigma}}. \tag{3.31}$$

It can be noted that the bound takes the form of a power law in the variables L, ℓ and δ. The constant $2A_0L^2H$ is an inconsequential datum that reflects the normalization of the energy density.

3.3. Lower bound

Evidently, every choice of test deformation mapping produces an upper bound of the energy via Equation (3.2). However, Conti et al. [2014] showed, through arguments of mathematical analysis of a somewhat technical nature, that the upper bound given by Equation (3.31) is indeed optimal, in the sense that there exists a matching lower bound of the form

$$c_L k_L L^2 \ell^{\frac{\sigma}{1+\sigma}} \delta^{\frac{1}{1+\sigma}} \leq E - 2L^2 A_0 H, \tag{3.32}$$

with identical exponents of L, ℓ and δ. The key idea is to combine the fact that the local energy can only be small if the deformation is concentrated on a small part of the domain with a Poincaré inequality to control the L^1 norm of $D\boldsymbol{y}$ by its $W^{\sigma,1}$ norm. It should be noted that, while the constants c_L and c_U may be lax, owing, e. g., to the simplicity of the test deformation mapping used in the upper bound construction, the scaling exponents are hard and precise predictions of the theory. Furthermore, for the topological reasons discussed earlier, the constants necessarily blow up as σ approaches 1 from below, i. e., in the limit of conventional strain-gradient elasticity.

3.4. Relation to fracture

Considered jointly, the bounds in Equations (3.31) and (3.32) yield the optimal scaling law

$$c_L k_L L^2 \ell^{\frac{\sigma}{1+\sigma}} \delta^{\frac{1}{1+\sigma}} \leq E_{\min} - 2A_0 L^2 H \leq c_U k_U L^2 \ell^{\frac{\sigma}{1+\sigma}} \delta^{\frac{1}{1+\sigma}}. \tag{3.33}$$

We note that the bounds in Equation (3.33) scale with the in-plane area L^2, and are independent of the thickness $2H$ of the slab. This type of scaling is characteristic of fracture

processes, in which the deformation is concentrated in the neighborhood of a fracture surface, and the energy scales with the area of the surface. In particular, the specific energy per unit area

$$\Phi = \frac{E_{\min} - 2A_0 L^2 H}{L^2} \tag{3.34}$$

is bounded and independent of the thickness $2H$ of the slab. The bounds (3.33) can be recast in terms of this specific energy per unit area as

$$c_L k_L \ell^{\frac{\sigma}{1+\sigma}} \delta^{\frac{1}{1+\sigma}} \leq \Phi \leq c_U k_U \ell^{\frac{\sigma}{1+\sigma}} \delta^{\frac{1}{1+\sigma}}. \tag{3.35}$$

Now, for fixed ℓ and for the specific energy per unit area regarded as a function $\Phi(\delta)$ of the opening displacement, the corresponding applied normal traction then follows by the work-energy theorem as

$$\sigma = \frac{\partial \Phi}{\partial \delta} = \sigma(\delta). \tag{3.36}$$

This relation may be regarded as a cohesive law that relates opening displacement δ and traction σ. We recall that the attainment of a critical value of Rice's J-integral [Rice, 1968] provides a standard and widely used non-linear fracture criterion with several attractive properties (cf., e. g., Hutchison [1979]; Kanninen and Popelar [1985] for reviews): i) For linear elastic materials, J coincides with G, the elastic energy release rate; ii) for power-law small-strain plastic behavior, J determines the strength of the HRR singular field [Hutchinson, 1968; Rice and Rosengren, 1968] at the crack tip; and iii) it can be evaluated experimentally in a convenient manner. For an otherwise elastic material obeying a cohesive fracture law, an application of Rice's J-integral [Rice, 1968] gives the plane-strain critical energy release rate at crack growth initiation as

$$G_c = \int_0^{+\infty} \sigma(\delta)\, d\delta = \Phi(+\infty) - \Phi(0). \tag{3.37}$$

Inserting the upper bound (3.35) into (3.37) we find that the integral is indeed convergent at the origin, and a void nucleation model is not required in order to ensure the boundedness of G_c. By contrast, when inserting the lower bound (3.35) into (3.37), the same integral diverges at infinity; i. e., it predicts an infinite G_c. In order to eliminate this divergence, a cut-off δ_c can be introduced, representing a critical opening displacement at crack-growth initiation, and thus

$$G_c = \int_0^{\delta_c} \sigma(\delta)\, d\delta = \Phi(\delta_c) - \Phi(0). \tag{3.38}$$

In the present context, δ_c may conveniently be identified with the chain length of the polymer, on the grounds that failure must occur when the chains are stretched beyond their fully-stretched length. Inserting the bound (3.35) into (3.38) leads to

$$c_L k_L \ell^{\frac{\sigma}{1+\sigma}} \delta_c^{\frac{1}{1+\sigma}} \leq G_c \leq c_U k_U \ell^{\frac{\sigma}{1+\sigma}} \delta_c^{\frac{1}{1+\sigma}}, \tag{3.39}$$

which supplies bounds for G_c as a function of the internal length ℓ, the critical opening displacement δ_c and the material constants k_L and k_U. The bounds (3.39) supply a link between independently measurable material and fracture properties, and thus open the theory to experimental calibration.

4. Simulation of Taylor impact experiments

4.1. Numerical implementation

This section summarizes some algorithmic aspects of the solid mechanics solver used in the presented calculations. A full account of the theoretical foundations of the method and a number of convergence tests can be found in [Li et al., 2010, 2012; Pandolfi and Ortiz, 2012]. Some of the functional solver requirements in the investigation of materials under high impact loading conditions are the ability to transport mass efficiently, as well as having the capability of accounting for complex contact, deformation and failure patterns. To meet these requirements, the presented simulations in this work make use of the Optimal Transportation Meshfree (OTM) approximation schemes introduced by Li et al. [2010]. Furthermore, the OTM method is extended to account for fracture and failure by resorting to material point eigenerosion schemes [Li et al., 2010, 2012; Pandolfi and Ortiz, 2012].

4.1.1. Optimal transportation meshfree approximation

The optimal transportation meshfree (OTM) approximation schemes combine concepts of spatial and temporal discretization into a new method that is applicable to complex simulations meeting the requirements outlined above. On the one hand, concepts from optimal transportation theory (for example, the Wasserstein distance between consecutive mass densities) are used for the temporal discretization of the action integral. With

regard to spatial discretizations, on the other hand, maximum-entropy meshfree interpolation schemes from a nodal point set [Arroyo and Ortiz, 2006] are applied, which enables the simulation of unconstrained flows by avoiding continuous remeshing. It also prevents mesh entanglements, which will be beneficial for the simulations presented here. Finally, the OTM method uses material point sampling as a way of storing local state data and performing constitutive updates.

Overall, the method may hence be viewed as a way of restricting the optimal transport problem to mass densities, which are concentrated in material points and undergo motions in the form of piecewise linear trajectories (see Figure 4.2 for reference) [Pandolfi et al., 2014]. A detailed description of the OTM method may be found in [Li et al., 2010], and its main features and characteristics will be summarized (under the assumption of nonlinear elasticity) in the following. For extensions to general materials, variational constitutive updates may be applied.

The temporal discretization is based on discrete times $t_0, t_1, ..., t_{L-1}$, for which a semi-discrete action sum S_d can be written as

$$S_d(\boldsymbol{\varphi_1}, ..., \boldsymbol{\varphi_{L-1}}) = \sum_{k=0}^{L-1} \left[\frac{1}{2} \frac{d_W^2(\rho_k, \rho_{k+1})}{(t_{k+1} - t_k)^2} - \frac{1}{2} \left(U(\boldsymbol{\varphi_k}) + U(\boldsymbol{\varphi_{k+1}}) \right) \right] (t_{k+1} - t_k), \tag{4.1}$$

where deformation mapping and density at time t_k are denoted by $\boldsymbol{\varphi_k}$ and ρ_k, respectively. With $d_W^2(\rho_k, \rho_{k+1})$ defined as the Wasserstein distance between mass densities ρ_k and ρ_{k+1}, a measure of inertial action in the time interval $t_{k+1} - t_k$ is introduced in the form of

$$\frac{1}{2} \frac{d_W^2(\rho_k, \rho_{k+1})}{(t_{k+1} - t_k)^2} \tag{4.2}$$

in Equation (4.1).

The Wasserstein distance is defined by

$$d_W^2(\rho_k, \rho_{k+1}) = \inf \int |T(x) - x|^2 \rho_k(x)\, dx, \tag{4.3}$$

with T representing the optimal transference mass of ρ_k into ρ_{k+1}. Furthermore, U denotes the material's total internal energy according to

$$U(\boldsymbol{\varphi}) = \int_B \left[\rho\left(f\left(\boldsymbol{\nabla}\boldsymbol{\varphi}\right) - u\right) - \mathrm{tr}(\boldsymbol{\tau})\right] dx, \tag{4.4}$$

with isothermal local free energy density $f\,(\nabla\varphi)$, self-equilibrated stress field τ acting on the body and scalar body force potential u. In equilibrium, the relations

$$\boldsymbol{\nabla} \cdot \boldsymbol{\tau} = 0 \quad \text{in B} \tag{4.5}$$

and

$$\boldsymbol{\tau}\mathbf{n} = \mathbf{q} \quad \text{on } \partial_2\mathrm{B} \tag{4.6}$$

between self-equilibrated stress field $\boldsymbol{\tau}$ and applied tractions $\mathbf{q}$ holds. This approach to time discretization used in the OTM method enables geometrically exact updates of mass densities and local volumes. It is thus not necessary to solve a numerically cumbersome Poisson equation for pressure and, at the same time, mass conservation errors arising in Eulerian formulations are eliminated.

For the spatial discretization, all local state data is stored in a material point set, which evolves over time and also serves as the location of constitutive computations (see Figure 4.1 for reference). Material points are fix points of the body with designated mass and volume, which are convected via applied deformations. They furthermore represent integration points for the purpose of calculating effective nodal forces and masses. In order to define the spatial discretization approach, mass densities are approximated as

point masses via

$$\rho_{h,k}(\mathbf{x}) = \sum_{p=1}^{M} m_p \delta(\mathbf{x} - \mathbf{x}_{p,k}), \tag{4.7}$$

with index h denoting discretized quantities, $x_{p,k}$ is the position of a material point of mass m_p at time t_k, and $\delta(x - x_{p,k})$ being the Dirac-delta function centered at $x_{p,k}$. For the remaining part of the spatial discretization, the incremental deformation mapping is approximated as

$$\varphi_{h,k\to k+1}(\mathbf{x}) = \sum_{a=1}^{N} \mathbf{x}_{a,k+1} N_{a,k}(\mathbf{x}), \tag{4.8}$$

where $N_{a,k}(\mathbf{x})$ denote conforming shape functions defined at time t_k, and $(x_{a,k+1}, a = 1, ..., N)$ represents the nodal coordinate array at time t_{k+1}.

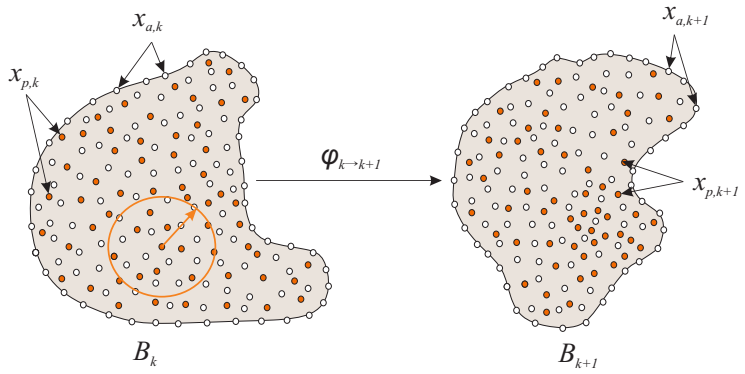

Figure 4.1.: Spatial discretization used in the optimal transportation meshfree approximation schemes (adapted from [Li et al., 2010]). Material points are shown in red, whereas nodal points are shown in white. An exemplary circular local neighborhood of nodal points is shown at time t_k.

In the presented calculations, maximum entropy (max-ent) shape functions are used and re-evaluated at every time step, which leads to a dynamic reconnection of material points and nodes. A further advantage of max-ent shape functions lies in their strong localization property [Arroyo and Ortiz, 2006], based on which shape function calculations at a material point $\mathbf{x}_{p,k}$ only involve a small neighborhood of nodes $N_{p,k}$. These local

neighborhoods of nodal points are dynamically updated via range searches in order to take relative motion between nodes and material points into account. As a result, there is no cost associated with remapping local states carried by material points, which is particularly useful in the case of inelastic solids involving local material states defined by internal variables. Furthermore, max-ent interpolation schemes are mesh-free and satisfy a Kronecker-delta property on the boundary. This spatial discretization feature simplifies the enforcement of essential boundary conditions, as well as offering good convergence, accuracy and monotonicity conditions.

By making use of the above approximations, a fully discrete action S_h follows as

$$\begin{aligned} S_h = \sum_{k=0}^{L-1} \sum_{p=1}^{M} (t_{k+1} - t_k) \Bigg[& \frac{m_p}{2} \frac{\left| \mathbf{x}_{p,k+1} - \mathbf{x}_{p,k} \right|^2}{(t_{k+1} - t_k)^2} \\ & - \frac{1}{2} \Big[m_p \left(\mathbf{f}_{p,k+1} - \mathbf{u}_{p,k+1} \right) - \operatorname{tr}(\boldsymbol{\tau}_{p,k+1}) \boldsymbol{\nu}_{p,k+1} \\ & + m_p (\mathbf{f}_{p,k} - \mathbf{u}_{p,k}) - \operatorname{tr}(\boldsymbol{\tau}_{p,k}) \boldsymbol{\nu}_{p,k} \Big] \Bigg], \end{aligned} \tag{4.9}$$

with abbreviations $\boldsymbol{\tau}_{p,k} = \boldsymbol{\tau}(\mathbf{x}_{p,k})$, $\mathbf{f}_{p,k} = \mathbf{f}\left(\nabla \boldsymbol{\varphi}_{h,k}(\mathbf{x}_{p,k}) \right)$ and $\mathbf{u}_{p,k} = \mathbf{u}(\mathbf{x}_{p,k})$. Hamilton's principle of stationary action finally gives the discrete trajectories

$$\delta S_h = 0. \tag{4.10}$$

The OTM scheme is solved in a forward-explicit fashion following the usual structure of updated-Lagrangian schemes and using forward time integration. Similar to other material point methods, optimal transportation meshfree approximation schemes offer the advantage of allowing nodal points of different bodies to be members of the same local neighborhood of a material point. Based on the cancellation of linear momentum, this feature of the OTM method automatically enables dynamic contact interactions of seizing type.

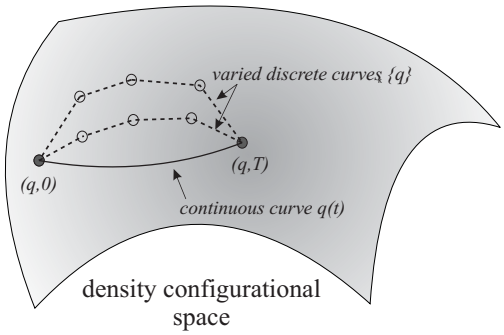

Figure 4.2.: Time discrete Lagrangian dynamics (adapted from [Li, 2009]).

4.1.2. Material failure

In the sequel, material failure will be modeled for a viscoelastic body occupying a three-dimensional domain $\mathcal{B}$. The boundary $\partial\mathcal{B}$ of the body consists of an exterior boundary $\mathcal{S}$, corresponding to the boundary of the uncracked body, and a collection of cracks, voids and tears jointly defining a crack set $\mathcal{C}$. In addition, $\mathcal{S}$ partitions in the usual manner into a displacement boundary $\mathcal{S}_1$ and a traction boundary $\mathcal{S}_2$. The body undergoes deformations under the action of body forces, displacements prescribed over $\mathcal{S}_1$, and tractions $\bar{\mathbf{T}}$ applied over $\mathcal{S}_2$. Under these conditions, the total potential energy of the body is

$$E(\boldsymbol{\varphi}, t) = \int_{\mathcal{B}\backslash\mathcal{C}} W\left(\nabla\boldsymbol{\varphi}(x,t), t\right) dV - \int_{\mathcal{S}_2} \bar{\mathbf{T}}(x,t) \cdot \boldsymbol{\varphi}\, dS \tag{4.11}$$

where $\mathcal{B}\backslash\mathcal{C}$ denotes the domain of the body with the crack set excluded, dV and dS are the elements of volume and area, respectively. Function

$$W(\nabla\boldsymbol{\varphi}, t) = W(\mathbf{F}, \mathbf{e}_1^i(t), \ldots, \mathbf{e}_N^i(t)) \tag{4.12}$$

is the free energy density of the body (to be specified in the following), $\bar{\mathbf{T}}$ is the applied traction, and $\boldsymbol{\varphi} : \mathcal{B}\backslash\mathcal{C} \to \mathbb{R}^3$ is the deformation mapping.

In addition, we must have

$$\boldsymbol{\varphi}(\mathbf{x}, t) = \bar{\boldsymbol{\varphi}}(\mathbf{x}, t) \quad \forall \quad \mathbf{x} \in \mathcal{S}_1, \tag{4.13}$$

where $\bar{\boldsymbol{\varphi}}$ is the prescribed value of the deformation mapping over the displacement boundary. The explicit dependence of E on t in (4.11) implies the evolution of inelastic strains as well as the time dependence of forcing terms, which are the prescribed displacements and forces. The equilibrium displacement field for a crack set $\mathcal{C}$ at time t may then be found by minimizing energy (4.11) over an appropriate space of functions.

If the material is not only allowed to deform viscoelastically but may also fail by extending the crack set $\mathcal{C}$, a monotonicity constraint representing the irreversible character of material failure is introduced as

$$\mathcal{C}(t) \subset \mathcal{C}(t + \Delta t). \tag{4.14}$$

Hereby, the monotonicity constraint merely describes the fact that later crack sets must contain earlier crack sets. Furthermore, crack extension follows unilateral contact constraints, and the crack set (or parts of it) are allowed to be closed at any given time.

Since the implementation of unilateral contact constraints is numerically challenging, calculations presented in the following are based on assuming the erosion of material points in a state of volumetric expansion only. Furthermore, previously eroded material points can be reinstantiated if a state of volumetric compression is attained, leading to crack closure.

Crack propagation then results from two competing material properties, viz. viscoelasticity and critical energy release rate G_c. The former promotes fracture in order to release energy, whereas the latter penalizes fracture (proportional to the area of the crack set). The competition between material failure and viscoelasticity for energy supplied by ex-

ternal forces is modeled via an energy-dissipation functional

$$F(\boldsymbol{\varphi}, \mathcal{C}, t) = E(\boldsymbol{\varphi}, t) + G_c|\mathcal{C}|. \tag{4.15}$$

Here, $|\mathcal{C}|$ denotes the crack set area. By minimization of the energy-dissipation functional (4.15) at every time, while taking the kinetic equations of the internal processes and and monotonicity constraints (4.14) into account, the state of deformation and failure can be calculated.

Unfortunately, minimization of the energy-dissipation functional (4.15) $F(\boldsymbol{\varphi}, \mathcal{C}, t)$ with respect to the crack set $\mathcal{C}$ is numerically challenging. We therefore resort to the variational eigenfracture scheme introduced by Schmidt et al. [2009] and its extension to eigenerosion of material points [Pandolfi and Ortiz, 2012]. The theory of eigenfracture uses an arbitrary eigendeformation field ϵ^* in order to define the crack set

$$\mathcal{C} = \{\epsilon^* \neq 0\}. \tag{4.16}$$

By introducing eigendeformations into the kinematics of crack propagation, the energy is relaxed locally, and the displacement field can include jumps without any cost of local elastic energy [Pandolfi et al., 2014]. For all material points at a distance ϵ or less away from the crack set $\mathcal{C}$ (whereby ϵ is a small length parameter) an ϵ-neighborhood of $\mathcal{C}$ may be defined. With ϵ-neighborhood volume $|\{\epsilon^* \neq 0\}_\epsilon|$, a surface measure of the crack follows as

$$|\mathcal{C}|_\epsilon = \frac{1}{2\epsilon}|\{\epsilon^* \neq 0\}_\epsilon|. \tag{4.17}$$

Here, ϵ^{-1} is a scaling factor that acts as a penalty factor for the crack set volume, converging to a surface in the limit [Pandolfi et al., 2014]. As shown in [Schmidt et al., 2009], the eigenfracture scheme converges to Griffith fracture solutions for the limiting case of

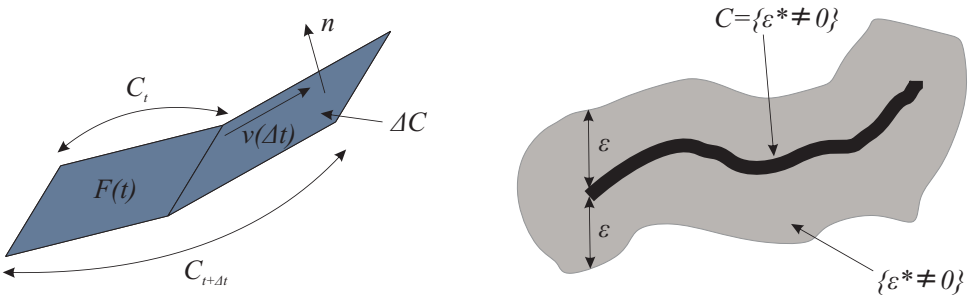

Figure 4.3.: Left: Advancing crack showing a zoom of the crack front propagating in the direction of crack front velocity v (adapted from [Pandolfi and Ortiz, 2012]). $\mathcal{C}(t)$ and $\mathcal{C}(t+\Delta t)$ are the original and extended crack set, respectively. Right: Set of eroded material points forming a crack and respective ϵ-neighborhood.

infinitesimal mesh sizes. For an arbitrary eigendeformation field taken as piecewise constant over the set of elements or material points under consideration, eigendeformations may either be zero (and thus minimize the attendant fracture energy), or cancel any local deformations (which in turn renders the elastic energy zero). Fig. 4.3 illustrates an advancing crack set and the ϵ-neighborhood.

The material point eigenerosion scheme uses a local energy-averaging procedure in order to approximate the necessary energy release rate for material point failure. For cases in which the estimated energy release rate exceeds the material's specific fracture energy, material points are eroded, and the collection of eroded material points in turn represents the crack set. Therefore, the material point eigenerosion scheme reduces the discrete crack-tracking problem to a successive failure of material points for cases in which a positive net gain in energy can be achieved, viz. cases with lower cost in fracture energy compared to the attendant elastic energy release. The algorithm used in the implementation of the material point eigenerosion scheme is summarized in Algorithm 1.

At every OTM step, the determination of the next material points to be eroded follows from sorting material points experiencing tensile states p in a priority queue based on the

Algorithm 1 Crack-tracking scheme for material point discretization [Pandolfi and Ortiz, 2012]

Require: Crack set C_k at the end of time step t_k
Require: Material state at all material points at the end of OTM time step t_{k+1}
Require: Priority queue PQ of real numbers ordered from largest (highest priority) to smallest (lowest priority).
  Set PQ = empty.
  Set $C_{k+1} = C_k$.
  for *all material points p not in* C_{k+1} *and in tensile stress state* **do**
    Compute elastic energy release $-\Delta E_p$.
    Compute effective crack area increment: ΔA_p.
    Compute net energy gain: $-\Delta F_p = -\Delta E_p - G_c \Delta A_p$.
    If $-\Delta F_p \geq 0$, push p into PQ.
  if $PQ \neq$ *empty* **then**
    Pull all material points K with net energy gain $-\Delta F_K > 0$ from PQ, add to C_{k+1}.
  else
    Exit.

energetic difference

$$-\Delta F_p = -\Delta E_p - G_c \Delta A_p > 0, \tag{4.18}$$

where $-\Delta E_p$ is the corresponding elastic energy release, and $G_c \Delta A_p$ denotes the fracture energy cost. In order to approximate the energy release rate related to material point erosion, first-order asymptotic formulae for notches are used, and the energy release rate is calculated as the elastic energy stored in the material point [Pandolfi et al., 2014].

Figure 4.4 shows a two-dimensional example of the ϵ-neighborhood construction. Each neighborhood V_ϵ^p contains all material points that lie inside a circular region of radius ϵ centered at the material point under consideration. For a propagating crack set $\mathcal{C} = \{\epsilon^* \neq 0\}$ consisting of eroded material points, the spherical neighborhood V_ϵ^p of each newly-failed material point is therefore included in the ϵ-neighborhood of $\mathcal{C}$, i.e., $\{\epsilon^* \neq 0\}_\epsilon$. The crack advance ΔA_p for a single material point p may then be computed as

$$\Delta A_p = \frac{1}{2\epsilon} \left(|\{\epsilon^* \neq 0\}_\epsilon|^p - |\{\epsilon^* \neq 0\}_\epsilon| \right) = \frac{1}{2} \Delta V_\epsilon^p, \tag{4.19}$$

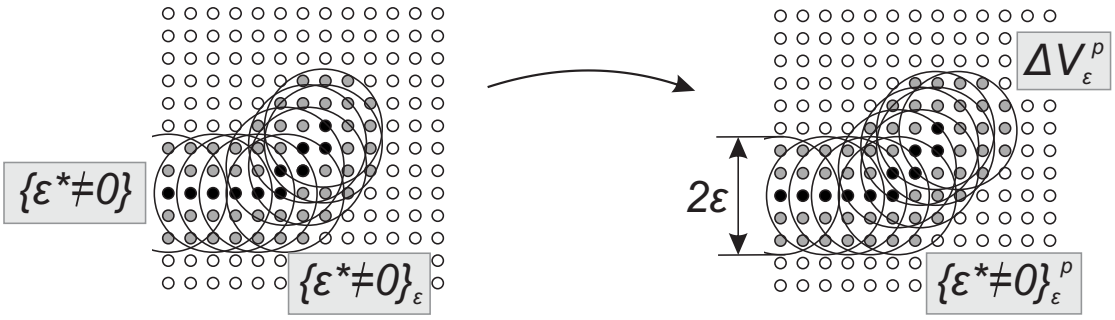

Figure 4.4.: Visualization of the material point eigenerosion approach (adapted from [Pandolfi et al., 2014]). Black dots denote members of the crack set ($\{\epsilon^* \neq 0\}$), whereas gray dots belong to the ϵ-neighborhoods of failed material points ($\{\epsilon^* \neq 0\}_\epsilon$). The thickness of the ϵ-neighborhood is 2ϵ and, after crack propagation, the increment in the crack's ϵ-neighborhood is ΔV_ϵ^p.

whereby $|\{\epsilon^* \neq 0\}_\epsilon|^p$ is the ϵ-neighborhood of $\mathcal{C}$ after inclusion of V_ϵ^p. The choice of the regularization parameter ϵ must be such that its value tends to zero more slowly than the mesh size. One possibility is therefore to use a regularization parameter proportional to the minimum mesh size according to

$$\epsilon = C_1 h_{min}, \tag{4.20}$$

where $C_1 > 0$ is a constant.

4.2. Supporting microscopy and experimental calibration

The macroscopic fracture model that results from the optimal scaling analysis is solely characterized by the critical energy-release rate G_c. This parameter is well-known from Griffith's theory of linear-elastic fracture and correlates the free-surface energy of a propagating crack to the elastic energy stored in the bulk of the material. Rivlin and Thomas [1953] extended Griffith's concept to determine the tear resistance of highly stretched

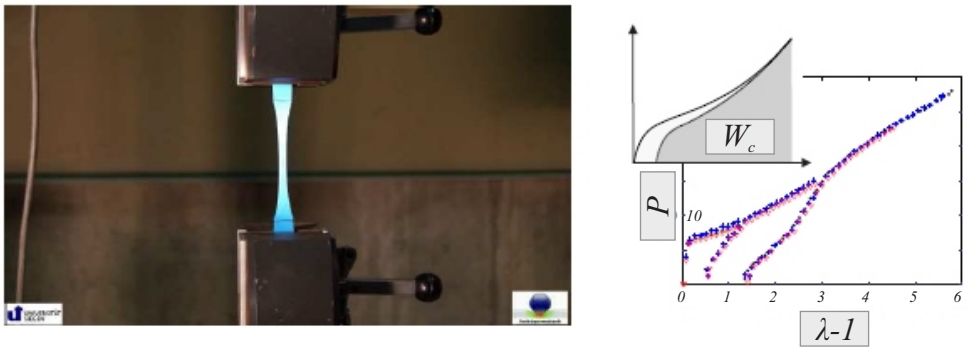

Figure 4.5.: Uniaxial tension test of polyurea 1000 with feed of 2mm/s [Reppel et al., 2012]. Left: Thin-strip specimen stretched quasistatically up to failure. Right: Determination of the elastic strain energy density by data reduction.

rubbery material. Here, the critical energy release rate follows from

$$G_c = l_c\, W(\lambda_c), \tag{4.21}$$

where l_c is the crack length and $W(\lambda)$ is the elastic-strain energy density as a function of the applied stretch λ. The specific fracture energy $W_c \equiv W(\lambda = \lambda_c)$ follows as the area under the elastic stress-strain curve from beginning until rupture at $\lambda = \lambda_c$.

Typically, the specimens used to determine G_c are dog-bone-shaped thin strips or thick-waist sheets tested in tension. To analyze crack growth in moderate but cyclic loading, these specimens are pre-cut. Moreover, the crack length in (4.21) corresponds to the increase in cut length. In a monotonous loading regime, the width of the specimen defines the maximal amount of elastic strain energy density at rupture.

In order to determine G_c for PU 1000, uniaxial tension tests using thin-strip specimens were performed by Reppel et al. [2012]. Since the tear resistance after monotonous loading was investigated, the specimens were not preconditioned against the Mullins effect. Instead, the amount of permanent set within the teared specimen was accounted for, which was determined by stepwise loading and unloading of several samples. Figure 4.5 illustrates the approach. Here, specimens were stretched to 150% and to 350%, both

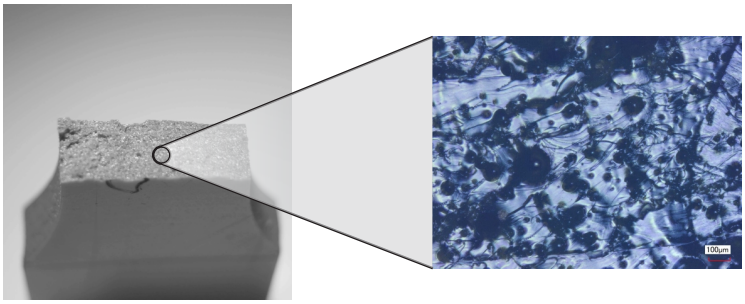

Figure 4.6.: Micrograph of the fracture surface of a polyurea specimen after failure in uniaxial tension (adapted from [Reppel et al., 2012]), whereby shaded areas represent voids.

followed by a full relaxation, and subsequently re-stretched to rupture. Based on the recorded loading-unloading data, the relative extent of material dissipation was calculated. The remaining energy density is the maximal amount of elastic strain energy upon failure, i.e., the specific fracture energy.

Finally, this data reduction procedure yielded a value of $W_c = 38.2\,\mathrm{MPa}$ for PU 1000 specimens with width $l_c = 1.15\,\mathrm{mm}$. The critical energy release rate follows from Figure 4.5 as $G_c = 44\,\mathrm{kJ/m^2}$. This value is employed in the numerical Taylor-anvil test simulations presented in Section 4. Compared to typical values for polymers (which are around $1-10\,\mathrm{kJ/m^2}$ [Alger, 1997]), the obtained value of G_c is relatively high. This may be explained by the remarkable stretchability of polyurea 1000 and also by the monotonically-loaded, not-preconditioned specimen. The close agreement between the numerical results of Section 4.4 and experimental observations thereof lend a modicum of support to the data reduction procedure just described as a means for determining the tear resistance of stretched polyurea.

Additionally, a virgin and post-mortem fractographic analysis of the failure surface reveals insight into the micromechanisms of fracture. The polyurea, in its as received state, had a porosity of about 50 voids/$\mathrm{mm^2}$ with diameters in the range of $10-30\ \mu m$, see Figure 1.3a. Upon deformation, the voids grow, fibrils rupture and a large number of new

Table 4.1.: Elastic material parameters of a Neo-Hookean solid for polyurea used in OTM-simulations of Taylor-impact experiments.

λ_0 [MPa]	133.793
μ_0 [MPa]	5.759

voids nucleate. The void multiplication is clearly evident in post-mortem fractographs of failure planes, which show considerable dimpling. Counting the density of dimples gives a porosity of 97 voids/mm^2, with some dimple diameters in excess of 200 μm, as shown in Figure 1.3b. The complex interplay between void nucleation and growth, failed fibrils and rupture is clearly evident.

4.3. Static and viscoelastic behavior of polyurea

In this section, the static and viscoelastic material behavior of polyurea is discussed. Experimental data sets from the literature (see, e.g., [Knauss and Zhao, 2007; Reppel et al., 2012]) are used to fit the different material models, and the resulting material parameters are presented. Polyurea is highly elastic and deforms in a reversible way, but as most elastomers it also shows retardation and time dependence. Thus, a rheological generalized Maxwell model [Ortiz, 2012], i.e., an entropy-elastic spring in parallel with a number of spring-dashpot elements, is suitable for material characterization.

Typical stress-strain curves of polyurea are indicative of ostensibly-elastic behavior up to elongations of the order of 700%. Consequently, the elastic branch of the material stress-strain relationship may be adapted to low-strain rate experimental data and quasistatic experiments (see, e.g., Sarva et al. [2007] and Reppel et al. [2012]). A prime example of such elastic material models is the Neo-Hookean solid, which was derived in the context of macromolecular polymer models in Section 1.2.1. In its compressible extension, the

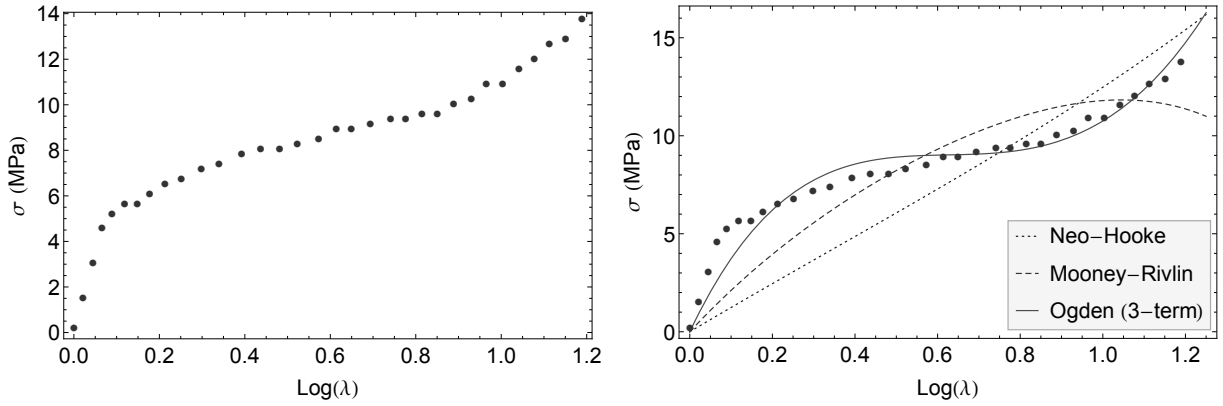

(a) (b)

Figure 4.7.: Comparison of different elastic material models shown in (b) fitted to low-strain rate experimental data of Sarva et al. [2007] at $\dot{\epsilon} = 0.0016s^{-1}$ as depicted in (a).

strain energy density of a Neo-Hookean solid takes the form

$$W_0(\mathbf{F}) = \frac{1}{2}\lambda_0 \log J^2 - \mu_0 \log J + \frac{1}{2}\mu_0 [\mathrm{tr}(\mathbf{C}) - 3], \tag{4.22}$$

where $\mathbf{C} = \mathbf{F}^T\mathbf{F}$ denotes the right Cauchy-Green tensor. The material parameters λ_0 and μ_0 may be obtained by subsequent fitting to experimental data, and are given in Table 4.1. Figure 4.7 furthermore shows a comparison of different elastic material models.

The viscous response of polyurea is commonly assumed to be isochoric, with $\bar{\mathbf{F}} = J^{-1/3}\mathbf{F}$. The dissipation potential of this particular material may be modeled by extending a Prony-series [Ortiz, 2012] to the finite-deformation range. Introducing the tensor of deviatoric logarithmic strains, $\mathbf{e} = \log\sqrt{\bar{\mathbf{C}}}$, where $\bar{\mathbf{C}} = \bar{\mathbf{F}}^T\bar{\mathbf{F}}$, the formulation of N Maxwell elements in parallel follows as

$$\phi = \sum_{\alpha=1}^{N} \mu_\alpha |\mathbf{e} - \mathbf{e}_\alpha^i|^2 \,. \tag{4.23}$$

Here, the $\mathbf{e}^i$ form the set of internal variables accounting for the N relaxation mechanisms and μ_α are the corresponding material constants. The evolution of the inelastic strains is

Table 4.2.: Moduli and relaxation times for polyurea (units are [MPa] and [s]) obtained from fitting [Knauss and Zhao, 2007].

μ_α	5.164	5.400	2.529	2.525	1.451	1.101	0.299	0.332	0.578
τ_α	1.0e-5	1.0e-4	1.0e-3	1.0e-2	1.0e-1	1.0	10.0	100.0	1000.0

assumed to be governed by linear kinetics, viz.

$$\dot{\mathbf{e}}^i_\alpha = \frac{1}{\tau_\alpha}\left(\mathbf{e} - \mathbf{e}^i_\alpha\right), \tag{4.24}$$

where τ_α are viscoelastic relaxation times. This model can be cast into an incremental variational framework by recourse to variational constitutive updates [Ortiz and Stainier, 1999]. Consequently, the state of the body (i. e., the internal variables and the primary kinematic quantities) at each time increment can be obtained by minimization of a total power potential with respect to the viscous strains, $\mathbf{e}^i_\alpha$, for each relaxation mechanism, $\alpha = 1,\ldots,N$. The first Piola-Kirchhoff stress tensor then follows as the sum of elastic and viscous contributions according to

$$\mathbf{P} = \frac{\partial W}{\partial \mathbf{F}}(\mathbf{C}, \mathbf{e}^i_1, \ldots, \mathbf{e}^i_N). \tag{4.25}$$

Elastic moduli and relaxation times for polyurea have been determined by Knauss and Zhao [2007] for small strains. By setting $\mu_\alpha = E_\alpha/3$ for nearly incompressible polymeric materials, these data can be expressed in terms of the Lamé parameters. The resulting numerical values are summarized in Table 4.2. By specifying the above model to the incompressible uniaxial state and integrating the viscous strains for fixed strain rates, the model can be compared to large-deformation experiments. Figure 4.8 shows that the high strain rate data of Sarva et al. [2007] can be recovered with good accuracy in this way.

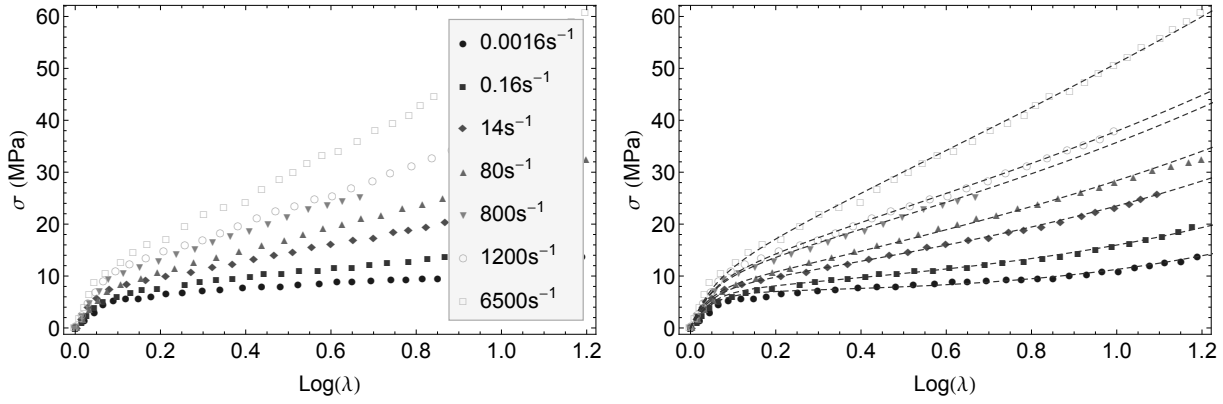

Figure 4.8.: Left: Cauchy stress σ versus true strain $\epsilon = \log \lambda$ for polyurea at different true strain rates $\dot{\epsilon}$; data collected from Roland et al. [2007], Sarva et al. [2007], Yi et al. [2006], Zhao et al. [2007], Amirkhizi et al. [2006] and Reppel et al. [2012]. Right: Results for fittings of a Prony series formulation as introduced in Section 4.3 to the experimental data set.

4.4. Taylor-anvil tests

The macroscopic fracture model that results from the optimal scaling analysis is characterized by a single parameter, namely the critical energy-release rate G_c. This simple structure greatly simplifies material characterization. By way of illustration, and in order to calibrate subsequent calculations, G_c for polyurea 1000 is estimated from the uniaxial-tension test data of Weinberg and Reppel [2013].

Another appealing aspect of the macroscopic fracture model is that it is amenable to a straightforward numerical implementation based on material-point erosion [Li et al., 2012; Pandolfi and Ortiz, 2012; Schmidt et al., 2009]. The scope of the resulting numerical model is demonstrated by means of an example of application: the Taylor-impact experiments of Mock and Drotar [2006] on polyurea 1000 specimens. These simulations additionally furnish a modicum of validation of the fidelity of the failure and fracture model.

The tests of Mock and Drotar [2006] were performed at the Research Gas Gun Facil-

Table 4.3.: Specifics of the three different Taylor-anvil test cases.

	Velocity [m/s]	Initial length [mm]	Initial diameter [mm]
Case I	245.759	25.73528	12.59205
Case II	332.047	25.60828	12.61491
Case III	424.413	25.76068	12.61745

ity at the Naval Surface Warfare Center (Dahlgren Division). Cylindrical specimens of polyurea 1000 were driven into a metal anvil at different impact speeds, cf. Table 4.3. Figure 4.9 shows a sequence of specimen snapshots during impact for an impact velocity of $v = 245$ m/s. The large deformations undergone by the specimen are evident from the figure. At sufficiently large impact velocities, the specimen is observed to petal as a result of the development of radial cracks or tears. Post-mortem examination of the specimens also reveals extensive distributed damage in the vicinity of the contact surface. The Taylor-impact experiments thus furnish a representative example of application as well as an exacting validation of the theory.

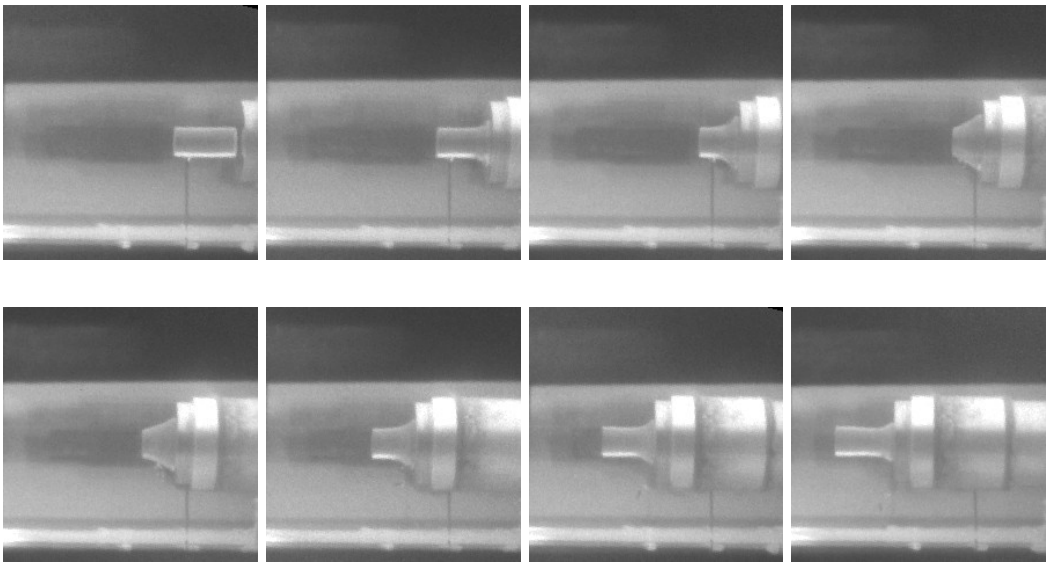

Figure 4.9.: Taylor-anvil test of polyurea 1000 rod; experiments have been performed by Mock and Drotar [2006] at NSWC. $R_0 = 6.29603$ mm, $L_0 = 25.7353$ mm, and $v = 245$ m/s.

In calculations, the viscoelastic behavior of polyurea is accounted for by means of a stan-

dard Prony series as characterized experimentally by [Knauss and Zhao, 2007; Zhao et al., 2007] and described in more detail in Section 4.3. The quasistatic response of the material is additionally described by a Neo-Hookean model. In the presence of viscoelastic and other dissipative mechanisms, the variational formulation underpinning the derivation of the optimal scaling laws, and the corresponding micro-to-macro transition formulated in Section 3, is recovered through time-discretization using variational constitutive updates [Ortiz and Stainier, 1999]. These updates effectively reduce the incremental problem to the minimization of an effective energy that accounts for both elastic energy and dissipation.

The integration of the equations of motion is carried out by means of the *Optimal Transportation Meshfree* (OTM) method [Li et al., 2010] described in Section 4.1.2. Furthermore, damage and fracture are accounted for by means of material-point eigenerosion as described in Section 4.1.2.

Figures 4.10 to 4.12 show snapshots from simulations at the three different impact speeds of Table 4.3. At the smallest impact velocity of $v = 245$ m/s, the specimen undergoes large deformations before rebounding, but no radial cracks or tears develop. By contrast, incipient radial tearing is clearly evident at the intermediate impact velocity of $v = 332$ m/s, Fig. 4.11, whereas extensive petalling is predicted at the highest impact velocity of $v = 424$ m/s, Fig. 4.12. Remarkably, the radial tears retract almost entirely upon rebound and the specimens appear outwardly intact, as observed experimentally.

Figures 4.13 to **??** depict the state of damage in the recovered specimens at the three different speeds as computed and as observed post-mortem in experiments. The experimental pictures show the recovered specimens after impact, wherein the extent and distribution of damage can be clearly discerned optically. The pictures from simulations map the final state of damage by showing the failed material points as black dots in the reference configuration.

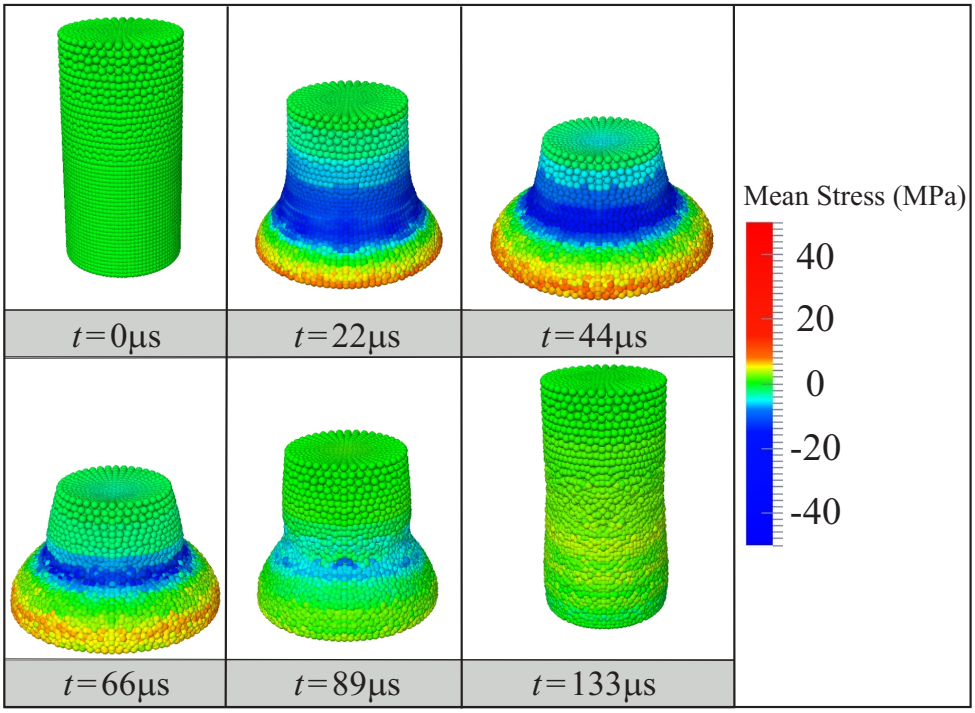

Figure 4.10.: Snapshots of the simulated deformation at v = 245 m/s impact velocity.

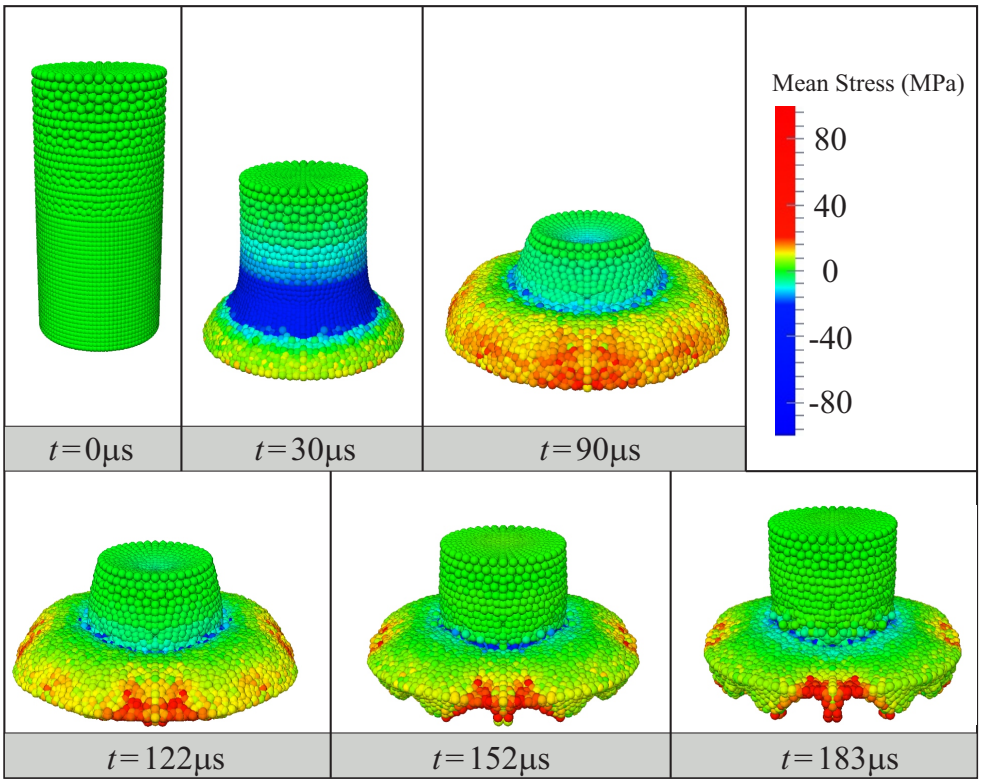

Figure 4.11.: Snapshots of the simulated deformation at v = 332 m/s impact velocity.

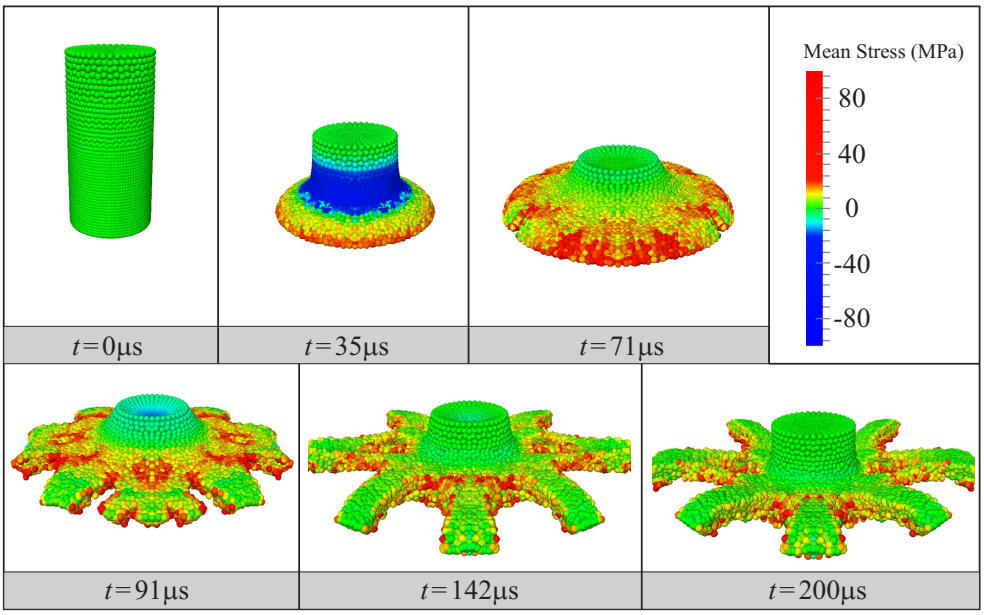

Figure 4.12.: Snapshots of the simulated deformation at $v = 424$ m/s impact velocity.

In all three comparisons, the simulations qualitatively capture the damage distribution within the specimen. At the lowest speed, Figure 4.13, the specimen is predicted to undergo limited damage and cracking in the vicinity of the impact surface, in keeping with experimental observation. At the intermediate speed, Figure **??**, the simulations predict significant distributed damage near the impact surface, in good agreement with experiments. In the simulations, the impact surface additionally undergoes incipient radial cracking, also in agreement with observation. Finally, at the largest speed, Figure **??**, both experiments and simulations reveal severe distributed damage over a large fraction of the specimen, and the impact surface splits into well-defined radial cracks or tears. The ability of a simple single-parameter (namely the critical energy release rate G_c) model to qualitatively capture both patterns of distributed damage and cracking over a range of impact velocities is remarkable.

In addition, Figure 4.14a shows the measured and computed normalized rod lengths as functions of time for all three velocities under consideration, by way of quantitative validation. By this metric, the results of the simulations match the observed trends and

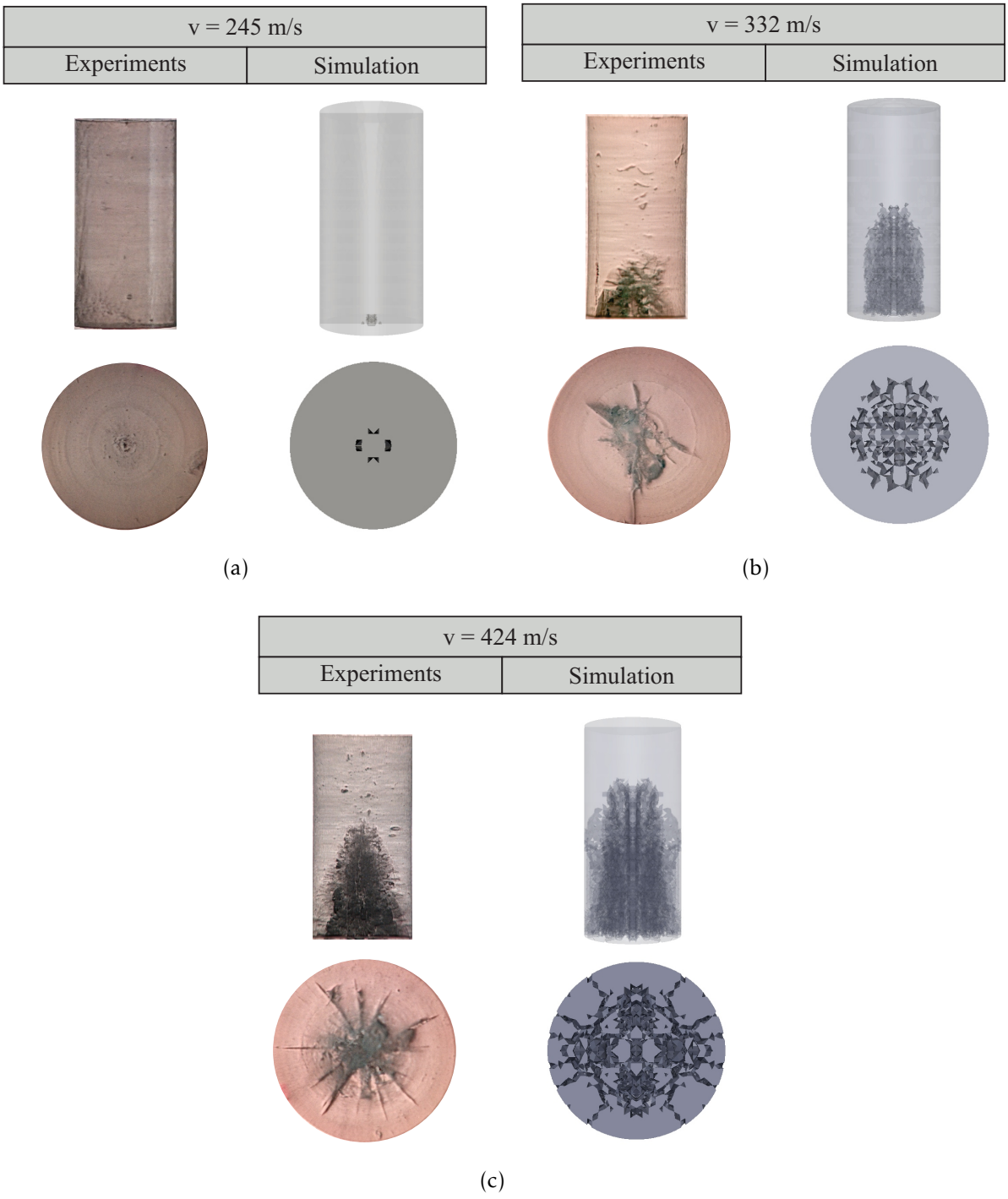

Figure 4.13.: Comparison of the recovered target after shot between experiments and simulations with impact speeds $v = 245m/s$ (a), $v = 332m/s$ (b) and $v = 424m/s$ (c).

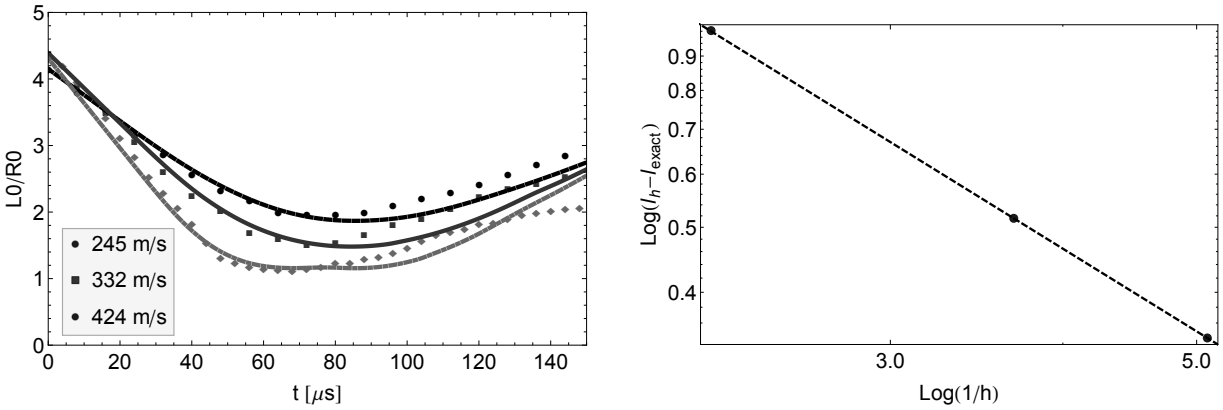

Figure 4.14.: a) Normalized specimen height versus time at impact speeds $v = 245$ m/s, $v = 332$ m/s and $v = 424$ m/s. b) Logarithmic convergence plot showing total accumulated specimen length over time for different mesh sizes.

are in fair agreement with experimental measurements.

It bears emphasis that the model employed in the simulations is remarkable for its simplicity, both with regard to the bulk behavior of the material and its fracture properties, and that no effort has been made to enhance the model in order to improve the fit to experiments.

Given the simplicity of the model, the quantitative agreement shown in Figure 4.14a may be regarded as furnishing a modicum of validation of the overall framework. For completeness, Figure 4.14b additionally shows the variation of the computed specimen length with mesh size to demonstrate convergence. A clear trend towards convergence is evidenced by the figure with a superlinear convergence rate $\alpha = 1.27$.

5. Crazing model using full derivatives and a core cut-off

The non-local regularization approach of the previous Section requires the computation of fractional derivatives, which is inconvenient for numerical implementations. Using full derivatives, in contrast, is favorable for practical purposes, yet it presents a new challenge because the energy may produce singularities in the presence of voids as those studied here. In this Section, we therefore consider a modified regularization approach based on the introduction of a core cut-off as presented in [Heyden et al., 2015].

5.1. Problem formulation

As a conventional device applied in the theory of linear-elastic dislocations, introducing a core cut-off enables the elimination of logarithmic divergence of the energy. In the present context, the core-cutoff regularization may be introduced as follows.

We begin by noting that crazing is characterized by the topology schematically shown in Fig. 5.1b, consisting of a distribution of fibrils bridging the flanks of the crack. This topology is defined by the property that circuits such as shown in Fig. 5.1b cannot be reduced to a point without exiting the material. For continuous – hence, topology preserving – deformations, the crazing topology must set in immediately following nucleation and remain invariant thenceforth. Thus, the nucleation geometry must have the structure shown in Fig. 5.1a, i. e., it must consist of a network of boreholes contained on the incipient fracture plane. Upon further deformation, the boreholes expand and eventually attain the geometry characteristic of crazing.

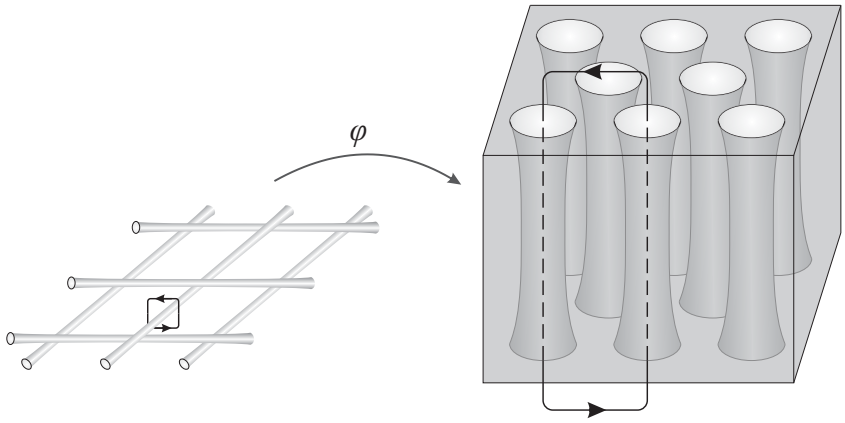

Figure 5.1.: Schematic of the topology of fibril nucleation and growth. Left: Planar network of cylindrical cavities that provide the nucleation sites for fibrils. The inscribed circuit cannot be reduced continuously to a point, which illustrates the topological transition undergone by the body as a result of nucleation. Right: Distribution of fibrils resulting from the expansion of the nucleation sites under transverse uniaxial deformation. Since the deformation after nucleation is continuous outside the boreholes, the topology of the body does not change upon deformation. In particular, the structure of irreducible circuits such as inscribed remains unchanged.

In the vicinity of one borehole, the early stages of nucleation may be approximated as the expansion of a concentric cylinder with the borehole along its axis. The resulting deformation mapping is fully determined by incompressibility condition

$$\pi\left(a^2 - r^2\right) = \pi\left(A^2 - R^2\right), \tag{5.1}$$

where A (a) is the outer radius of the undeformed (deformed) configuration, B (b) is the radius of the borehole in the undeformed (deformed) configuration, R is polar radius in the undeformed configuration and r is the corresponding polar radius in the deformed configuration. The corresponding nonzero components of the deformation gradient follow as

$$F_{RR} = \frac{R}{\sqrt{a^2 - A^2 + R^2}}, \qquad F_{TT} = 1/F_{RR}, \qquad F_{ZZ} = 1, \tag{5.2}$$

where (R, T, Z) denotes a system of cylindrical coordinates over the the undeformed configuration.

A straightforward calculation further gives the norm of the second deformation gradient as

$$|\nabla \mathbf{F}| = \sqrt{\frac{\left(a^2 - A^2\right)^2 \left(3a^4 + 6a^2\left(R^2 - A^2\right) + 3A^4 - 6A^2R^2 + 4R^4\right)}{R^4\left(a^2 - A^2 + R^2\right)^3}}. \tag{5.3}$$

Assuming p-growth, $p \geq 1$, at large deformations the nonlocal energy per unit undeformed length of the cylinder follows as

$$E_{non} \sim \int_B^A C\,|\nabla \mathbf{F}(R)|^p\, 2\pi R\, dR. \tag{5.4}$$

For $a/A \gg 1$, a straightforward asymptotic analysis gives

$$|\nabla \mathbf{F}(R)| \sim \sqrt{3}\frac{a}{R^2}, \tag{5.5}$$

which substituted into Equation (5.4) in turn gives

$$E_{non} \sim \frac{3^{p/2}\pi C}{p-1}\left(\frac{1}{B^{2(p-1)}} - \frac{1}{A^{2(p-1)}}\right) a^p, \tag{5.6}$$

if $p > 1$, and

$$E_{non} \sim 2\sqrt{3}\pi C a \log\frac{A}{B}, \tag{5.7}$$

for linear growth $p = 1$. We see that, in call cases, the energy diverges as the core-cutoff radius B tends to zero, logarithmically so in the case of linear growth of the nonlocal energy.

In order to avert this divergence and obtain finite energies, we simply assume that the nucleation boreholes have an initial radius commensurate with a characteristic length of

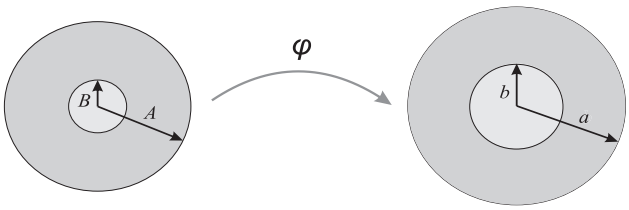

Figure 5.2.: Expansion of borehole in a concentric incompressible cylinder.

the chain distribution in the polymer network. Thus, in view of the network structure of polymers, we may think of the initial boreholes as spanning intervening space between chains and their diameter to be of the order of the mean-free path between chains.

5.2. Crazing and scaling

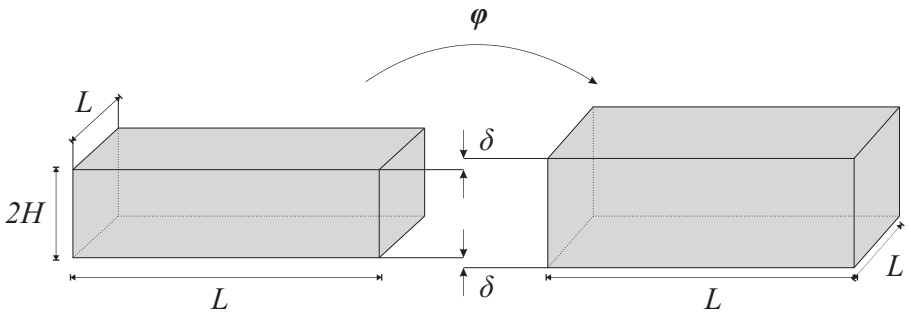

Figure 5.3.: Infinite slab of thickness $2H$ subject to prescribed opening displacements δ on its surface.

A principal aim of the present work is to ascertain such scaling laws as may be obeyed by the macroscopic fracture energy resulting from the micromechanical model just described. In order to make connection with such macroscopic fracture properties, we specifically consider periodic deformations of a slab of thickness $2H$ occupying the domain $\{|x_3| \leq H\}$ subject to prescribed opening displacements δ on its surfaces, Fig. 5.3.

We identify a periodic unit cell $\Omega = [0,L]^2 \times (-H,H)$ and describe the deformation of the slab by means of a $[0,L]$-periodic deformation mapping $\varphi : \Omega \to \mathbb{R}^3$ subject to the

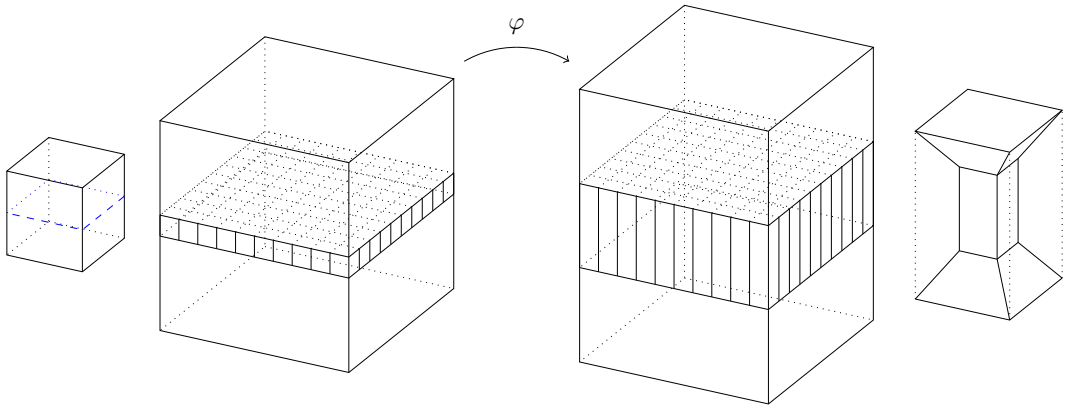

Figure 5.4.: Assumed deformation pattern describing the process of crazing. The deformation is assumed to localize to a thin layer of thickness a and, elsewhere, the slab is assumed to undergo a rigid translation through the prescribed opening displacement $\pm\delta$. The layer is then further subdivided into identical cubes of size a, each of which undergoes the deformation illustrated above. The void region arises from the equator of the cube as shown on the right.

constraint of volume conservation in Ω and to displacement boundary conditions

$$\varphi_3(x_1, x_2, -H) = -H - \delta, \tag{5.8a}$$

$$\varphi_3(x_1, x_2, H) = H + \delta, \tag{5.8b}$$

with $(x_1, x_2) \in [0, L]^2$. The aim of the analysis is to derive optimal, or matching, upper and lower bounds for the energy of the slab as a function of the parameters entering the energy.

5.2.1. Some heuristics

A deformation mapping which describes, in a simple manner, the process of crazing is shown schematically in Figures 5.3 and 5.4. The deformation is localized to the layer $(0, L)^2 \times (-a, a) \subset \Omega$ and, elsewhere, the slab undergoes a rigid translation through the prescribed opening displacement δ. The layer $(0, L)^2 \times (-a, a)$ is then subdivided into $\sim (L/a)^2$ identical cubes of size a.

The deformation is everywhere volume preserving and results in the formation of a fibril along the vertical axis of the cube by means a process of cavitation from the four boundary segments on the symmetry plane of the cube. As noted above, the process of cavitation from a line results in infinite energies in solids obeying strain-gradient elasticity. We relax this excessive rigidity by assuming availability of nucleation boreholes of a small but finite radius.

We proceed to argue heuristically the expected scaling properties of the deformation just described. For definiteness, we assume linear scaling of the nonlocal energy. As noted in Section 2, the local part of the energy density saturates to a constant W_∞ when all chains in the polymer network are stretched to failure. In this state, the local energy of a cube scales as

$$E_{\text{loc}} \sim W_\infty a^3. \tag{5.9}$$

Suppose, in addition, that for large deformations the non-local energy density behaves as $W_\infty \ell |\nabla \mathbf{F}|$, where ℓ is a microstructural length scale. As noted in the foregoing, to leading order the energy is dominated by a logarithmic divergence at the core of the nucleation boreholes. Under these conditions, we have

$$E_{non} \sim W_\infty a \ell \delta \log \frac{a}{b}, \tag{5.10}$$

where, here and subsequently, b denotes the core-cutoff radius. The total energy of a cube therefore goes as

$$E = E_{loc} + E_{non} \sim W_\infty a^3 + W_\infty a \ell \delta \log \frac{a}{b}. \tag{5.11}$$

Next, we optimize the size of the cubes. To this end, we note that energy per unit area of slab, or fracture energy, is given by $G = E/a^2$. Minimizing this fracture energy with

respect to the cube size gives

$$\frac{\partial G}{\partial a} = \frac{\partial}{\partial a}\frac{E}{a^2} = W_\infty - W_\infty \frac{\ell\delta}{a^2}\log\frac{a}{b} + W_\infty\frac{\ell\delta}{a^2} = 0. \tag{5.12}$$

After simplification, we obtain the condition

$$\frac{a^2}{\ell\delta} = \log\frac{a}{b} - 1, \tag{5.13}$$

whence we obtain the optimal cell size $a^*(\delta/b, \ell/b)$. For large δ, the optimality condition simplifies to

$$a^* \sim \ell^{1/2}\delta^{1/2}\left(\log\frac{a^*}{b}\right)^{1/2} \sim \ell^{1/2}\delta^{1/2}\left(\log\frac{\ell\delta}{b^2}\right)^{1/2} \tag{5.14}$$

and the fracture energy to

$$G \sim W_\infty \ell^{1/2}\delta^{1/2}\left(\log\frac{\ell\delta}{b^2}\right)^{1/2}, \tag{5.15}$$

which to leading order is proportional to the square root of the opening displacement δ.

The specific fracture energy of the material follows from (5.15) by additionally assuming that the fibrils break at a critical opening displacement δ_c, with the result

$$G_c \sim W_\infty \ell^{1/2}\delta_c^{1/2}\left(\log\frac{\ell\delta_c}{b^2}\right)^{1/2}. \tag{5.16}$$

The structure of this specific fracture energy is noteworthy. Thus, G_c is proportional to W_∞, the saturation value of the local energy density at failure. The parameter W_∞ provides a measure of the strength of the material and, thus, it is reasonable to expect that the specific fracture energy be in proportion to W_∞.

We also observe that G_c is to leading order in direct proportion to the geometric mean of

the intrinsic length ℓ and the critical opening displacement δ_c. The core cutoff radius b enters only through the logarithmic term. These dependences are also expected since ℓ sets the scale for the non-local regularization, δ_c provides a measure of the strength of the fibrils, and b sets the scale of the logarithmic energy barrier for nucleation.

It is also instructive to compare with the fractional derivative regularization proposed by Heyden et al. [2014]. In that model the boreholes were absent, $b = 0$, but the term $\int \ell|\nabla \mathbf{F}|$ was replaced by the softer term $\int \ell^\sigma|\nabla^\sigma \mathbf{F}|$, with σ smaller than 1. Therefore the $b \to 0$ limit of the present model should correspond to the $\sigma \to 1$ limit of the fractional-derivative model.

Indeed, Conti et al. [2014] derived a scaling of the energy proportional to $\ell^{\sigma/(1+\sigma)}\delta^{1/(1+\sigma)}$, which reduces to the present scaling $\ell^{1/2}\delta^{1/2}$ as $\sigma \to 1$. The prefactor arising from the fibril construction was however proportional to $1/(1-\sigma)$ and diverges in the limit, much as the logarithmic term in the present model diverges as $b \to 0$.

5.2.2. Local constitutive damage model

In order to facilitate computations, cubature formulas as derived in [Cools, 2003] have been used for an approximation of the surface integral in Equations (2.18) and (2.19). A total of 14 cubature points was chosen in computations, whereby marginally modifying their respective location on the unit sphere enables the attainment of a fully damaged state in the limit of large deformations.

Figure 5.5 illustrates that under uniaxial loading conditions, cubature points aligned with the principal axes of loading result in a small subset of cubature points whose fiber orientation will never lead to complete damage due to the chosen number of finite cubature points. The set of cubature points is therefore rotated by an intrinsic rotation (see Figure 5.6).

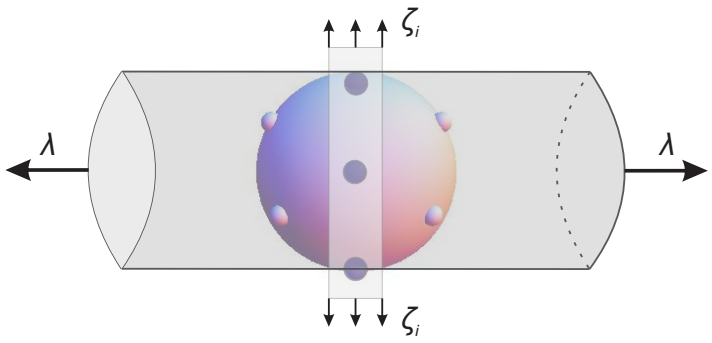

Figure 5.5.: Subset of cubature points on the unit sphere for which fiber orientation ζ_i under uniaxial loading in the direction of λ lies in a purely compressive zone (and hence will not fail in the limit of large deformations).

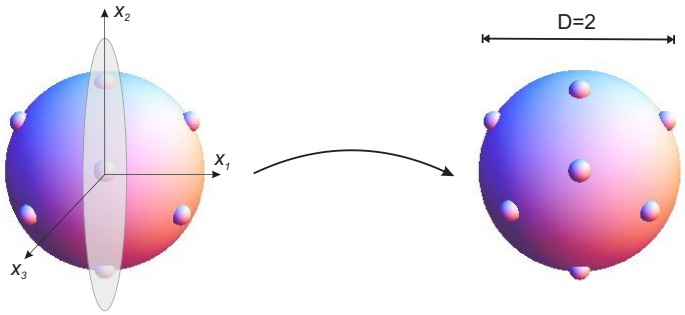

Figure 5.6.: Cubature points on the unit sphere before (left) and after rotation (right).

The local strain energy density contribution then follows as

$$\begin{aligned} W(\mathbf{F}) = &\frac{4\pi b^2}{3k_B T l^2 n} f(J, I_2) \\ &+ \sum_{i=1}^{n} w_i D\left(\sqrt{Q_I^i C_{IJ} Q_J^i}\right) Q_I^i C_{IJ} Q_J^i \\ &+ \frac{E_b}{k_B T} \sum_{i=1}^{n} w_i \left[1 - D\left(\sqrt{Q_I^i C_{IJ} Q_J^i}\right)\right], \end{aligned} \tag{5.17}$$

whereby $\mathbf{Q}^i$ and w_i are quadrature point locations and weights, respectively. Furthermore, volumetric energy contributions are modeled using a Mooney-Rivlin material ac-

cording to

$$f(J,I_2) = f(I_2) + f(J)$$
$$= \frac{\mu}{2}\left(\tilde{I_2} - 3\right)\sum_{i=1}^{n} w_i D\left(\sqrt{Q_I^i C_{IJ} Q_J^i}\right) + \frac{\kappa}{2}(J-1)^2, \tag{5.18}$$

with a modified second invariant $\tilde{I_2} = \frac{1}{2}\left[(\mathrm{tr}\,(\mathbf{C}_{dev}))^2 - \mathrm{tr}\,(\mathbf{C}_{dev}\mathbf{C}_{dev})\right]$ (where $\mathbf{C}_{dev} = \mathbf{F}_{dev}^T\mathbf{F}_{dev}$ and $\mathbf{F}_{dev} = \mathbf{F}J^{-1/3}$).

It should be noted that the damage distribution function $D(\lambda(\mathbf{Q}_i))$ does not enter volumetric contributions $f(J) = \frac{\kappa}{2}(J-1)^2$ in order to not weaken incompressibility. Introducing constants E_f and c as

$$E_f = \frac{E_b}{k_B T} \quad \text{and} \quad c = \frac{4\pi b^2}{3k_B T l^2 n} \tag{5.19}$$

leads to first Piola-Kirchhoff stresses of the form

$$\frac{\partial W}{\partial \mathbf{F}} = \sum_{i=1}^{n} w_i \mathbf{F}\mathbf{Q}^i \otimes \mathbf{Q}^i \left[2D(\lambda^i) + \frac{1}{\lambda^i}\mathbf{Q}^i\mathbf{C}\mathbf{Q}^i - E_f\frac{1}{\lambda^i}\right]$$
$$+ \kappa(J-1)J\mathbf{F}^{-T} + \frac{\partial f(I_2)}{\partial \mathbf{F}} \quad \text{with} \tag{5.20}$$

$$\frac{\partial f(I_2)}{\partial \mathbf{F}} = \sum_i w_i \frac{\mu}{2}\left[\frac{1}{\lambda^i}(\tilde{I_2} - 3)\mathbf{F}\mathbf{Q}^i \otimes \mathbf{Q}^i\right. \tag{5.21}$$
$$+ D(\lambda^i)\left(-\frac{2}{3}J^{-4/3}\mathbf{F}^{-T}\mathrm{tr}(\mathbf{C})^2 + 2J^{-4/3}\mathrm{tr}(\mathbf{C})\mathbf{F}\right. \tag{5.22}$$
$$\left.\left. + \frac{2}{3}J^{-4/3}\mathrm{tr}(\mathbf{C}\mathbf{C})\mathbf{F}^{-T} - 2J^{-4/3}\mathbf{F}\right)\right]. \tag{5.23}$$

from where it can be seen that the material is not stress-free in its reference configuration, which may be associated with eigenstrains of the polymer chains.

5.2.3. Numerical non-local regularization model

For an energy functional of the general form

$$I = \int_{\Omega} W(\mathbf{F}, \nabla\mathbf{F})\, dV - \int_{\partial\Omega_t} \mathbf{T} \cdot \delta\boldsymbol{\varphi}\, dS \tag{5.24}$$

with tractions $\mathbf{T}$ and deformation mapping $\boldsymbol{\varphi}$, taking first variations and enforcing stationarity gives

$$\begin{aligned}\delta I = &\int_{\partial\Omega_t} \Big[\Big(P_{iJ} - \eta_{ikJ,k}\Big) N_J - T_i\Big] \delta\varphi_i\, dS \\ &+ \int_{\partial\Omega_t} \eta_{iJk} N_J \delta\varphi_{i,k}\, dS \\ &- \int_{\Omega} \Big(P_{iJ} - \eta_{ikJ,k}\Big)_{,J} \delta\varphi_i\, dV = 0.\end{aligned} \tag{5.25}$$

Here, $P_{iJ} = \frac{\partial W}{\partial F_{iJ}}$, $\eta_{iJk} = \frac{\partial W}{\partial F_{iJ,k}}$ and $\delta\boldsymbol{\varphi} = 0$ on $\partial\Omega_u$ are used. While the first and last terms invite to the definition of an effective stress tensor in the presence of higher-gradient terms, the second (surface) term is numerically challenging. The numerical implementation of such gradient theories requires not only higher-order elements that accurately interpolate the higher gradients required in the model.

In addition, the surface term (which accounts for tractions conjugate to the second-order deformation gradient) necessitates the implementation of special boundary elements. In order to circumvent these and related difficulties, we introduce the following approximation.

Non-local energy contributions, as introduced in the optimal scaling laws in Equation (3.2), are in the following specified via a jump regularization model. The model takes into account interface element contributions depending on the jump in deformation across interfaces, and thus approximates gradient regularization terms in a finite element setting with linear elements.

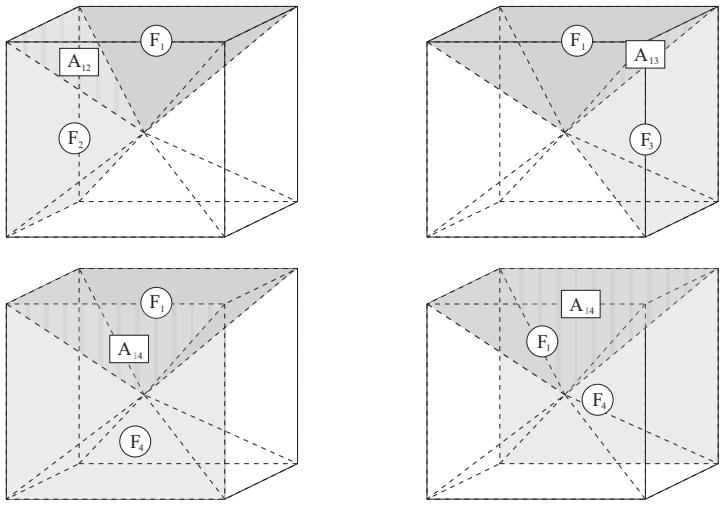

Figure 5.7.: Examples of different sets of interface energy contributions between tetrahedral element 1 and its neighbors.

As a starting example, consider a one-dimensional chain of n nodes and $n-1$ simplicial elements that therefore have constant deformation gradients $F_i = (\varphi_{i+1} - \varphi_i)/\Delta x$ $(i = 1, \ldots, n)$ with Δx being the (constant) element length. As an approximation to the gradient energy, let us introduce

$$W_{\text{interface}} = k \sum_{i=1}^{n} |\Delta F_i|^a \, A_i \tag{5.26}$$

where A_i denotes the cross-sectional area of each element and $\Delta F_i = F_{i+1} - F_i$ is the jump in the displacement gradient across an element interface. In the limit of an infinitely-fine discretization, we thus see that for $a = 1$,

$$\begin{aligned} \lim_{n\to\infty} W_{\text{interface}} &= \lim_{n\to\infty} k \sum_{i=1}^{n} |\Delta F_i| \, A_i = k \lim_{n\to\infty} \sum_{i=1}^{n} \left| \frac{F_{i+1} - F_i}{\Delta x} \right| \Delta x A_i \\ &= \int_L k |\nabla F| \, dx. \end{aligned} \tag{5.27}$$

Note that if $a \neq 1$, energy (5.26) should be modified as follows in order to maintain the

correct limit:

$$W_{\text{interface}} = k \sum_{i=1}^{n} \frac{|\Delta F_i|^a}{(\Delta x)^{a-1}} A_i. \tag{5.28}$$

In a three-dimensional setting, the interfacial energy contributions introduced above can be defined as

$$W_{\text{interface}}(\Delta \mathbf{F}) = A_f \, W_{\text{jump}}(\Delta \mathbf{F}), \tag{5.29}$$

with interface area A_f (see Figure 5.7 for reference) and jump regularization model

$$W_{\text{jump}}(\Delta \mathbf{F}) = k \, \|\Delta \mathbf{F}\|^a. \tag{5.30}$$

Here, k serves as a non-local stiffness parameter, whereas a is a measure of growth. For polymers undergoing crazing mechanisms, linear growth of the non-local energy with respect fractional derivatives of the deformation gradient is expected. Our investigation therefore focuses on the limiting case $a = 1$ (for implications on numerical stability with regard to the cusp-like regularization energies, please refer to Section 5.2.4).

5.2.4. Simulation of craze formation

In this section, we aim to verify numerically the preceding heuristic scaling relations for crazing. To this end, we employ a finite-element discretization of the boundary value problem defined in Section 5.2. By periodicity, we restrict the analysis to one in-plane periodic unit cell of the slab. In addition, we exploit symmetry in order to further restrict the analysis to one eighth of the unit cell.

A schematic of the domain of analysis and the tetrahedral 8,766-element mesh used in calculations is shown in Fig. 5.8. We note that the computational domain includes a small

groove along the perimeter of the unit cell simulating the initial nucleation borehole.

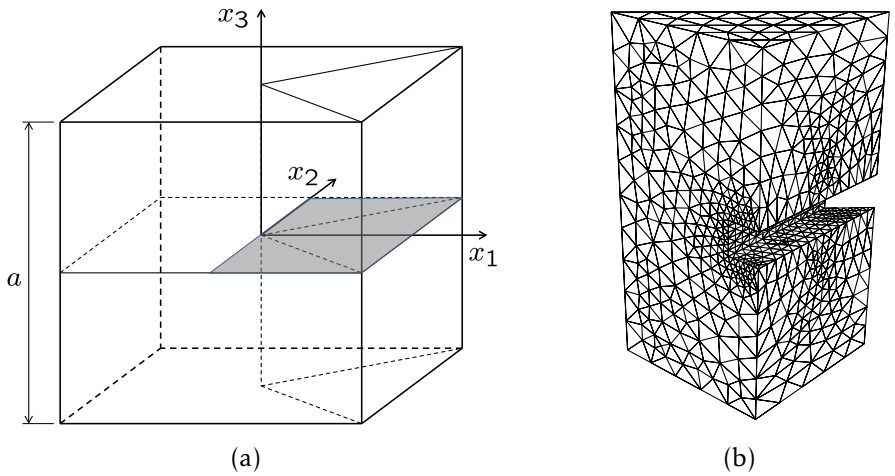

Figure 5.8.: a) Schematic of the domain of analysis spanning one quarter of the cubic periodic unit cell. b) Initial tetrahedral 8,766-element mesh used in calculations.

We enforce the incompressibility constraint by means of a penalty method consisting of adding to the unconstrained local energy a very high bulk or volumetric energy. In order to avoid locking, we employ quadratic interpolation in the discretization of the local energy. By contrast, we employ linear interpolation in the discretization of the nonlocal energy. By virtue of this choice, the second deformation gradient $\nabla\mathbf{F}$ vanishes in the interior of the elements and is concentrated on the interfaces between adjacent elements.

The energy contributed by each such interface is then evaluated as $W_\infty \ell A \left|\|\mathbf{F}\|\right|$, where A is the area of the interface, and $\|\mathbf{F}\|$ is the jump of the deformation gradient across the interface. The corresponding equilibrium problem is solved by means of an iterative nonlinear conjugate-gradient solver.

A sequence of equilibrium configurations under increasing prescribed opening displacement is shown in Figure 5.9. As may be seen from the figure, the initial borehole expands greatly upon deformation, resulting in the formation of an elongated fibril. The remainder of the cell remains relatively undeformed. The figure also shows the volumetric deformation $\det(\mathbf{F})$. We observe, by way of verification, that the volumetric deformation

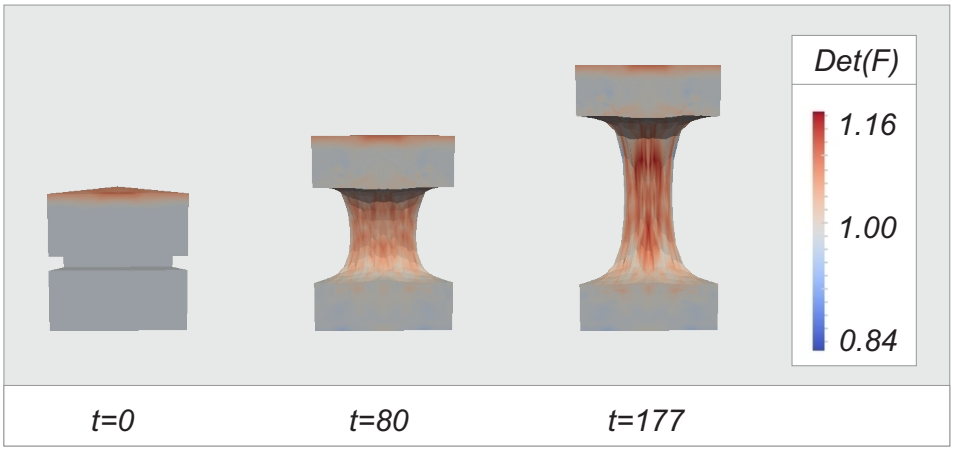

Figure 5.9.: Sequence of equilibrium configurations under increasing prescribed opening displacement. Superimposed on the figure are level contours of volumetric deformation det(**F**).

remains ostensibly close to 1 over most of the domain, with the exception of small concentrated regions where the material undergoes modest volumetric deformations.

With a view to verifying the heuristic scaling relations (5.9) and (5.10), Figs. 5.10a and 5.10b show the dependence of the local, normalized by $W_\infty a^3$, and the nonlocal energy, normalized by $W_\infty a^2 \ell$, respectively, as a function of the normalized opening displacement δ/a. The local energy thus normalized increases monotonically with the normalized opening displacement and exhibits a clear trend towards saturation at a maximum energy of value $W_\infty a^3$, in agreement with (5.9), Fig. 5.10a.

In addition, the normalized nonlocal energy exhibits an ostensibly linear dependence on the normalized opening displacement, in agreement with (5.10), Fig. 5.10b. Finally, Fig. 5.11 depicts the logarithmic dependence of the normalized nonlocal energy $E_{non}/W_\infty a^2 \ell$ on the normalized core-cutoff radius b/a for fixed δ and a and $\delta \gg a$. We note that, for each value of the core-cutoff radius b, the energy is converged with respect to the mesh size. The linear dependency of the normalized nonlocal energy on the normalized core-cutoff is clearly evident from the figure.

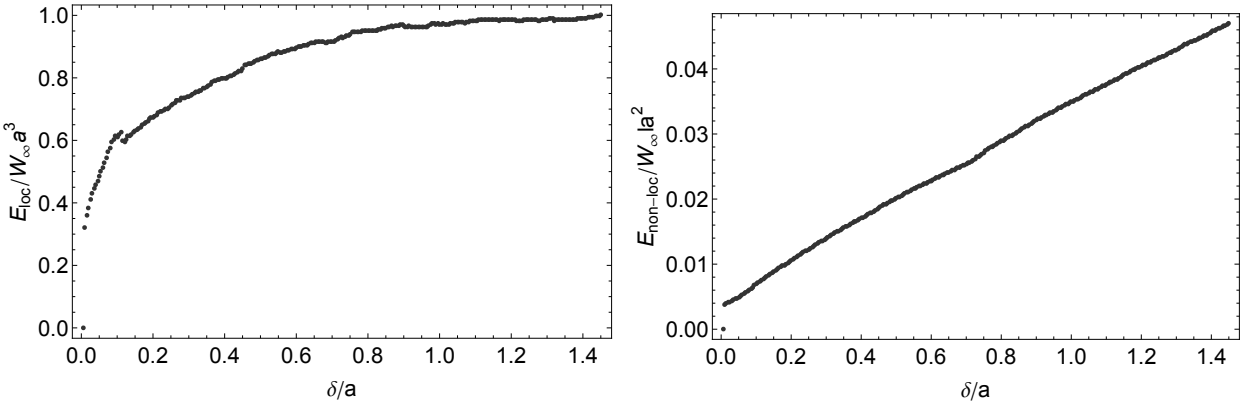

Figure 5.10.: a) Normalized local energy $W_{\text{loc}}/W_\infty a^3$ *vs.* normalized opening displacement δ/a. b) Normalized nonlocal energy $W_{\text{non}}/W_\infty a^2\ell$ *vs.* normalized opening displacement δ/a.

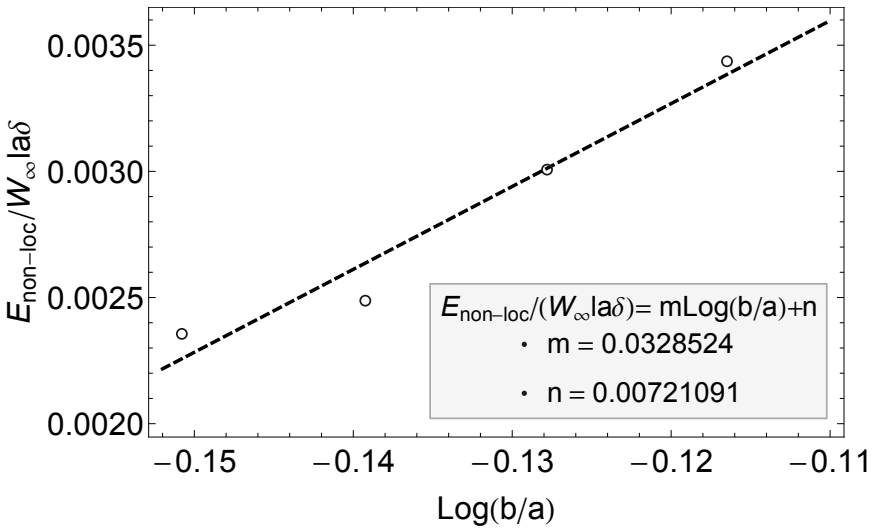

Figure 5.11.: Dependence of the normalized nonlocal energy $E_{non}/W_\infty a^2\ell$ on the normalized core cutoff radius b/a for fixed δ and a and $\delta \gg a$.

We may thus conclude that the heuristic scaling relations (5.9) and (5.10) are indeed born out by the finite-element calculations. By extension, the finite-element calculations thus lend support to the scaling of the fracture energy (5.15) and the critical energy-release rate (5.16).

6. Concluding remarks and future work

In this work, a simple one-parameter macroscopic model of distributed damage and fracture of polymers was derived. A first underlying assumption is given by the fact that the material behavior has two components, local and nonlocal. The local component characterizes the behavior of large material samples deforming uniformly, and it represents the configurational statistics of a polymeric chain network in the thermodynamic limit. In order to account for damage, the classical network theory was extended by assuming that the chain bonds have a finite strength. It was shown that, for large deformations, the corresponding deformation-theoretical free energy has zero growth, i. e., it is bounded above and below by a constant. In polymers undergoing fracture, it was assumed that this inherently unstable behavior is held in check by a second fundamental property, viz. the fractional strain-gradient elasticity. A further assumption is that the non-local component of the material behavior is characterized by fractional strain-gradient elasticity with linear growth in the strain gradient. This latter growth assumption allows for deformation jumps across sharp interfaces. Under these conditions, it was shown that fracture emerges as the net result of two competing effects: localization of deformation to failure planes promoted by the zero-growth of the local energy, and the stabilizing effect of fractional strain-gradient elasticity. We specifically derive optimal scaling laws for the macroscopic fracture energy in the form of matching upper and lower bounds. The macroscopic fracture model that results from the optimal scaling analysis is characterized by a single parameter, namely the critical energy-release rate. Conveniently, such a model is amenable to a straightforward numerical implementation by recourse to material-point eigenerosion, an averaged material-point erosion scheme that is known to

converge in the limit of zero mesh size. The range and fidelity of the damage and fracture criterion formulated in the foregoing was demonstrated by means of an example of application: Taylor-impact experiments of Mock and Drotar [2006] on polyurea specimens. Remarkably, despite its simplicity, the model captures qualitatively both patterns of distributed damage and cracking or tearing over the experimental range of impact velocities. The simulations are also in fair agreement with quantitative metrics such as the specimen length, and exhibit robust convergence with respect to mesh size.

The essential role of the intrinsic length ℓ in determining the optimal scaling behavior is particularly noteworthy. Thus, if $\ell = 0$, i. e., if the material is local, then it can be seen from (3.31) that the energy is bounded above by a bound that is linear in a, the fibril spacing. Evidently, the least upper bound is then zero, and is attained for $a = 0$, in agreement with (3.30), i. e., the energy relaxes to zero as a result of localization of deformations to a negligibly thin band. Thus, in the absence of an internal length scale the fracture energy degenerates to zero, as expected from the sublinear growth of the energy, and the solid can fracture spontaneously at no energy cost. This unstable and pathological behavior of the local energy is stabilized by the non-local energy. Indeed, the lower bound (3.32) shows that, with $\ell > 0$, fracture indeed requires a well-defined energy per unit area, or specific fracture energy. The antagonistic roles of sublinear energy growth, characteristic of polymers undergoing damage, and fractional strain-gradient elasticity in shaping the effective fracture properties of the material are remarkable.

Furthermore, a different cazing model using full derivatives of the deformation gradient and a core cut-off was presented. By means of the simple example of the expansion of a hollow cylinder in an incompressible material, it was shown that strain-gradient elasticity regularization is feasible provided that a core of a small but finite radius is assumed along the nucleation sites of the fibrils. Based on heuristic arguments, scaling relations for the local and nonlocal energies attendant to crazing were derived, as well as for the specific fracture energy thereof. Finally, finite-element calculations were presented that bear out

the heuristic scaling relations, whereby numerical implementation was achieved via a jump regularization model taking into account the jumps in deformation gradients across element interfaces. By means of uniaxial tensile simulations, it was shown how the non-local regularization model stabilizes the effect of localization to failure planes. Moreover, based on a simulation of craze formation, scaling properties of both local- and nonlocal energy contributions were verified.

A main value of the theory and the scaling analysis presented here resides in the conceptual framework that they set forth as regards the dependence of the macroscopic fracture properties of polymers on micromechanical parameters. Thus, we find that the critical energy-release rate G_c is in direct proportion to the saturation local energy density W_∞, the square root of the intrinsic length ℓ of strain-gradient elasticity and to the square root of the critical opening displacement δ_c for fibril failure, and it diverges logarithmically if the core cut-off radius b tends to zero. These dependences stand to reason since W_∞ measures the extent of energy dissipation attendant to damage, ℓ sets the scale for the non-local regularization, δ_c provides a measure of the ultimate strength of the fibrils, and b sets the scale of the logarithmic energy barrier for nucleation. Thus, the scaling laws supply a valuable link between micromechanical properties and macroscopic fracture properties of polymers. In particular, they reveal insight into the relative roles that surface energy, chain elasticity, and damage play as contributors to the specific fracture energy of polymers.

The experimental validation presented here suggests that a very simple model of bulk behavior and fracture suffices to characterize qualitatively, and to a fair quantitative degree, complex aspects of the dynamic behavior and failure of polymers, including large deformations, patterns of distributed damage, and fracture patterns. It should be remarked that the preponderance of fracture mechanics pertains to materials that undergo small overall deformations, be they elastic or plastic. Thus, the ability of the model to characterize fracture in solids undergoing exceedingly large deformations, including the

retraction of cracks upon unloading, is remarkable. The ability of tensile tests to supply estimates of the critical energy-release rate, also in the context of very large deformations, is also noteworthy. While its qualitative predictiveness and micromechanical foundations lend strong support to the overall modeling framework, further modeling enhancements may be desirable with a view to improving its quantitative fidelity.

In order to further elucidate desirable properties of elastomeric polymers, e.g., the high-pressure strength of polyurea, future work will include investigations below the scale of the continuum level. Hereby, for example a maximum-entropy approach could be used in a molecular dynamics framework. Its capability for the study of the long-term macroscopic behavior of complex multi-species systems mediated by slow, coupled, thermal-mechanical-chemical processes at atomistic scales enables the simulation of isentropic deformations of polymers at high pressures. Hereby, the max-ent approach will enable consideration of a much broader range of strain rates, from quasistatic to high-strain behavior, and temperatures, including isentropic temperature excursions, entropic effects and dissipation due to heat conduction at the nanoscale, than currently accessible to conventional molecular dynamics. These simulations could elucidate a number of fundamental aspects of the pressure-dependence of strength in polymers, including the role of free volume, dynamic atomic bond formation and breaking, local thermal relaxation, and others. Furthermore, the simulations represent a powerful tool for developing advanced constitutive models for use in computational mechanics codes.

Future work in the field of mathematical analysis lies in the derivation of a full model of fracture, which goes beyond the methods of optimal scaling presented in this thesis. As described in Section 3, the current analysis focuses on a specific example of deformation, viz., a slab divided into unit cells under opening displacements. A further development would be the description of fracture under general loading conditions (e.g., mode I/II loading, to name prime examples of loading conditions in fracture mechanics). Generalizing the analysis from specific cases to arbitrary loading conditions would thereby, in

the mathematical description, correspond to the derivation of a full Γ-limit.

With regard to the area of constitutive modeling, enhancements of the current material model for polyurea may be achieved by including the material's temperature dependence as well as a consideration of more elaborate chain models for the polymer's free energy. However, from the standpoint of fracture mechanics, the exploration of different chain models is expected to merely influence optimal scaling constants.

Finally, future directions in the area of numerical modeling include the implementation of fractional strain-gradient elasticity models based on mathematical representations of fractional norms. Such implementations would open the field to numerical calibrations of the optimal scaling constants analytically derived in Section 3.

A. Preliminaries

In this appendix, the basics of tensor algebra and analysis as well as the fundamentals of continuum mechanics are reviewed. This provides a brief overview of the mathematical and physical framework on which this thesis is based. For more details, the reader is refered to, e.g., [Flügge, 1972] and [Holzapfel, 2000].

A.1. Vector and tensor fundamentals

A.1.1. Basis representation and summation convention

In this thesis, vector and tensor quantities are denoted by bold symbols, where lowercase letters are used for the former and uppercase letters are used for the latter. Furthermore, a restriction to an orthonormal and time-invariant basis in the three-dimensional Euclidean vector space $\mathbb{R}^3$, described by a *Cartesian* coordinate system, will be employed for simplicity. The collection of basis vectors

$$\mathcal{B} = \{\mathbf{G}_1, \mathbf{G}_2, \mathbf{G}_3\} \tag{A.1}$$

hence enables the representation of a vector $\mathbf{v}$ with components v_i in three dimensions as

$$\mathbf{v} = \sum_{i=1}^{3} v_i \mathbf{G}_i = v_i \mathbf{G}_i. \tag{A.2}$$

Throughout this thesis, Einstein's summation convention is assumed [Flügge, 1972], stating that repeated indices that appear twice in a term are to be summed (where the upper summation bound is set by the number of dimensions).

These repeated indices (called dummy indices) are to be distinguished from free indices, which only appear once in a single term and whose total number determines the order of a tensor. A term containing no free index denotes a scalar, whereas one and n free indices represent vectors and tensors of order n, respectively.

A.1.2. Vector and tensor operations

The *Kronecker delta*, defined by

$$\delta_{ij} = \mathbf{G}_i \cdot \mathbf{G}_j = \begin{cases} 1, & \text{if } i = j \\ 0, & \text{otherwise,} \end{cases} \tag{A.3}$$

admits the definition of the *inner product* of two vectors (also known as *scalar* product) via

$$\mathbf{u} \cdot \mathbf{v} = u_i v_j (\mathbf{G}_i \cdot \mathbf{G}_j) = u_i v_i. \tag{A.4}$$

The *outer product* of two vectors (often referred to as *tensor* or *dyadic* product) is defined by

$$(\mathbf{u} \otimes \mathbf{v})\,\mathbf{w} = \mathbf{u}\,(\mathbf{v} \cdot \mathbf{w}) \tag{A.5}$$

and results in a second-order tensor

$$\mathbf{T} = \mathbf{u} \otimes \mathbf{v} = u_i v_j \mathbf{G}_i \otimes \mathbf{G}_j = T_{ij} \mathbf{G}_i \otimes \mathbf{G}_j. \tag{A.6}$$

The action of a second-order tensor onto a vector defines a linear mapping via

$$\mathbf{T}\,\mathbf{u} = (T_{ij}\mathbf{G}_i \otimes \mathbf{G}_j)u_k\mathbf{G}_k = T_{ij}\mathbf{G}_i(\mathbf{G}_j \cdot u_k\mathbf{G}_k) = T_{ij}u_k\delta_{jk}\mathbf{G}_i = T_{ij}u_j\mathbf{G}_i. \tag{A.7}$$

Analogously, the multiplication (or composition) of two second-order tensors

$$\mathbf{ST} = (S_{ik}\mathbf{G}_i \otimes \mathbf{G}_k)(T_{lj}\mathbf{G}_l \otimes \mathbf{G}_j) = S_{ik}T_{lj}\delta_{kl}(\mathbf{G}_i \otimes \mathbf{G}_j) = S_{il}T_{lj}(\mathbf{G}_i \otimes \mathbf{G}_j) \tag{A.8}$$

defines a composition of two mappings, i. e.

$$\mathbf{STu} = \mathbf{S} \circ (\mathbf{T}\,\boldsymbol{u}). \tag{A.9}$$

By exploiting the properties of the aforementioned linear mapping, the individual components of a second-order tensor are obtained via

$$T_{ij} = \mathbf{G}_i \cdot \mathbf{T}\mathbf{G}_j. \tag{A.10}$$

Consequently, tensor components T_{ij} depend on the chosen basis, whereas tensor $\mathbf{T}$ is invariant and therefore constant under coordinate transformations.

Altogether, these rules define the most common relations between tensors $\mathbf{T}$ and $\mathbf{S}$, vectors $\mathbf{u}$ and $\mathbf{v}$, and scalar m:

distributive law	$\mathbf{T}(\mathbf{u}+\mathbf{v}) = \mathbf{T}\mathbf{u} + \mathbf{T}\mathbf{v}$,
associative law	$\mathbf{T}(m\mathbf{u}) = m(\mathbf{T}\mathbf{u})$,
associative law	$(\mathbf{TS})\mathbf{u} = \mathbf{T}(\mathbf{S}\mathbf{u})$,
distributive law	$(\mathbf{T}+\mathbf{S})\mathbf{u} = \mathbf{T}\mathbf{u} + \mathbf{S}\mathbf{u}$,
commutative law	$\mathbf{T}+\mathbf{S} = \mathbf{S}+\mathbf{T}$,
distributive law	$\mathbf{T}(\mathbf{S}+\mathbf{V}) = \mathbf{TS} + \mathbf{TV}$,
associative law	$\mathbf{T}(\mathbf{SV}) = (\mathbf{TS})\mathbf{V}$,
and in general	$\mathbf{TS} \neq \mathbf{ST}$.

The relation $\mathbf{u} \cdot \mathbf{T}\mathbf{v} = \mathbf{v}\mathbf{T}^T\mathbf{u}$ defines the *transpose* $\mathbf{T}^T$ of a tensor $\boldsymbol{T}$ with components

$$(T_{ij})^T = T_{ji} \quad \text{or} \quad (u_i v_j)^T = u_j v_i, \tag{A.11}$$

from which the following rules can be deduced:

$$\begin{aligned}(T_{ij} + S_{ij})^T &= T_{ij}^T + S_{ij}^T = T_{ji} + S_{ji},\\ (T_{ij}^T)^T &= T_{ij},\\ (T_{ij}S_{jk})^T &= T_{kj}S_{ji}.\end{aligned} \tag{A.12}$$

Symmetric and antisymmetric second-order tensors are defined by

$$\begin{aligned}T_{ij} &= T_{ji} \qquad \text{if } \mathbf{T} \text{ is symmetric}\\ T_{ij} &= -T_{ji} \qquad \text{if } \mathbf{T} \text{ is antisymmetric.}\end{aligned} \tag{A.13}$$

Furthermore, one abbreviates the symmetric and skew-symmetric parts of a tensor $\mathbf{T}$ as, respectively,

$$\begin{aligned}(\mathrm{sym}\mathbf{T})_{ij} &= \frac{1}{2}(T_{ij} + T_{ji}),\\ (\mathrm{skw}\mathbf{T})_{ij} &= \frac{1}{2}(T_{ij} - T_{ji}),\end{aligned} \tag{A.14}$$

If the linear mapping associated with tensor tensor $\mathbf{T}$ is injective, the *inverse* $\mathbf{T}^{-1}$ is introduced such that

$$\mathbf{T}^{-1}\mathbf{T} = \mathbf{T}\mathbf{T}^{-1} = \mathbf{I}, \tag{A.15}$$

so that the inverse of a composition of mappings follows as

$$(\mathbf{T}\mathbf{S})^{-1} = \mathbf{S}^{-1}\mathbf{T}^{-1}. \tag{A.16}$$

In addition, special relations hold for rotation tensors $\mathbf{R} \in SO(d)$ (i. e., tensors that belong to the special orthogonal group) since

$$\mathbf{R}\mathbf{R}^{-1} = \mathbf{R}\mathbf{R}^{T} = \mathbf{I}. \tag{A.17}$$

A special tensor quantity (which is also a tensor invariant), denoted as the *trace* of a tensor, is defined according to

$$\operatorname{tr}\mathbf{T} = T_{ii}, \tag{A.18}$$

along with the relations

$$\begin{aligned} \operatorname{tr}(\mathbf{u}\otimes\mathbf{v}) &= u_i v_j \delta_{ij} = u_i v_i = \mathbf{u}\cdot\mathbf{v}, \\ \operatorname{tr}\mathbf{T} &= \operatorname{tr}\mathbf{T}^{T} = T_{ii} \quad \text{and} \\ \operatorname{tr}(\mathbf{T}+\mathbf{S}) &= \operatorname{tr}\mathbf{T} + \operatorname{tr}\mathbf{S}. \end{aligned} \tag{A.19}$$

By recourse to the Kronecker delta defined above, the *inner product* of two second-order tensors (also known as *double contraction*) can be introduced as

$$\mathbf{T}\cdot\mathbf{S} = (T_{ij}\mathbf{G}_i\otimes\mathbf{G}_j)\cdot(S_{kl}\mathbf{G}_k\otimes\mathbf{G}_l) = T_{ij}S_{kl}(\mathbf{G}_i\cdot\mathbf{G}_k)(\mathbf{G}_j\cdot\mathbf{G}_l) = T_{ij}S_{kl}\delta_{ik}\delta_{jl} = T_{kl}S_{kl}, \tag{A.20}$$

which leads to the following relations:

$$\begin{aligned} \operatorname{tr}(\mathbf{A}^{T}\mathbf{B}) &= \operatorname{tr}(A_{ik}B_{ij}) = A_{ik}B_{ij}\delta_{kj} = A_{ij}B_{ij}, \\ (\mathbf{u}\otimes\mathbf{v})\cdot(\mathbf{w}\otimes\mathbf{z}) &= (\mathbf{u}\cdot\mathbf{w})(\mathbf{v}\cdot\mathbf{z}) = u_i w_i v_j z_j \quad \text{and} \\ (\mathbf{u}\otimes\mathbf{v})\mathbf{T}(\mathbf{w}\otimes\mathbf{z}) &= (v_k T_{kl} w_l) u_i v_j. \end{aligned} \tag{A.21}$$

As a special case, the norm of a tensor of arbitrary order (including vectors and tensors)

is defined via

$$|\mathbf{T}| = \sqrt{\mathbf{T} \cdot \mathbf{T}}, \tag{A.22}$$

which for a vector $\mathbf{v}$ yields $|\mathbf{v}| = \sqrt{v_i v_i}$, and for a second-order tensor $\mathbf{T}$ we have $|\mathbf{T}| = \sqrt{T_{ij} T_{ji}}$.

The definition of the *cross product* of two vectors (also known as *vector product*) requires the introduction of the *permutation symbol*

$$\epsilon_{ijk} = \begin{cases} 1, & \text{if } i,j,k \text{ is a cyclic (even) sequence} \\ -1, & \text{if } i,j,k \text{ is an anticyclic (odd) sequence} \\ 0, & \text{if } i,j,k \text{ is an acyclic sequence.} \end{cases} \tag{A.23}$$

The vector product is then obtained as

$$\mathbf{u} \times \mathbf{v} = u_i v_j \mathbf{G}_i \times \mathbf{G}_j = \epsilon_{ijk} u_i v_j \mathbf{G}_k, \tag{A.24}$$

for which helpful relations include

$$\begin{aligned} \epsilon_{ijk}\epsilon_{imn} &= \delta_{jm}\delta_{kn} - \delta_{jn}\delta_{km}, \\ (\mathbf{u} \times \mathbf{v})_i &= \epsilon_{ijk} u_j v_k = -\epsilon_{ikj} u_j v_k = -\epsilon_{ijk} u_k v_j = -(\mathbf{v} \otimes \mathbf{u})_i \quad \text{and} \\ (\mathbf{u} \times \mathbf{v}) \cdot \mathbf{w} &= \mathbf{u} \cdot (\mathbf{v} \otimes \mathbf{w}). \end{aligned} \tag{A.25}$$

Furthermore, the *determinant* of a second-order tensor $\mathbf{T}$ can be defined by

$$\det \mathbf{T} = \epsilon_{ijk} T_{i1} T_{j2} T_{k3} \tag{A.26}$$

with relations

$$\begin{aligned} \det \mathbf{TS} &= \det \mathbf{T} \det \mathbf{S}, \\ \det \mathbf{T}^T &= \det \mathbf{T}, \\ \det \mathbf{T}^{-1} &= \frac{1}{\det \mathbf{T}} \quad \text{and} \\ \det(\mathbf{u} \otimes \mathbf{v}) &= 0. \end{aligned} \tag{A.27}$$

A.1.3. Tensor analysis

Finally, let us review rules of *differentiation* with respect to vector and tensor quantities. To this end, the *Gateaux* derivative

$$D(\Phi)\mathbf{v} = \frac{d}{d\epsilon}\Phi(\mathbf{x} + \epsilon\mathbf{v})\Big|_{\epsilon=0} \tag{A.28}$$

is introduced as the slope of Φ at point $\mathbf{x}$ into the direction of $\mathbf{v}$. A formal definition of the *gradient* of a scalar field is then given by

$$\mathrm{grad}\Phi(\mathbf{x}) \cdot \mathbf{v} = D(\Phi)\mathbf{v}, \tag{A.29}$$

which leads to the components of the gradient

$$(\mathrm{grad}\Phi)_i = \frac{\partial \Phi(\mathbf{x})}{\partial x_i}, \tag{A.30}$$

with

$$\frac{\partial x_i}{\partial x_j} = \delta_{ij} = x_{i,j}. \tag{A.31}$$

Here and in the following, a comma in an index implies differentiation with respect to the coordinates following the comma. Generalizing the gradient to arbitrary tensors and

furthermore introducing the *divergence* and *curl* operators for arbitrary (continuously differentiable) fields, we have

$$\begin{aligned} &\operatorname{grad}(\cdot) = (\cdot)_{,i} \otimes \mathbf{G}_i, \\ &\operatorname{div}(\cdot) = (\cdot)_{,i} \cdot \mathbf{G}_i \quad \text{and} \\ &\operatorname{curl}(\cdot) = -(\cdot)_{,i} \times \mathbf{G}_i, \end{aligned} \tag{A.32}$$

(A.33)

in which $(\cdot)$ denotes tensors of any order. The *del* and *Laplace* operators are then introduced as

$$\begin{aligned} &\text{del operator:} \qquad \nabla \circ (\cdot) = \frac{\partial (\cdot)}{\partial x_i} \circ \mathbf{G}_i, \\ &\text{Laplace operator:} \qquad \Delta(\cdot) = \operatorname{div}(\operatorname{grad}(\cdot)) = (\cdot)_{,kk}. \end{aligned} \tag{A.34}$$

General tensor derivatives then follow as

$$\frac{\partial (\cdot)}{\partial \mathbf{T}} = \frac{\partial (\cdot)}{\partial T_{ij\ldots n}} \otimes \mathbf{G}_i \otimes \mathbf{G}_j \otimes \ldots \otimes \mathbf{G}_n \qquad \text{with} \qquad \frac{\partial T_{ab\ldots d}}{\partial T_{ij\ldots n}} = \delta_{ai}\delta_{bj}\ldots\delta_{dn}. \tag{A.35}$$

For second-order tensors we thus have

$$\frac{\partial A_{ii}}{\partial A_{kl}} = \delta_{jk} = \mathbf{I} = \frac{\partial \operatorname{tr} \mathbf{A}}{\partial \mathbf{A}} \tag{A.36}$$

and

$$\frac{\partial T_{ij} T_{ij}}{\partial T_{kl}} = \delta_{ik}\delta_{jl} T_{ij} + T_{ij}\delta_{ik}\delta_{jl} = 2T_{kl} \qquad \text{or} \qquad \frac{\partial \operatorname{tr}(\mathbf{T}^T \mathbf{T})}{\partial \mathbf{T}} = 2\mathbf{T}. \tag{A.37}$$

Without proof it should also be mentioned that

$$\frac{\partial \det \mathbf{T}}{\mathbf{T}} = \mathbf{T}^{-1} \det \mathbf{T} = \operatorname{cof} \mathbf{T}. \tag{A.38}$$

A.2. Review of continuum mechanics

Application of the theory of continuum mechanics rests upon the basic assumption that a body can be treated as a continuum (described by a continuous position vector $\mathbf{x}$) with material properties described by continuous functions (except at a finite number of interior surfaces). Although this theory is a simplification of the underlying discrete nature of matter, such an approximation is valid if the length scale of interest L is significantly larger that the largest scale l describing the material discreteness so that $L >> l$. In this case, a continuous body may be assumed, whose properties at a material point are understood as averages over length scales $\bar{l}$ with $l << \bar{l} << L$. Under the assumption of a continuous body with material properties defined by continuous functions, mathematical laws governing the kinematics of deformation can be derived. In the following, both cases of large (finite) and small (linearized) deformations will be considered, whereby linearized kinematics are derived as a special case of the general theory of finite kinematics. The following gives a brief summary of the governing equations of continuum mechanics; for a detailed review the reader is referred to [Ortiz, 2012].

A.2.1. Finite kinematics

A body Ω, whose state is changing from an undeformed reference configuration into its deformed configuration $\boldsymbol{\varphi}(\Omega)$, is shown in Figure A.1, whereby $\boldsymbol{\varphi}$ denotes the deformation mapping

$$\boldsymbol{\varphi} : \Omega \rightarrow \mathbb{R}^d. \tag{A.39}$$

Here and in the following, upper-/lower-case letters are used to denote quantities in the reference/deformed configuration, respectively. Material points $\mathbf{X}$ in the reference and spatial points $\mathbf{x}$ in the deformed configuration are thus connected via the mapping $\mathbf{x} =$

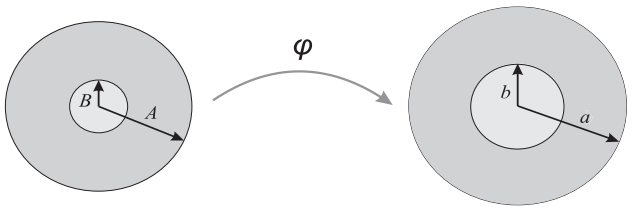

Figure A.1.: Deformation mapping $\boldsymbol{\varphi}$ between a body in the reference configuration Ω and its deformed configuration $\varphi(\Omega)$.

$\boldsymbol{\varphi}(\mathbf{X})$, which is required to be injective so that two different points in Ω do not map onto the same point in $\boldsymbol{\varphi}(\Omega)$. It is furthermore required that $\boldsymbol{\varphi}^{-1} : \boldsymbol{\varphi}(\Omega) \to \Omega$ exits.

Velocity and acceleration fields in both the material (Lagrangian) and spatial (Eulerian) framework can then be written as

$$\left.\begin{aligned} \mathbf{V}(\mathbf{X},t) &= \frac{\partial \boldsymbol{\varphi}}{\partial t}(\mathbf{X},t), \\ \mathbf{A}(\mathbf{X},t) &= \frac{\partial \mathbf{V}}{\partial t}(\mathbf{X},t), \end{aligned}\right\} \quad \text{Lagrangian framework}$$

and

$$\left.\begin{aligned} \mathbf{v}(\mathbf{x},t) &= \mathbf{V}(\boldsymbol{\varphi}^{-1}(\mathbf{x},t)) = \mathbf{V} \circ \boldsymbol{\varphi}^{-1}(\mathbf{x},t), \\ \mathbf{a}(\mathbf{x},t) &= \mathbf{A}(\boldsymbol{\varphi}^{-1}(\mathbf{x},t)) = \mathbf{A} \circ \boldsymbol{\varphi}^{-1}(\mathbf{x},t), \end{aligned}\right\} \quad \text{Eulerian framework}$$

In keeping with our previous definition, uppercase letters are used for the material and lowercase letters are used for the spatial description. It is furthermore desirable to define the material time derivative for a general time-dependent spatial function $\mathbf{f}(\cdot,t)$: $\boldsymbol{\varphi}(B,t) \to \mathbb{R}^d$, $t \in [t_1,t_2]$ as

$$\frac{D\mathbf{f}}{Dt} = \frac{\partial \mathbf{f}}{\partial t} + \frac{\partial \mathbf{f}}{\partial x_j} v_j, \tag{A.40}$$

which denotes the rate of change of $\mathbf{f}$ at a fixed $\mathbf{X}$ and thus enables the calculation of, e. g., the spatial acceleration in fluid mechanics without the introduction of a reference configuration, viz. $\mathbf{a} = D\mathbf{v}/Dt$.

Following the principle of local action, any nonlinear deformation can locally be regarded as being affine, and thus as a transformation that preserves points, straight lines, and planes. An expansion of the position vector within an infinitesimal neighborhood of $\mathbf{X}$ gives

$$dx_i = \frac{\partial \varphi_i}{\partial X_J}(\mathbf{X}) dX_J. \tag{A.41}$$

The deformation gradient $\mathbf{F}(\mathbf{X})$ [Ortiz, 2012] at $\mathbf{X}$ can now be introduced as

$$F_{iJ}(\mathbf{X}) = \frac{\partial \varphi_i}{\partial X_J}(\mathbf{X}) \tag{A.42}$$

and will subsequently be used to calculate metric changes. For changes in length, stretch ratios λ in the direction of $\mathbf{N}$ follow from

$$\lambda^2(\mathbf{N}) = \mathbf{N} \cdot \mathbf{C}\mathbf{N}, \tag{A.43}$$

where $\mathbf{C} = \mathbf{F}^T\mathbf{F}$ denotes the right Cauchy-Green deformation tensor. Furthermore, the Green-Lagrange strain tensor $\mathbf{E}$ and extensional strains $\epsilon(\mathbf{N})$ are introduced as

$$\mathbf{E} = \frac{1}{2}(\mathbf{C} - \mathbf{I}) \tag{A.44}$$

and

$$\epsilon(\mathbf{N}) = \sqrt{\mathbf{N} \cdot \mathbf{C}\mathbf{N}} - 1. \tag{A.45}$$

In addition, changes of angle, volume and area are given by, respectively,

$$\cos\varphi(\mathbf{N}, \mathbf{M}) = \frac{\mathbf{M} \cdot \mathbf{C}\mathbf{N}}{\lambda(\mathbf{N})\,\lambda(\mathbf{M})}, \quad \frac{dv}{dV} = \det \mathbf{F} = J \quad \text{and} \quad \frac{|d\mathbf{a}|}{|d\mathbf{A}|} = J\sqrt{\mathbf{N} \cdot \mathbf{C}^{-1}\mathbf{N}}, \tag{A.46}$$

with $\mathbf{N}$ being the unit normal vector on the oriented infinitesimal area segment $d\mathbf{A}$.

Rotations define a special class of linear mappings that preserve local metrics (such as lengths and angles). Rotations in $\mathbb{R}^2$ are defined by the angle of rotation, whereas rotations in $\mathbb{R}^3$ can be described by an angle as well as an axis of rotation. For the former, rotation matrices assume the form

$$\mathbf{R} = \begin{pmatrix} \cos\varphi & -\sin\varphi \\ \sin\varphi & \cos\varphi \end{pmatrix} \tag{A.47}$$

and for the latter case, rotation matrices are defined by components

$$R_{ij} = e_i e_j + (\delta_{ij} - e_i e_j)\cos\varphi + \epsilon_{ijl} e_l \sin\varphi \tag{A.48}$$

with angle of rotation

$$\cos\varphi = \frac{1}{2}(\operatorname{tr}\mathbf{R} - 1), \tag{A.49}$$

while the axis of rotation $\mathbf{e}$ has components

$$\begin{aligned} e_1 &= \frac{R_{32} - r_{23}}{2\sin\varphi}, \\ e_2 &= \frac{R_{13} - R_{31}}{2\sin\varphi} \quad \text{and} \\ e_3 &= \frac{R_{21} - R_{12}}{2\sin\varphi}. \end{aligned} \tag{A.50}$$

The deformation gradient $\mathbf{F}$ thus contains all information necessary to describe the local state of deformation. However, the existence of a corresponding deformation mapping $\boldsymbol{\varphi}$ is only guaranteed if certain compatibility conditions are satisfied. In general, any tensor field $\mathbf{F}$ is compatible over a domain U if there exists a mapping $\boldsymbol{\varphi} : U \to \mathbb{B}^3$ such that $\mathbf{F} = \operatorname{Grad}\boldsymbol{\varphi}$ and $F_{iJ} = \partial\varphi_i/\partial X_J$. Here and in the following, the capital letter of the gradient

operator (and analogously all differential operators) denotes that derivatives are taken with respect to coordinates in the reference configuration. As a necessary (pointwise) condition of compatibility, the deformation gradient must satisfy

$$\operatorname{curl} \mathbf{F} = \mathbf{0}. \tag{A.51}$$

The sufficient (domainwise) condition of compatibility requires that

$$\operatorname{curl} \mathbf{F} = \mathbf{0} \quad \text{in } U. \tag{A.52}$$

In case of discontinuities across material interfaces, the deformation gradient must satisfy compatibility in the sense of Hadamard (also known as rank-1-compatibility). The jump in $\mathbf{F}$ across an interface S (written as $\left[\!\left[F_{iJ}\right]\!\right] = a_i N_J$, whereby N_J is the unit normal onto the interface) must satisfy

$$\left[\!\left[F_{iJ}\right]\!\right] T_J = a_i N_J T_J = 0 \quad \forall \quad \mathbf{T} \in S. \tag{A.53}$$

A.2.2. Linearized kinematics

The theory of finite kinematics as outlined in A.2.1 can be simplified for cases of small deformation by linearizing the relations derived above. Most generally, material points in the deformed configuration are described by the position vector

$$\mathbf{x}(\mathbf{X}) = \mathbf{X} + \mathbf{u}(\mathbf{X}), \tag{A.54}$$

where $\mathbf{u}$ denotes the displacement field and strains are small ($\operatorname{grad}\mathbf{u} \approx \operatorname{Grad}\mathbf{u} \ll 1$). For a general field $\mathbf{G}(\boldsymbol{\varphi})$, we can introduce the linearization

$$\mathbf{G}(\boldsymbol{\varphi} + \mathbf{u}) = \mathbf{G}(\boldsymbol{\varphi}) + D\mathbf{G}(\boldsymbol{\varphi})\mathbf{u} + h.o.t. \tag{A.55}$$

and neglect all higher-order terms. The Gateaux derivative $D\mathbf{G}(\boldsymbol{\varphi})\mathbf{u}$ is defined by

$$\mathbf{G}(\boldsymbol{\varphi}+\mathbf{u}) = \mathbf{G}(\boldsymbol{\varphi}) + D\mathbf{G}(\boldsymbol{\varphi})\mathbf{u} = \mathbf{G}(\boldsymbol{\varphi}) + \frac{d}{d\epsilon}\mathbf{G}(\boldsymbol{\varphi}+\epsilon\mathbf{u})\Big|_{\epsilon=0}. \tag{A.56}$$

Application of this linearization procedure to the deformation gradient $\mathbf{F}$ about the undeformed configuration now gives

$$\mathbf{F} \approx \mathbf{I} + \operatorname{grad}\mathbf{u} \tag{A.57}$$

and the right Cauchy-Green tensor follows as

$$\mathbf{C} \approx \mathbf{I} + 2\boldsymbol{\varepsilon} = \mathbf{I} + 2(\operatorname{grad}\mathbf{u} + \operatorname{grad}\mathbf{u}^T), \tag{A.58}$$

so that linearization of the Green-Lagrange strain tensor $\mathbf{E} = \frac{1}{2}(\mathbf{C}-\mathbf{I}) \approx \boldsymbol{\varepsilon}$ yields the small-strain tensor $\boldsymbol{\varepsilon}$. For cases in which $\boldsymbol{\varepsilon} = \mathbf{0}$, linearized rotational deformations continue to be rotations (which implies that the perturbed spatial deformation gradient is skew-symmetric, i. e. $\mathbf{F} = -\mathbf{F}^T$).

Metric changes such as changes of length, angle and volume now follow as, respectively,

$$\begin{aligned} \boldsymbol{\epsilon}(\mathbf{N}) &= \mathbf{N}\cdot\boldsymbol{\epsilon}\mathbf{N}, \\ \gamma(\mathbf{N},\mathbf{M}) &= 2\mathbf{N}\cdot\boldsymbol{\epsilon}\mathbf{M} \end{aligned} \tag{A.59}$$

and

$$\frac{dv}{dV} = 1 + \operatorname{tr}\boldsymbol{\epsilon}. \tag{A.60}$$

Finally, it is desirable to find compatibility conditions analogous to $\operatorname{Curl}\mathbf{F} = \mathbf{0}$ in the linearized framework. Compatibility requires the existence of a field $\mathbf{u}$ such that $\epsilon_{ij} =$

Linearized kinematics		**Rates**	
Displacement	u_i	Spatial velocity	v_i
Displacement gradient	$u_{i,j} = \beta_{ij}$	Spatial velocity gradient	$l_{ij} = v_{i,j}$
Strain	$\epsilon_{ij} = \frac{1}{2}(\beta_{i,j} + \beta_{j,i})$	Rate of deformation	$d_{ij} = \frac{1}{2}(l_{ij} + l_{ji})$
Rotation	$\omega_{ij} = \frac{1}{2}(\beta_{ij} - \beta_{ji})$	Spin	$w_{ij} = \frac{1}{2}(l_{ij} - l_{ji})$

Table A.1.: Deformation measures in linearized kinematics and corresponding deformation rates.

$\frac{1}{2}(u_{i,j} + u_{j,i})$. The infinitesimal rotation tensor ω is introduced as

$$\omega_{ij} = \frac{1}{2}(u_{i,j} - u_{j,i}) \tag{A.61}$$

so that

$$\text{grad}\mathbf{u} = \boldsymbol{\omega} + \boldsymbol{\varepsilon}. \tag{A.62}$$

From the Schwarz integrability condition [Ortiz, 2012], small-strain compatibility follows as

$$\text{curl}\,(\text{curl}\,\boldsymbol{\epsilon}) = \mathbf{0}. \tag{A.63}$$

A.2.3. Rates of deformation

For any deformation measure $G(\boldsymbol{\varphi})$ moving with velocity v, the associated deformation rates are given by

$$\dot{G}(\boldsymbol{\varphi}_t) = \frac{d}{dt}G(\boldsymbol{\varphi}_t) = DG(\boldsymbol{\varphi}_t)\dot{\boldsymbol{\varphi}}_t = DG(\boldsymbol{\varphi}_t)\mathbf{v}_t. \tag{A.64}$$

Deformation measures previously derived in the linearized kinematics framework can thus be used to find their corresponding rates as shown in Table A.2.3.

A.2.4. Conservation laws

In the preceding sections, motions of solids and fluids were described in purely kinematical terms and without taking into account that these motions must obey the fundamental laws of thermodynamics. The following sections are therefore dedicated to establishing conservation laws, which will for the purpose of generality be formulated in both Eulerian as well as Lagrangian frameworks.

Let the Lagrangian and Eulerian mass densities per unit undeformed and deformed volume, respectively, be denoted as $R : B \to \mathbb{R}$ and $\rho : \varphi(B) \to \mathbb{R}$, respectively. Enforcing that the mass of a body B remains constant throughout the deformation gives the condition

$$m(B,t) = \int_B R\, dV = \int_{\varphi(B,t)} \rho\, dv = \int_B \rho J\, dV \qquad \Rightarrow \qquad R = \rho J. \tag{A.65}$$

Furthermore, conservation of mass in Lagrangian form requires that

$$\frac{dm}{dt}(B,t) = \frac{d}{dt}\int_B R\, dV = \int_B \dot{R}\, dV = 0 \qquad \Rightarrow \qquad \dot{R} = 0, \tag{A.66}$$

whereas the local statement of mass conservation in spatial form evaluates to

$$\dot{\rho} + \rho \operatorname{div} \mathbf{v} = 0. \tag{A.67}$$

With linear momentum of a simple body defined by

$$\mathbf{L}(\mathbf{V}) = \int_V R\mathbf{V}\, dV = \int_{\varphi(V)} \rho\mathbf{v}\, dv, \tag{A.68}$$

its change with time must equal the resultant force $\mathbf{F}(\mathbf{V})$ of all forces acting on V, such that linear momentum balance requires

$$\frac{d\mathbf{L}}{dt}(V) = \mathbf{F}(V). \tag{A.69}$$

Here, the resultant force $\mathbf{F}(V)$ includes body forces as well as surface tractions according to

$$\mathbf{F}(V) = \int_V R\mathbf{B}\, dV + \int_{\partial V} \mathbf{T}(\mathbf{N})\, dS = \int_{\boldsymbol{\varphi}(V)} \rho\mathbf{b}\, dv + \int_{\partial\boldsymbol{\varphi}(V)} \mathbf{t}(\mathbf{n})\, ds, \tag{A.70}$$

whereby $R\mathbf{B}$ and $\rho\mathbf{b}$ denote body forces per unit mass in the material and spatial configurations, respectively, and similarly $\mathbf{T}(\mathbf{N})$ and $\mathbf{t}(\mathbf{n})$ denote tractions in the material and spatial configurations. In Lagrangian form, the local statement of conservation of linear momentum therefore follows as

$$R\mathbf{A} = R\mathbf{B} + \operatorname{Div}\mathbf{P}, \tag{A.71}$$

with acceleration $\mathbf{A}$, traction components $T_i(\mathbf{N}) = P_{iI}N_I$, and P_{iI} denoting the components of the first Piola-Kirchhoff stress tensor $\mathbf{P}$ representing forces in the deformed configuration normalized by the undeformed area on which they are acting. In Eulerian form, in contrast, the local statement of conservation of linear momentum reads

$$\rho\mathbf{a} = \rho\mathbf{b} + \operatorname{div}\boldsymbol{\sigma}, \tag{A.72}$$

where $\boldsymbol{\sigma}$ is the Cauchy-stress tensor, which comprises tractions in the deformed configuration ($t_i = \sigma_{ij}n_j$) acting on areas in the deformed configuration. The first Piola-Kirchhoff and the Cauchy stress tensor are related via

$$\boldsymbol{\sigma} = J^{-1}\mathbf{P}\mathbf{F}^T. \tag{A.73}$$

Analogously, the angular momentum $\mathbf{G}$ and the resultant moment $\mathbf{M}$ of all forces can be defined (in the deformed configuration) as

$$\mathbf{G}(v) = \int_{\boldsymbol{\varphi}(v)} \mathbf{x} \times \rho\mathbf{v}\, dv, \tag{A.74}$$

and

$$\mathbf{M}(v) = \int_{\varphi(v)} \mathbf{x} \times \rho \mathbf{b}\, dv + \int_{\partial\varphi(v)} \mathbf{x} \times \mathbf{t}(\mathbf{n})\, ds \tag{A.75}$$

respectively. The change in angular momentum over time must satisfy

$$\frac{d}{dt}\mathbf{G}(v) = \mathbf{M}(v), \tag{A.76}$$

which after some algebraic manipulations leads to the requirement that the Cauchy stress tensor for simple bodies must be symmetric (this excludes special continua such as e.g. Cosserat materials whose microrotations are taken into account):

$$\sigma = \sigma^T. \tag{A.77}$$

In general, one distinguishes extensive variables, whose values are added when two identical systems are combined (e.g. mass m), and intensive variables, whose values remain constant when two identical systems are combined (e.g. temperature T). Important extensive variables in the derivation of conservation laws are the kinetic energy K of a simple continuum V (without any rotational inertia)

$$K(V) = \int_V \frac{1}{2} R |\mathbf{V}|^2 \, dV = \int_{\varphi(V)} \frac{1}{2} \rho |\mathbf{v}|^2 \, dv, \tag{A.78}$$

where $\mathbf{V}$ and $\mathbf{v}$ denote mean material and spatial velocity fields, as well as heat Q, whose change over time results from heat flux $H(\mathbf{N})$ (or equivalently $h(\mathbf{n})$ in the Eulerian framework) and heat sources, i. e.

$$\dot{Q}(V) = \int_V R S_h \, dV - \int_{\partial V} H(\mathbf{N}) dS = \int_{\varphi(V)} \rho s_h \, dv - \int_{\varphi(\partial V)} h(\mathbf{n})\, ds \tag{A.79}$$

with heat source density S_h in material form, and s_h being its spatial counterpart. Fur-

thermore, the external power as the sum of body forces and tractions is

$$P^E(V) = \int_V R\mathbf{B} \cdot \mathbf{V}\, dV + \int_{\partial V} \mathbf{T}(\mathbf{N}) \cdot \mathbf{V}\, dS = \int_{\varphi(V)} \rho \mathbf{b} \cdot \mathbf{v}\, dv + \int_{\partial\varphi(V)} \mathbf{t}(\mathbf{n}) \cdot \mathbf{v}\, ds. \tag{A.80}$$

The deformation power is defined by

$$P^D(V) = P^E(V) - \dot{K}(V) \tag{A.81}$$

and denotes the amount of externally applied power that does not lead to a change in kinetic energy. The integral form of $P^D(V)$ in a Lagrangian framework gives

$$P^D(V) = \int_V \mathbf{P} \cdot \dot{\mathbf{F}}\, dV, \tag{A.82}$$

which implies that $\mathbf{P}$ and $\dot{\mathbf{F}}$ form a work-conjugate pair. Similarly, the spatial form

$$P^D(v) = \int_{\varphi(V)} \boldsymbol{\sigma} \cdot \mathbf{d}\, dv \tag{A.83}$$

shows that the Cauchy stress tensor $\boldsymbol{\sigma}$ and the rate-of-deformation tensor $\mathbf{d}$ are work-conjugate. An overview of work-conjugate pairs can be found in Table A.2.4, and a summary of stress measures is given in Table A.2.4.

Stress	$\mathbf{P}$	$\mathbf{S}$	$\boldsymbol{\sigma}$
Rate of deformation	$\dot{\mathbf{F}}$	$\dot{\mathbf{E}}$	$\mathbf{d}$

Table A.2.: Overview of work-conjugate pairs.

Stress	**Name**	**Configurational space**	**Symmetry**
σ_{ij}	Cauchy	$\frac{\text{force}}{\text{deformed area}}$	symmetric
P_{iJ}	First Piola-Kirchhoff	$\frac{\text{force}}{\text{undeformed area}}$	not symmetric
S_{IJ}	Second Piola-Kirchhoff	$\frac{\text{force (mapped into undeformed configuration)}}{\text{undeformed area}}$	symmetric

Table A.3.: Summary of stress measures.

With the previously-defined deformation power, the first law of thermodynamics can be stated as an exact conversion from external power and heat input into internal or kinetic energy according to

$$\dot{E}(V) + \dot{K}(V) = P^E(V) + \dot{Q}(V). \tag{A.84}$$

From Equation A.84 it follows that the internal energy $E(V)$ is an extensive variable, which leads to defining an internal energy density per unit mass (denoted as U and u in the material and spatial configuration, respectively), viz.

$$E(V) = \int_V RU\, dV = \int_{\boldsymbol{\varphi}(V)} \rho u\, dv. \tag{A.85}$$

Similarly to the cases of conservation of mass and linear momentum, the conservation of energy can also be expressed in local form. To this end, a combination of Equations A.84 and A.85 together with the definitions of external and deformation powers gives

$$\frac{d}{dt}\int_V RU\, dV = \int_V \mathbf{P}\dot{\mathbf{F}}\, dV + \int_V RS_h\, dV - \int_{\partial V} H(\mathbf{N})\, dS. \tag{A.86}$$

In analogy to the previous derivations of local conservation laws, the use of stress/traction relations, Cauchy's tetrahedron law, and the divergence theorem leads to the local statement of energy balance in material and spatial forms as, respectively,

$$R\dot{U} = \mathbf{P}\cdot\dot{\mathbf{F}} + RS_h - \operatorname{Div}\mathbf{H} \tag{A.87}$$

and

$$\rho\dot{u} = \boldsymbol{\sigma}\cdot\mathbf{d} + \rho s_h - \operatorname{div}\mathbf{h}. \tag{A.88}$$

The introduction of the second law of thermodynamics requires a number of additional preliminaries such as a definition of thermodynamic systems and their respective equilibrium states. A *thermodynamic system* denotes a collection of matter characterized by a constant chemical decomposition, and a *closed thermodynamic system* is one that does not exchange matter with its exterior. Such a system is in *uniform thermodynamic equilibrium* if its intensive properties are independent of position and, furthermore, all properties of the system are independent of time. *Internal variables* $\mathbf{Q}$ are required to define the state of a thermo-mechanical system in addition to $\mathbf{F}$ describing kinematics and E describing the energy of a system. Examples include microstructural information or deformation history. A system is in *thermal equilibrium* it two different initially equilibrated systems remain in equilibrium after being placed in contact.

With these definitions at hand, the *zeroth law of thermodynamics* states that if two systems A and B are both in thermodynamic equilibrium with a third system C, then it follows that system A is in thermal equilibrium with system B. Introducing the empirical temperature Θ as a state variable, the zeroth law of thermodynamics may be written as

$$\Theta(A) = \Theta(C) \wedge \Theta(B) = \Theta(C) \quad \Rightarrow \quad \Theta(A) = \Theta(B). \tag{A.89}$$

The state of a system can thus be defined by a collection of state variables $\{\mathbf{F}, \Theta, \mathbf{Q}\}$, whereby their transition over time $\{\mathbf{F}(t), \Theta(t), \mathbf{Q}(t)\}$ for $t_1 < t < t_2$ defines a *thermodynamic process*. A thermodynamic process is *reversible* if its internal variables do not change with time, the process is quasistatic (so that no kinetic energy is turned into heat by dissipation), and each state during the process denotes a uniform thermodynamic equilibrium. It has furthermore been shown via empirical observations that there exists an absolute temperature $T(\Theta)$ that can be uniquely defined up to a constant, so that

$$S_2 = S_1 + \int_1^2 \frac{dQ}{T} \tag{A.90}$$

along arbitrary reversible paths $1 \rightarrow 2$, and $dS = \frac{dQ}{T}$ denotes a total differential. As a result, S must be a state variable that is known as the *entropy* of a thermodynamic system. The foregoing can also be generalized to irreversible processes according to

$$\dot{S}^{int} = \dot{S} - \frac{\dot{Q}}{T}, \tag{A.91}$$

where $\dot{S}^{int}$, $\dot{S}$ and $\frac{\dot{Q}}{T}$ are the internal entropy production rate, the rate of entropy increase in the system, and the external entropy supply, respectively. It follows that for reversible processes, $\dot{S}^{int} = 0$. For irreversible processes (including e.g. heat conduction and viscous flows), empirical observations have shown that $\dot{S}^{int} \geq 0$, based upon which the *second law of thermodynamics* for irreversible processes can be expressed as

$$\dot{S}^{int} = \dot{S} - \dot{S}^{ext} \geq 0. \tag{A.92}$$

Viscosity is an important example that must be taken into account when modeling materials whose state of stress does not only depend on $\{\mathbf{F}, \Theta, \mathbf{Q}\}$, but also on $\dot{\mathbf{F}}$; polymers are prime examples for materials that display pronounced viscous effects. Equilibrium stress $\mathbf{P}^e$ and viscous stress $\mathbf{P}^v$ are defined by, respectively,

$$\mathbf{P}^e(\mathbf{F}, \Theta, \mathbf{Q}) = \mathbf{P}(\dot{\mathbf{F}} = 0, \mathbf{F}, \Theta, \mathbf{Q}) \tag{A.93}$$

and

$$\mathbf{P}^v(\dot{\mathbf{F}}, \mathbf{F}, \Theta, \mathbf{Q}) = \mathbf{P} - \mathbf{P}^e. \tag{A.94}$$

The second law of thermodynamics (in local form) applied to viscous materials implies that

$$\mathbf{P}^v \cdot \dot{\mathbf{F}} \geq 0. \tag{A.95}$$

In order to derive a continuum description of entropy, temperature and the second law of thermodynamics, each material point may be defined as a thermodynamical system. The absolute temperature in Lagrangian and Eulerian form is thus given by $T(\mathbf{X},t)$ and $\Theta = T(\boldsymbol{\varphi}(\mathbf{X},t),t)$, and entropy densities are described as $N(\mathbf{X},t)$ and $\eta = N(\boldsymbol{\varphi}(\mathbf{X},t),t)$ in material and spatial configurations, respectively. Following the definition of the external entropy input by Truesell and Noll, we define

$$\dot{S}^{ext}(V) = \int_V \frac{RS_h}{T}\,dV - \int_{\partial V} \frac{\mathbf{H}\cdot\mathbf{N}}{T}\,dS = \int_{\boldsymbol{\varphi}V} \frac{\rho s_h}{\Theta}\,dv - \int_{\partial\boldsymbol{\varphi}V} \frac{\mathbf{h}\cdot\mathbf{n}}{\Theta}\,ds, \tag{A.96}$$

which yields the Clausius-Duhem inequality in Lagrangian form,

$$\frac{d}{dt}\int_V RN\,dV - \int_V \frac{RS_h}{T}\,dV + \int_{\partial V} \frac{\mathbf{H}\cdot\mathbf{N}}{T}\,dS \geq 0 \tag{A.97}$$

and in Eulerian form,

$$\frac{d}{dt}\int_{\boldsymbol{\varphi}(V)} \rho n\,dv - \int_{\boldsymbol{\varphi}(V)} \frac{\rho s_h}{\theta}\,dv + \int_{\partial\boldsymbol{\varphi}(V)} \frac{\mathbf{h}\cdot\mathbf{n}}{\theta}\,ds \geq 0. \tag{A.98}$$

Bibliography

Robert A. Adams. *Sobolev Spaces*. Academic Press, New York-London, 1975. Pure and Applied Mathematics, Vol. 65.

A. W. Agar, F. C. Frank, and A. Keller. Crystallinity effects in the electron microscopy of polyethylene. *Philosophical Magazine*, 4(37):32–55, 1959.

A. B. Albrecht, K. M. Liechti, and K. Ravi-Chandar. Characterization of the transient response of polyurea. *Experimental Mechanics*, 53:113–122, 2012.

D. Alcazar, J. R. Ruan, A. Thierry, A. Kawaguchi, and B. Lotz. Polysynthetic twinning in poly (vinylcyclohexane) single crystals and "fractional" secondary nucleation in polymer crystal growth. *Macromolecules*, 39(3):1008–1019, 2006.

M. S. M. Alger. *Polymer Science Dictionary*. Springer, 1997.

A. V. Amirkhizi, J. Isaacs, J. McGee, and S. Nemat-Nasser. An experimentally-based viscoelastic constitutive model for polyurea, including pressure and temperature effects. *Philosophical Magazine*, 86(36):5847–5866, 2006.

E. H. Andrews. *Fracture in Polymers*. American Elsevier, New York, 1968.

A. S. Argon. *The Physics of Deformation and Fracture of Polymers*. Cambridge University Press, Cambridge, 2013.

M. Arroyo and M. Ortiz. Local maximum-entropy approximation schemes: a seamless bridge between finite elements and meshfree methods. *International Journal for Numerical Methods in Engineering*, 65(13):2167–2202, 2006.

E. M. Arruda and M. C. Boyce. A three-dimensional constitutive model for the large stretch behavior of rubber elastic materials. *Journal of the Mechanics and Physics of Solids*, 41:389–412, 1993.

A. R. C. Baljon and M. O. Robbins. Simulations of crazing in polymer glasses: Effect of chain length and surface tension. *Macromolecules*, 34(12):4200–4209, 2001.

J. M. Ball. Discontinuous equilibrium solutions and cavitation in nonlinear elasticity. *Philos. Trans. Roy. Soc. London Ser. A*, 306(1496):557–611, 1982.

S. Basu, D. K. Mahajan, and E. Van der Giessen. Micromechanics of the growth of a craze fibril in glassy polymers. *Polymer*, 46(18):7504–7518, 2005.

Z. Bažant and M. Jirásek. Nonlocal integral formulations of plasticity and damage: Survey of progress. *Journal of Engineering Mechanics*, 128:1119–1149, 2002.

Z. P. Bažant. Instability, ductility and size effect in strain-softening concrete. *J. Eng. Mech. Dev.*, 102(2):331–344, 1976.

Z. P. Bažant. Imbricate continuum and its variational derivation. *J. Eng. Mech.*, 110(12):1693–1712, 1984.

Z. P. Bažant and T. B. Belytschko. Wave propagation in a strain-softening bar: Exact solution. *J. Eng. Mech.*, 111(3):381–389, 1985.

Z. P. Bažant and L. Cedolin. Blunt crack band propagation in finite element analysis. *J. Eng. Mech.*, 105(2):297–315, 1979.

Z. P. Bažant and B.-H. Oh. Crack band theory for fracture of concrete. *Mater. Struct.*, 16:155–177, 1983.

Z. P. Bažant, T. B. Belytschko, and T.-P. Chang. Continuum model for strain softening. *J. Eng. Mech.*, 110(12):1666–1692, 1984.

N. M. Bikales. *Mechanical Properties of Polymers*. Encyclopedia reprints. Wiley-Interscience, New York, 1971.

M. Böl and S. Reese. Finite element modelling of rubber-like materials - a comparison between simulation and experiment. *Journal of Materials Science*, 4:5933–5939, 2005.

L. Cedolin and Z. P. Bažant. Effect of finite-element choice in blunt crack band analysis. *Comput. Methods Appl. Mech. Eng.*, 24:305–316, 1980.

V. Chakkarapani, K. Ravi-Chandar, and K. M. Liechti. Characterization of multiaxial constitutive properties of rubbery polymers. *Journal of Engineering Materials and Technoloy*, 128:489–494, 2006.

K. Cho and A. N. Gent. Cavitation in model elastomeric composites. *Journal of Materials Science*, 23(1):141–144, 1988.

R. Choksi, R. V. Kohn, and F. Otto. Domain branching in uniaxial ferromagnets: a scaling law for the minimum energy. *Comm. Math. Phys.*, 201:61–79, 1999.

M. Colakoglu, O. Soykasap, and T. Özek. Experimental and numerical investigations on the ballistic performance of polymer matrix composites used in armor design. *Applied Composite Materials*, 14:47–58, 2007.

S. Conti. Branched microstructures: scaling and asymptotic self-similarity. *Comm. Pure Appl. Math.*, 53:1448–1474, 2000.

S. Conti and C. DeLellis. Some remarks on the theory of elasticity for compressible neohookean materials. *Ann. Scuola Norm. Sup. Pisa Cl. Sci. (5)*, pages 521–549, 2003.

S. Conti and M. Ortiz. Dislocation microstructures and the effective behavior of single crystals. *Arch. Rat. Mech. Anal.*, 176:103–147, 2005.

S. Conti et al. On a model for failure in polymers with fractional strain-gradient regularization. (in preparation), 2014.

R. Cools. An encyclopaedia of cubature formulas. *J. Complexity*, 19:445–453, 2003.

E. Cosserat and F. Cosserat. *Théorie des corps déformables*. Herrmans, Paris, 1909.

Michael Cross. *Statistical Physics Course Notes*. California Institute of Technology, 2006.

B. J. Dimitrijevic and K. Hackl. A method for gradient enhancement of continuum damage models. *Technische Mechanik*, 28:43–52, 2007.

A. M. Donald and E. J. Kramer. The competition between shear deformation and crazing in glassy-polymers. *Journal of Materials Science*, 17(7):1871–1879, 1982.

A. D. Drozdov. Modelling nonlinear viscoelasticity and damage in amorphous glassy polymers. *Mathematical and Computer Modelling*, 33(8-9):883–893, 2001.

D. G. B. Edelen and N. Laws. On the thermodynamics of systems with nonlocality. *Arch. Ration. Mech. Anal.*, 43:24–35, 1971.

T. El Sayed, W. Mock, A. Mota, F. Fraternali, and M. Ortiz. Computational assessment of ballistic impact on a high strength structural steel/polyurea composite plate. *Computational Mechanics*, 43(4):525–534, 2009.

A. C. Eringen. Linear theory of nonlocal elasticity and dispersion of plane waves. *Int. J. Eng. Sci.*, 10:425–435, 1972.

A. C. Eringen and B. S. Kim. Stress concentration at the tip of a crack. *Mech. Res. Commun.*, 1: 233–237, 1974.

R. Estevez, S. Basu, and E. Van Der Giessen. A thermo-mechanical investigation of the influence of shear yielding and crazing on fracture characteristics of glassy polymers. *Advances in Mechanical Behaviour, Plasticity and Damage, Vols 1 and 2, Proceedings*, pages 225–230, 2000a.

R. Estevez, M. G. A. Tijssens, and E. Van der Giessen. Modeling of the competition between shear yielding and crazing in glassy polymers. *Journal of the Mechanics and Physics of Solids*, 48(12): 2585–2617, 2000b.

N. A. Fleck and J. W. Hutchinson. A phenomenological theory for strain gradient effects in plasticity. *Journal of the Mechanics and Physics of Solids*, 41(12):1825–1857, 1993.

N. A. Fleck and J. W. Hutchinson. Strain gradient plasticity. *Advances in Applied Mechanics*, 33: 295–361, 1997.

N. A. Fleck and J. W. Hutchinson. A reformulation of strain gradient plasticity. *Journal of the Mechanics and Physics of Solids*, 49(10):2245–2271, 2001.

N. A. Fleck, G. M. Muller, M. F. Ashby, and J. W. Hutchinson. Strain gradient plasticity - theory and experiment. *Acta Metallurgica Et Materialia*, 42(2):475–487, 1994.

P. J. Flory. *Statistical Mechanics of Chain Molecules*. Interscience Publishers, New York, 1969.

P. J. Flory. *Statistical Mechanics of Chain Molecules*. Hanser Publishers, Munich, 1989.

W. Flügge. *Tensor Analysis*. Springer, New York, 1972.

L. Fokoua, S. Conti, and M. Ortiz. Optimal scaling in solids undergoing ductile fracture by void sheet formation. *Archive for Rational Mechanics and Analysis*, 212:331–357, 2014a.

L. Fokoua, S. Conti, and M. Ortiz. Optimal scaling laws for ductile fracture derived from strain-gradient microplasticity. *J. Mech. Phys. Solids*, 62:295–311, 2014b. doi: 10.1016/j.jmps.2013.11.002.

A. Fortunelli and M. Ortiz. Constitutive model for plasticity in an amorphous polycarbonate. *Physical Review E*, 76(4), 2007.

A. Fortunelli, C. Geloni, and A. Lazzeri. Simulation of the plastic behavior of amorphous glassy bis-phenol-a-polycarbonate. *Journal of Chemical Physics*, 121(10):4941–4950, 2004.

P. H. Geil. *Polymer Single Crystals*. Polymer reviews,. Interscience Publishers, New York,, 1963.

A. N. Gent. Cavitation, crazing and fracture in glassy polymers. *Bulletin of the American Physical Society*, 18(3):400–400, 1973.

A. N. Gent and C. Wang. Fracture-mechanics and cavitation in rubber-like solids. *Journal of Materials Science*, 26(12):3392–3395, 1991.

A. Gloria, P. Le Tallec, and M. Vidrascu. Foundation, analysis, and numerical investigation of a variational network-based model for rubber. *Continuum Mechanics and Thermodynamics*, 26: 1–31, 2013. doi: 10.1007/s00161-012-0281-6.

Granta Design. Young's modulus versus density plot. `http://www.grantadesign.com/images/ces/Youngs-Density-2012-large.jpg`, 2014. Accessed: 2014-08-10.

A. E. Green and R. S. Rivlin. Simple force and stress multi-poles. *Arch. Ration. Mech. Anal.*, 16: 325–353, 1964.

W. Grellmann and S. Seidler. *Deformation and Fracture Behavior of Polymers*. Engineering materials. Springer, Berlin, 2001.

G. Grioli. Elasticità asimmetrica. *Annali di matematica pura ed applicata*, IV:389–417, 1960.

M. Grujicic, B. Pandurangan, K. L. Koudela, and B. A. Cheeseman. A computational analysis of the ballistic performance of light-weight hybrid composite armors. *Applied Surface Science*, 253: 730–745, 2006.

D. Henao and C. Mora-Corral. Invertibility and weak continuity of the determinant for the modelling of cavitation and fracture in nonlinear elasticity. *Archive for Rational Mechanics and Analysis*, 197:619–655, 2010.

C. S. Henkee and E. J. Kramer. Loss of entanglement density during crazing. *Journal of Materials Science*, 21(4):1398–1404, 1986.

G. Hermann. *R. D. Mindlin and Applied Mechanics; a collection of studies in the development of applied mechanics, dedicated to Professor Raymond D. Mindlin by his former students*. Pergamon Press, New York,, 1974.

S. Heyden, B. Li, K. Weinberg, S. Conti, and M. Ortiz. A micromechanical damage and fracture model for polymers based on fractional strain-gradient elasticity. *Journal of the Mechanics and Physics of Solids*, 74:175–195, 2014.

S. Heyden, S. Conti, and M. Ortiz. A nonlocal model of fracture by crazing in polymers. *Mechanics of Materials*, 2015. Paper under review.

G. A. Holzapfel. *Nonlinear Solid Mechanics: A Continuum Approach for Engineering*. John Wiley & Sons Ltd, Chichester, England, 1st edition, 2000.

Y. Huang, Z. Xue, H. Gao, W. D. Nix, and Z. C. Xia. A study of microindentation hardness tests by mechanism-based strain gradient plasticity. *Journal of Materials Research*, 15(8):1786–1796, 2000.

J. W. Hutchinson. Singular behaviour at end of a tensile crack in a hardening material. *Journal of the Mechanics and Physics of Solids*, 16(1):13–31, 1968.

J. W. Hutchison. A course on nonlinear fracture mechanics. Dept. Solid Mechanics, TU Denmark, 1979.

Richard D. James and Scott J. Spector. The formation of filamentary voids in solids. *J. Mech. Phys. Solids*, 39(6):783–813, 1991. ISSN 0022-5096.

T. Jiao, R. J. Clifton, and S. E. Grunschel. High strain rate response of an elastomer. *Shock Compression of Condensed Matter - 2005, Pts 1 and 2*, 845:809–812, 2006.

T. Jiao, R. J. Clifton, and S. E. Grunschel. Pressure-sensitivity and tensile strength of an elastomer at high strain rates. *Shock Compression of Condensed Matter - 2007, Pts 1 and 2*, 955:707–710, 2007.

T. Jiao, R. J. Clifton, and S. E. Grunschel. Pressure-sensitivity and consititutive modeling of an elastomer at high strain rates. *Shock Compression of Condensed Matter - 2009, Pts 1 and 2*, 1195: 1229–1232, 2009.

M. F. Kanninen and C. H. Popelar. *Advanced Fracture Mechanics*. Oxford engineering science series. Oxford University Press, New York, 1985.

H. H. Kausch, editor. *Crazing in Polymers*. Springer-Verlag, Berlin, 1983.

H. H. Kausch. *Polymer Fracture*. Polymers, Properties and Applications. Springer-Verlag, Berlin, 2nd edition, 1985.

A. Keller. Polymer crystals. *Reports on Progress in Physics*, 31:623, 1968.

H. Kiho, P. H. Geil, and A. Peterlin. Polymer deformation (6) - twinning and phase transformation of polyethylene single crystals as function of stretching direction. *Journal of Applied Physics*, 35 (5), 1964.

A. J. Kinloch and Robert J. Young. *Fracture Behaviour of Polymers*. Applied Science Publishers, London, 1983.

W. G. Knauss and J. Zhao. Improved relaxation time coverage in ramp-strain histories. *Mechanics of Time-Dependent Materials*, 11:199–216, 2007.

R. V. Kohn and S. Müller. Branching of twins near an austenite-twinned-martensite interface. *Phil. Mag. A*, 66:697–715, 1992.

R. V. Kohn and S. Müller. Surface energy and microstructure in coherent phase transitions. *Comm. Pure Appl. Math.*, 47:405–435, 1994.

A. J. Kovacs, B. Lotz, and A. Keller. Multiple twinning in polyethylene oxide singlecrystals - a scheme for formation of growth twins from self-seeding nuclei. *Journal of Macromolecular Science-Physics*, B3(3):385, 1969.

E. J. Kramer and L. L. Berger. Fundamental processes of craze growth and fracture. *Advances in Polymer Science*, 91/92:1–68, 1990.

E. Kröner, editor. *Mechanics of Generalized Continua; proceedings of the IUTAM-symposium on the Generalized Cosserat Continuum and the Continuum Theory of Dislocations with Applications*. Springer-Verlag, Berlin, 1968.

T. N. Krupenkin and G. H. Fredrickson. Crazing in two and three dimensions. 1. two-dimensional crazing. *Macromolecules*, 32(15):5029–5035, 1999a.

T. N. Krupenkin and G. H. Fredrickson. Crazing in two and three dimensions. 2. three-dimensional crazing. *Macromolecules*, 32(15):5036–5045, 1999b.

W. Kuhn and F. Grün. Beziehungen zwischen elastischen konstanten und dehnungsdoppelbrechung hochelastischer stoffe. *Kolloid-Zeitschrift*, 101:248–271, 1942.

A. I. Leonov and H. R. Brown. A model of fibril deformation in crazes. *Journal of Polymer Science. Part B - Polymer Physics*, 29(2):197–209, 1991.

B. Li. *The Optimal Transportation Method in Solid Mechanics*. PhD thesis, California Institute of Technology, 2009.

B. Li, F. Habbal, and M. Ortiz. Optimal transportation meshfree approximation schemes for fluid and plastic flows. *International Journal for Numerical Methods in Engineering*, 83(12):1541–1579, 2010.

B. Li, A. Kidane, G. Ravichandran, and M. Ortiz. Verification and validation of the Optimal Transportation Meshfree (OTM) simulation of terminal ballistics. *International Journal of Impact Engineering*, 42:25–36, 2012.

C. Lin and M. Fatt. Perforation of composite plates and sandwich panels under quasi-static and projectile loading. *Composite Materials*, 40:1801–1840, 2006.

Alessandra Lunardi. *Interpolation theory*. Appunti. Scuola Normale Superiore di Pisa (Nuova Serie). Edizioni della Normale, Pisa, second edition, 2009.

J. Makowski, K. Hackl, and H. Stumpf. The fundamental role of nonlocal and local balance laws of material forces in finite elastoplasticity and damage mechanics. *International Journal of Solids and Structures*, 43:3940–3959, 2006.

J. B. Martin. *Plasticity : fundamentals and general results*. MIT Press, Cambridge, Mass., 1975.

G. A. Maugin and Andrei V. Metrikine. *Mechanics of Generalized Continua: One Hundred Years after the Cosserats*. Advances in mechanics and mathematics,. Springer, New York, 2010.

F. A. McClintock and Ali S. Argon. *Mechanical Behavior of Materials*. Addison-Wesley series in metallurgy and materials,. Addison-Wesley Pub. Co., Reading, Mass., 1966.

C. Miehe, S. Göktepe, and F. Lulci. A micro-macro approach to rubber-like materials - Part I: the non-affine micro-sphere model of rubber elasticity. *Journal of the Mechanics and Physics of solids*, 52:2617–2660, 2004.

R. D. Mindlin. Microstructure in linear elasticity. *Arch. Ration. Mech. Anal.*, 16:51–78, 1974.

W. Mock, Jr. (presenter) and J. Drotar. Penetration protection experiments using polymer materials. *ONR Workshop, St. Michael's, Maryland*, 2006.

S. Müller and S. J. Spector. An existence theory for nonlinear elasticity that allows for cavitation. *Arch. Rat. Mech. Anal.*, 131:1–66, 1995.

B. Nedjar. Elastoplastic-damage modelling including the gradient of damage: formulation and computational aspects. *International Journal of Solids and Structures*, 38:5421–5451, 2001.

W. D. Nix and H. J. Gao. Indentation size effects in crystalline materials: A law for strain gradient plasticity. *Journal of the Mechanics and Physics of Solids*, 46(3):411–425, 1998.

W. Noll. A new mathematical theory of simple materials. *Arch. Ration. Mech. Anal.*, 48:1–50, 1972.

M. Ortiz. *Continuum Mechanics Course Notes*. California Institute of Technology, 2012.

M. Ortiz and L. Stainier. The variational formulation of viscoplastic constitutive updates. *Computer Methods in Applied Mechanics and Engineering*, 171(3-4):419–444, 1999.

A. Pandolfi and M. Ortiz. An eigenerosion approach to brittle fracture. *International Journal for Numerical Methods in Engineering*, 92(8):694–714, 2012.

A. Pandolfi, B. Li, and M. Ortiz. *Computational Modelling of Concrete Structures*. Taylor & Francis Group, London, 2014.

S. Pietruszczak and Z. Mròz. Finite-element analysis of deformation of strain-softening materials. *Int. J. Numer. Methods Eng.*, 17:327–334, 1981.

C. Polizzotto. Nonlocal elasticity and related variational principles. *Int. J. Solids Struct.*, 38:7359–7380, 2001.

P. Pradère, J. F. Revol, and R. S. Manley. Microdomains in poly(4-methylpentene-1) single-crystals. *Macromolecules*, 21(9):2747–2751, 1988.

C. Reina, B. Li, K. Weinberg, and M. Ortiz. A micromechanical model of distributed damage due to void growth in general materials and under general deformation histories. *International Journal for Numerical Methods in Engineering*, 93(6):575–611, 2013.

D. H. Reneker and P. H. Geil. Morphology of polymer single crystals. *Journal of Applied Physics*, 31(11):1916–1925, 1960.

T. Reppel, T. Dally, and K. Weinberg. On the elastic modeling of highly extensible polyurea. *Technische Mechanik*, 33(1):19–33, 2012.

J. R. Rice. A path independent integral and approximate analysis of strain concentration by notches and cracks. *Journal of Applied Mechanics*, 35(2):379–386, 1968.

J. R. Rice and G. F. Rosengren. Plane strain deformation near a crack tip in a power-law hardening material. *Journal of the Mechanics and Physics of Solids*, 16(1):1–12, 1968.

R. S. Rivlin and A. G. Thomas. Rupture of rubber. i. characteristic energy for tearing. *Journal of Polymer Science*, 10:291–318, 1953.

D. Rogula. *Introduction to nonlocal theory of material media*. Nonlocal theory of material media, CISM courses and lectures. Springer, Wien, 1982.

C. M. Roland and R. Casalini. Effect of hydrostatic pressure on the viscoelastic response of polyurea. *Polymer*, 48:5747–5752, 2007.

C. M. Roland, J. N. Twigg, Y. Vu, and Mott P. H. High strain rate mechanical behavior of polyurea. *Polymer*, 48(2):574–578, 2007.

J. Rottler and M. O. Robbins. Growth, microstructure, and failure of crazes in glassy polymers. *Physical Review E*, 68(1), 2003.

J. Rottler and M. O. Robbins. Craze formation and the fracture energy of glassy polymers. *Chaos*, 14(4):5–5, 2004.

N. Saad-Gouider, R. Estevez, C. Agnon, and R. Seguela. Calibration of a viscoplastic cohesive zone for crazing in PMMA. *Engineering Fracture Mechanics*, 73(16):2503–2522, 2006.

R. D. Sanderson and H. Pasch, editors. *Crazing and Fracture in Polymers: Micro-mechanisms and effect of molecular variables*, volume 214. 2004.

S. S. Sarva, S. Deschanel, M. C. Boyce, and W. Chen. Stress-strain behavior of a polyurea and a polyrethane from low to high strain rates. *Polymer*, 48:2208–2213, 2007.

B. Schmidt, F. Fraternali, and M. Ortiz. Eigenfracture: An eigendeformation approach to variational fracture. *Multiscale Modeling & Simulation*, 7(3):1237–1266, 2009.

T. Seelig and E. Van der Giessen. A cell model study of crazing and matrix plasticity in rubber-toughened glassy polymers. *Computational Materials Science*, 45(3):725–728, 2009.

A. Simone, H. Askes, R. Peerlings, and L. Sluys. Interpolation requirements for implicit gradient-enhanced continuum damage models. *Communications in Numerical Methods in Engineering*, 19: 563–572, 2003.

S. Socrate, M. C. Boyce, and A. Lazzeri. A micromechanical model for multiple crazing in high impact polystyrene. *Mechanics of Materials*, 33(3):155–175, 2001.

Luc Tartar. *An Introduction to Sobolev Spaces and Interpolation Spaces*. Springer, 2007.

M. G. A. Tijssens and E. van der Giessen. A possible mechanism for cross-tie fibril generation in crazing of amorphous polymers. *Polymer*, 43(3):831–838, 2002.

M. G. A. Tijssens, E. van der Giessen, and L. J. Sluys. Modeling of crazing using a cohesive surface methodology. *Mechanics of Materials*, 32(1):19–35, 2000a.

M. G. A. Tijssens, E. van der Giessen, and L. J. Sluys. Simulation of mode i crack growth in polymers by crazing. *International Journal of Solids and Structures*, 37(48-50):7307–7327, 2000b.

R. A. Toupin. Elastic materials with couple stresses. *Arch. Ration. Mech. Anal.*, 11:385–414, 1962.

L.R.G. Treloar. *The Physics of Rubber Elasticity*. Oxford at the Clarendon Press, Oxford, 1949.

J. Červenka, Z. P. Bažant, and M. Wierer. Equivalent localization element for crack band approach to mesh-size sensitivity in microplane model. *Int. J. Numer. Methods Eng.*, 62(5):700–726, 2005.

P. Wambua, B. Vangrimde, S. Lomov, and V. Ignaas. The response of natural fibre composites to ballistic impact by fragment simulating projectiles. *Composite Structures*, 77:232–240, 2007.

K. Weinberg and T. Reppel. Elastic response and damage by cavitation in polyurea. *subm. to Exp. Mechanics*, 2013.

J. H. Weiner. *Statistical Mechanics of Elasticity*. Dover Publications, Mineola, N. Y., 2nd edition, 2002.

J. G. Williams. *Fracture Mechanics of Polymers*. Ellis Horwood series in engineering science. E. Horwood, Halsted Press, Chichester, 1984.

J. C. Wittmann and A. J. Kovacs. Multiple twins in polyethylene monocrystals. *Berichte Der Bunsen-Gesellschaft Für Physikalische Chemie*, 74(8-9):901, 1970.

Z. Xue, Y. Huang, F. Gao, and W. D. Nix. The strain gradient effects in micro-indentation hardness experiments. *Multiscale Phenomena in Materials - Experiments and Modeling*, 578:53–58, 2000.

J. Yi, M. C. Boyce, G. F. Lee, and E. Balizer. Large deformation rate-dependent stress-strain behavior of polyurea and polyurethanes. *Polymer*, 47:319–329, 2006.

Z. Yong, Liechti K. M., and K. Ravi-Chandar. Direct extraction of rate-dependent tractionâ€“separation laws for polyurea/steel interfaces. *International Journal of Solids and Structures*, 46:31–51, 2009. doi: doi:10.1016/j.ijsolstr.2008.08.019.

F. Zairi, M. Nait-Abdelaziz, J. M. Gloaguen, and J. M. Lefebvre. Modelling of the elasto-viscoplastic damage behaviour of glassy polymers. *International Journal of Plasticity*, 24(6):945–965, 2008.

J. Zhao, W. Knauss, and G. Ravichandran. Applicability of the time-temperature superposition principle in modeling dynamic response of a polyurea. *Mechanics of Time-Dependent Materials*, 11:289–308, 2007.